ACTAS DEL I CONGRESO INTERNACIONAL DE INGENIERÍA CIVIL (CIIC 2025)

FONDO EDITORIAL ULIMA

# ADVANCES IN CIVIL ENGINEERING: STRUCTURES, INFRASTRUCTURE, SUSTAINABILITY, AND EMERGING TECHNOLOGIES

Actas del I Congreso Internacional de Ingeniería Civil (CIIC 2025)

Advances in Civil Engineering: Structures, Infrastructure, Sustainability, and Emerging Technologies

ACTAS DEL I CONGRESO INTERNACIONAL DE INGENIERÍA CIVIL (CIIC 2025)

FONDO
EDITORIAL
ULIMA

# ADVANCES IN CIVIL ENGINEERING: STRUCTURES, INFRASTRUCTURE, SUSTAINABILITY, AND EMERGING TECHNOLOGIES

Congreso Internacional de Ingeniería Civil (1.° : 2025 : Lima, Perú)

*Advances in Civil Engineering: Structures, Infrastructure, Sustainability, and Emerging Technologies. Actas del I Congreso Internacional de Ingeniería Civil* / organizado por la Carrera de Ingeniería Civil de la Universidad de Lima. Primera edición digital. Lima: Universidad de Lima, Fondo Editorial, 2026.

105 páginas: ilustraciones, diagramas, gráficos.
Incluye referencias.

Ponencias del I Congreso Internacional de Ingeniería Civil (CIIC), titulado "*Advances in Civil Engineering: Structures, Infrastructure, Sustainability, and Emerging Technologies*", realizado en la Universidad de Lima del 28 al 30 de mayo de 2025.

1. Ingeniería civil – Congresos. 2. Construcción -- Congresos. 3. Estructuras (Construcción) -- Congresos. 4. Ingeniería civil -- Innovación tecnológica -- Congresos. 5. Ingeniería civil – Aspectos ambientales -- Congresos. I. Actas del I Congreso Internacional de Ingeniería Civil (1.° : 2025 : Lima, Perú). II. Universidad de Lima. Fondo Editorial.

624.06
C ISBN 978-9972-45-695-4

*Advances in Civil Engineering: Structures, Infrastructure, Sustainability, and Emerging Technologies*
*Actas del I Congreso Internacional de Ingeniería Civil (CIIC 2025)*
Primera edición digital: abril, 2026


Universidad de Lima
Fondo Editorial
Av. Javier Prado Este 4600,
Urb. Fundo Monterrico Chico, Lima 33
Apartado postal 852, Lima 100, Perú
Teléfono: 437-6767, anexo 30131
fondoeditorial@ulima.edu.pe
www.ulima.edu.pe

Diseño, edición y carátula: Fondo Editorial de la Universidad de Lima



ISBN 978-9972-45-695-4
ISSN (en línea) 3152-9062

Hecho el depósito legal en la Biblioteca Nacional del Perú n.° 2026-04302

## Junta Directiva / Steering Committee

- Edgar Valcárcel Pollard, Director de la Carrera de Ingeniería Civil
- Darwin La Torre Esquivel, Presidente del congreso y coordinador del comité de ponencias
- Flavio Silva, Presidente del congreso
- Carlos Moquillaza Vizarreta, Vicepresidente del congreso

## Comité Organizador / Organizing Committee

- Israel Montoya, coordinador del comité editorial
- Henrry Delgado Ortega, coordinador del comité de gestión de artículos e indexación
- Joao Rengifo Reátegui, coordinador del comité de patrocinadores, auspiciadores y expoferia
- Valeria Micali Morales, coordinadora de los comités de compras y logística, e imagen y estilo
- Juan Pablo Cedrón Marín, coordinador del comité de publicidad, página web y correo

## Comité editorial / Editorial Committee

- Daniel Cardoso, Pontificia Universidad Católica de Río de Janeiro (Brasil)
- Efraín Noa Yarasca, Texas A&M AgriLife (Estados Unidos)
- Matías Hube Ginestar, Pontificia Universidad Católica de Chile (Chile)
- Miguel Dmitrusenko, Universidad Nacional de Ingeniería
- Nabilt Jill Moggiano, Universidad Continental
- Luis Quiroz, Universidad de Lima
- José Luis Wong, Universidad de Lima
- Ricardo Madrid, Universidad de Lima
- Henrry Delgado Ortega, Universidad de Lima
- Israel Montoya, Universidad de Lima
- Joao Rengifo Reátegui, Universidad de Lima

# Table of contents

# Foreword

https://doi.org/10.26439/ciic2025.8663

The Civil Engineering Program at the University of Lima presents the proceedings of the 1st International Congress of Civil Engineering (CIIC 2025), held on May 28-30, 2025. This volume brings together seven peer-reviewed papers selected for publication from the congress. The contributions included here address a range of topics that are central to contemporary civil engineering, including seismic and structural performance, sustainable construction materials, infrastructure monitoring, and the application of digital and data-driven methods to inspection, assessment, and decision-making.

The congress also included keynote lectures by distinguished specialists from Peru and abroad, whose participation contributed to the broader academic exchange fostered by the event. While those lectures were an important part of the congress program, the present volume is devoted exclusively to the scientific papers accepted for publication.

The papers published in these proceedings reflect the thematic breadth of the congress and the diversity of current research interests in the field. They cover seismic and structural engineering, sustainable construction, transportation infrastructure, and emerging technologies applied to civil engineering. Presented in a hybrid format, the congress brought together researchers and professionals from Peru, Chile, and Colombia, creating a space for the discussion of shared challenges and current lines of inquiry across the region.

The Civil Engineering Program gratefully acknowledges the support of its sponsors—Cosapi, Bituper, PSS, PSV, and Unacem—as well as the work of the reviewers, session chairs, and volunteers who contributed to the organization of the event. It also extends its appreciation to all authors and participants whose contributions made CIIC 2025 a valuable forum for academic exchange within the civil engineering community.

# CONFERENCE PAPERS

# Development of a Numerical Model to Estimate the Capacity of Confined Tubular Masonry Walls, Unreinforced and Reinforced with Electrowelded Mesh

Balmes Tucto[1], Luis Quiroz[2]

[1] balmes.tucto@usil.pe, [2] lquiroz@ulima.edu.pe

[1]School of Engineering, San Ignacio de Loyola University, Peru | [2]Facultad de Ingeniería, Universidad de Lima, Perú

Recibido: 8 Mayo 2025 / Publicado: 24 Abril 2026
https://doi.org/10.26439/ciic2025.8664

ABSTRACT. **Brick is the predominant material used in dwelling construction in Peru; however, it is used inadequately, without proper technical supervision, resulting in informal buildings. These informal constructions are highly vulnerable, and when combined with Peru's high seismic hazard, they pose a serious risk of significant human loss during major seismic events. Among these, confined walls made of tubular bricks—also known as confined tubular masonry walls—are the most vulnerable; nevertheless, they are the most common structural walls in informal construction due to their low cost. The vulnerability of confined tubular masonry walls can be reduced through appropriate reinforcement techniques. In this context, a numerical model was calibrated to estimate the capacity of unreinforced and reinforced confined tubular masonry walls with electrowelded wire mesh. The model incorporates the longitudinal and transverse steel of the confining columns, axial load, masonry prism compressive strength, and electrowelded wire mesh. It follows a bilinear behavior and was calibrated using the multiple linear regression method and test results from the National University of Engineering (UNI) and the Pontifical Catholic University of Peru (PUCP). The model achieved a coefficient of multiple determination ($R^2$) of 0.88 for resistance and 0.42 for drift, with corresponding standard errors (SEs) of 0.033 and 0.00073, respectively.**

KEYWORDS: Confined tubular masonry walls, tubular brick, electrowelded wire mesh.THEMATIC AXES: Seismic and structural engineering.

## I. Introduction

In Peru, masonry walls are mainly built using four types of bricks or masonry units: solid industrial bricks, solid handmade bricks, industrial hollow bricks, and tubular bricks. The last three types are subject to restrictions for use as structural walls in highly seismic areas. Specifically, the Peruvian Masonry Standard (NTE-E.070) prohibits the use of industrial hollow bricks and tubular bricks, and in the case of solid handmade bricks, it only allows their use in buildings with a maximum of two stories located in the country's most seismic areas [1]. The regulatory restrictions are frequently disregarded by property owners or builders. As a result, dwellings constructed with these three types of bricks are commonly found along Peru's coast and highlands, leading to informal constructions that are highly vulnerable to both major and moderate seismic events.

According to the National Institute of Statistics and Informatics (INEI), 55.8% of

dwellings in Peru use brick or concrete block as the predominant construction material [2]. Moreover, a study by the Group for the Analysis of Development (GRADE) concluded that seven out of ten dwellings in the country are informal constructions [3]. The president of the Peruvian Chamber of Construction (CAPECO) has likewise indicated that 70% of dwellings in Lima are informal constructions and that an even higher percentage is observed in other regions of the country [4]. In that regard, a study by the Peruvian–Japanese Center for Seismic Research and Disaster Mitigation (CISMID) reported that 83% of dwellings in emerging areas of Lima are informal constructions. These structures fail to comply with the displacement limits established by the Seismic Resistant Design Standard (NTE-E.030) and the resistance requirements of the Masonry Standard (NTE-E.070), as their walls are made with inadequate bricks [5].

Among the different wall types, those build with tubular bricks—referred to as confined tubular masonry walls—exhibit the lowest load-bearing capacity. However, they are the most widely used in informal construction due to their low cost. Several research have therefore been conducted to demonstrate both the poor performance of confined tubular masonry walls under vertical and horizontal loads and the improved behavior achieved when these walls are reinforced with electrowelded wire mesh. The reinforcement technique using electrowelded wire mesh has been studied under different connection configurations between the mesh and the wall, including walls with the mesh connected to the masonry [6], to the masonry and the vertical confinement elements [7], [8], and to the masonry and all the confinement elements [9], [10].

Peru lies within a region where 80% of the world's earthquake occur, making it one of the most seismically active countries on the planet [11]. In addition, the predominant use of masonry units or bricks in dwellings—often the result of informal construction practices—further increases seismic vulnerability, as these structures typically employ deficient construction techniques and poor-quality materials, such as the use of tubular bricks instead of solid industrial ones. Hence, it is essential to develop a model for both unreinforced and reinforced confined tubular masonry walls to assess their seismic performance.

Three specific objectives were considered to meet the general objective of developing a numerical model for confined tubular masonry walls. The first is to collect capacity curves for both unreinforced and reinforced confined tubular masonry walls; the second is to transform these capacity curves into bilinear curves; and the third is to calibrate a numerical model using an appropriate statistical regression method. In this study, the dependent variable is the numerical model and the independent variable is the regression method. Finally, the research hypothesis proposes that the multiple linear regression method is appropriate to determine the capacity of both unreinforced and reinforced confined tubular masonry walls with electrowelded wire mesh.

## II. Background

The background is organized into three sections. The first section presents experimental studies on unreinforced confined tubular masonry walls. The second section discusses experimental studies on reinforced confined tubular masonry walls strengthened with electrowelded wire mesh. This section is further divided into three subsections, which differentiate the types of mesh-to-wall connection and the reinforcement applied on one versus both sides of the wall. The third section reviews three studies that focus on model calibration for confined masonry walls using statistical regression methods and laboratory wall test results.

### *A. Unreinforced Confined Tubular Masonry Walls*

In the design of reinforced concrete structures and metal structures, it is common to adopt foreign design standards. However, this approach is not appropriate for masonry structures, since construction procedures and materials differ markedly from those used in other countries [12]. Accordingly, this section presents national research on unreinforced confined tubular masonry walls. These studies were conducted in the laboratories of the National University of Engineering (UNI) and the Pontifical Catholic University of Peru

TABLE I
UNREINFORCED CONFINED TUBULAR MASONRY WALLS

| Author | Wall | Reinforcement | $t_{max}$ (MPa) | $D_{ult}$ (-) |
|---|---|---|---|---|
| Salinas & Lazares (2008) | 1 | NR | 0.55 | 0.0049 |
| Salinas & Lazares (2008) | 2 | NR | 0.54 | 0.0057 |
| Araoz & Velezmoro (2012) | 3 | NR | 0.53 | 0.0051 |
| Zavala et al. (2014) | 4 | NR | 0.44 | 0.0025 |
| Diaz et al. (2017) | 5 | NR | 0.50 | 0.0050 |
| Diaz et al. (2020) | 6 | NR | 0.46 | 0.0015 |
| Minimum | - | - | 0.44 | 0.0015 |
| Average | - | - | 0.50 | 0.0041 |
| Maximum | - | - | 0.55 | 0.0057 |

(PUCP). Table I shows the maximum capacity achieved by each unreinforced wall (NR) in terms of shear stress and drift. The reported shear stress corresponds to the maximum observed value, and the drift corresponds to the ultimate stress or 80% of the maximum observed stress, since beyond this point the wall becomes unstable [13].

Salinas and Lazares [14] were the first to study confined tubular masonry, motivated by the extensive use of tubular brick in the main walls of dwellings in Lima. Their study aimed to understand the behavior of confined tubular masonry walls. Notably, it is the only work that considered walls constructed with both industrial and handmade tubular bricks. Subsequent studies have focused exclusively on walls made of industrial tubular bricks. The findings indicated that the walls built with industrial tubular bricks were more resistant than those with handmade tubular bricks, but exhibited lower displacement capacity.

Araoz and Velezmoro [6], Zavala et al. [15], Diaz et al. [9], and Diaz et al. [10] also studied confined tubular masonry with the same objective and rationale. They additionally analyzed a series of masonry prisms, which presented a key mechanism between the mortar and the tubular brick that significantly increased the diagonal tensile strength. In this context, it was observed that the capacity of walls made of tubular brick is reduced by vertical loads than by horizontal ones. While key mechanisms provide good resistance to horizontal loads, the horizontal tubules of the brick make the wall fragile under vertical loads. Consequently, walls tested under excessive vertical loads showed reduced resistance and displacement capacities.

In Table I, the minimum and maximum resistance values are close to the average. However, in the case of drifts, the minimum value differs considerably from the average. This difference occurs because the ultimate drift is restricted to the point corresponding to 80% of the maximum resistance; if this restriction were ignored, the result would be closer to the average. In Wall 6 test, the wall reached a drift greater than 0.0040, but this value was not considered because the resistance fell below 80% of the maximum. It is worth mentioning that the minimum and average drift values are close to those recommended by Zavala et al. [5], who proposed using a design drift of 0.0017 and an ultimate drift of 0.0037 for confined tubular masonry walls. Moreover, Fig. 1 shows bilinear models of the capacity curves of unreinforced walls listed in the previous table, based on the American Society of Civil Engineers/ Structural Engineering Institute (ASCE/SEI) 41-13 methodology [13].

*B. Reinforced Confined Tubular Masonry Walls*

Similar to the previous section on unreinforced confined tubular masonry walls, this section presents national research on confined tubular

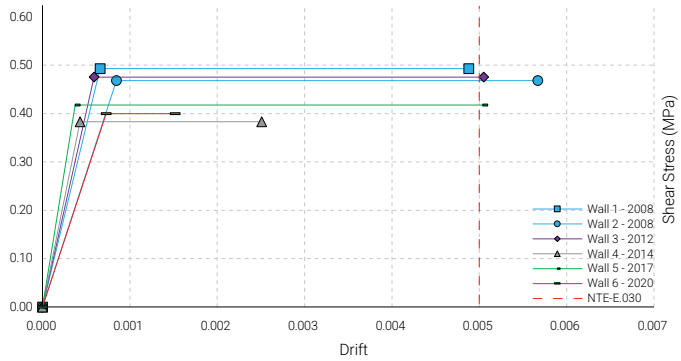


Fig. 1. Bilinear models of capacity curves for unreinforced confined tubular masonry walls.

TABLE II

REINFORCED CONFINED TUBULAR MASONRY WALLS

| Author | Wall | Reinforcement | $t_{max}$ (MPa) | $D_{ult}$ (-) |
|---|---|---|---|---|
| Araoz & Velezmoro (2012) | 7 | R-M-2 | 0.69 | 0.0074 |
| Mamani (2015) | 8 | R-MC-2 | 0.90 | 0.0073 |
| Mamani (2015) | 9 | R-MC-2 | 1.03 | 0.0077 |
| Diaz et al. (2017) | 10 | R-MCB-2 | 0.84 | 0.0053 |
| Diaz et al. (2020) | 11 | R-MCB-1 | 0.70 | 0.0026 |
| Diaz et al. (2020) | 12 | R-MCB-2 | 0.98 | 0.0098 |
| SENCICO (2021) | 13 | R-MC-1 | 0.77 | 0.0032 |
| SENCICO (2021) | 14 | R-MC-1 | 0.69 | 0.0065 |
| Minimum | - | - | 0.69 | 0.0026 |
| Average | - | - | 0.83 | 0.0062 |
| Maximum | - | - | 1.03 | 0.0098 |

masonry walls reinforced with electrowelded wire mesh. These studies were conducted in the laboratories of PUCP and UNI. Table II shows the maximum capacity reached by each reinforced wall in terms of shear stress and drift. The reported shear stress corresponds to the maximum observed value, and the drift corresponds to the ultimate stress or 80% of the maximum observed stress, since the wall becomes unstable beyond this threshold [13].

The reinforcement code R-M-2 denotes a reinforced wall (R) with mesh connected to masonry (M); R-MC-2 corresponds to a reinforced wall (R) with mesh connected to masonry (M) and the confinement columns (C); and R-MCB-2 refers to a reinforced wall (R) with mesh connected to masonry (M) and to all confinement elements (CB) on both sides (2). On the other hand, R-MC-1 corresponds to a reinforced wall (R) with mesh connected to masonry (M) and the confinement columns (C); and R-MCB-1 refers to a reinforced wall (R) with mesh connected to masonry (M) and to all confinement elements (CB) on one side (1). Reinforcements applied on both sides of the walls

represent the interior walls, while those applied on one side represent the exterior walls, which are only accessible from one side due to the neighboring buildings.

Araoz and Velezmoro [6] were the first to study confined tubular masonry walls reinforced with electrowelded wire mesh to prevent the collapse of confined tubular masonry dwellings. Their research aimed to improve the performance or behavior of these walls, which are highly vulnerable without reinforcement. It is important to note that in their study, the mesh was connected only to the masonry, since it was only intended to increase resistance. Mamani [7], Diaz et al. [9], Diaz et al. [10], and SENCICO [8] also studied confined tubular masonry walls strengthened with electrowelded wire mesh with the objective of improving their behavior. These studies demonstrated that the type of mesh connection and the number of reinforced sides have a significant influence on the capacity of the reinforced walls, producing a notable change in the resistance and deformation capacity.

The following paragraphs describe the performance of the reinforced walls according to the type of mesh connection.

**Reinforced confined tubular masonry with mesh connected to masonry (R-M-2).** This connection type produces a slight increase in the resistance of confined tubular masonry walls. Table I shows a minimum resistance of 0.44 MPa for unreinforced walls, while Table II shows that Wall 7, reinforced on both sides, reached a resistance of 0.69 MPa, representing a modest 57% increase. No studies have been conducted with the mesh connected only to the masonry on one side of the wall.

**Reinforced confined tubular masonry with mesh connected to masonry and confinement columns (R-MC-2, R-MC-1).** This connection type produces a significant increase in the resistance of confined tubular masonry walls. Table I shows a minimum resistance of 0.44 MPa for unreinforced walls, while Table II shows that Wall 8, reinforced on both sides, reached a resistance of 0.90 MPa, representing a substantial 105% increase. In the case of reinforcement on one side, Wall 14 reached a resistance of 0.69 MPa, corresponding to a 57% increase.

**Reinforced confined tubular masonry with mesh connected to masonry and all confinement elements (R-MCB-2, R-MCB-1).** This connection type leads to a significant improvement in both the resistance and drift capacity of confined tubular masonry walls. Table I shows a minimum resistance of 0.44 MPa and a minimum drift of 0.0015 for unreinforced walls, while Table II shows that Wall 10, reinforced on both sides, reached a resistance of 0.84 MPa and a drift of 0.0053, corresponding to increases of 91% and 253%, respectively. In the case of one-sided reinforcement on one side, Wall 11 achieved a resistance of 0.70 MPa and a drift of 0.0026, resulting in increases of 60% and 73%, respectively.

Finally, it is important to note that the comparison between unreinforced and reinforced walls is only referential, as they were tested under different conditions; i.e., they differ in the amount of steel in the confinement columns, masonry resistance, axial load, and the amount of mesh used. Accordingly, when reinforced walls on both sides are tested under similar conditions, those mesh connected to both the masonry and all confinement elements are expected to exhibit the greatest resistance and deformation capacity, while those with mesh connected only to the masonry should show the least. However, this trend is not reflected in the results presented in Table II, where Walls 7, 8, and 9 demonstrate greater deformation capacity than Wall 10. The average drift value is close to that recommended by Diaz [16], who recommends considering a drift of 0.0050 for walls reinforced with electrowelded wire mesh. Fig. 2 shows bilinear models of the capacity curves for the reinforced walls listed in the previous table.

### *C. Calibrated Masonry Models*

For model calibration using statistical regression methods, it is first necessary to identify the dependent and independent variables. In this case, the dependent variables are already defined as the shear resistance and deformation of confined tubular masonry walls. Therefore, it remains to identify the independent variables and the appropriate regression method to adequately estimate the resistance and deformation of these walls. In this regard, three studies are presented

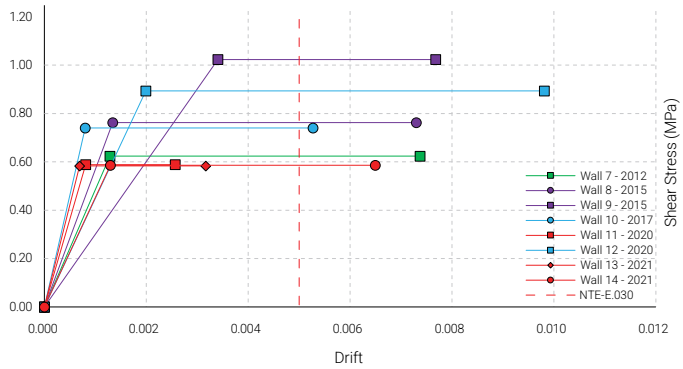


Fig. 2. Bilinear models of capacity curves for reinforced confined tubular masonry walls.

$$\frac{\tau_{max}}{F_m} = 0.0038 + 0.26 * \left(\frac{P_t * \sigma_y}{F_m}\right) + 0.14 * \left(\frac{P_{we} * \sigma_{wy}}{F_m}\right) + 0.089 * \left(\frac{\sigma_0}{F_m}\right) \quad (1)$$

$$\Delta_{max} = 0.00041 + 0.0057 * \left(\frac{h}{l}\right) \quad (2)$$

$$\frac{\tau_u}{F_m} = 0.050 + 0.026 * \left(\frac{h}{l}\right) + 0.010 * \left(\frac{P_t * \sigma_w}{F_m}\right) + 0.008 * \left(\frac{\sigma_0}{F_m}\right) \quad (3)$$

$$\frac{\tau}{F_m} = \beta_0 + \beta_1 * \left(\frac{P_t * \sigma_y}{F_m}\right)^{0,7} + \beta_2 * \left(\frac{P_{we} * \sigma_{wy}}{F_m}\right) + \beta_3 * \left(\frac{\sigma_0}{F_m}\right) \quad (4)$$

below, each proposing models to determine wall capacity based on specific independent variables.

Sugano et al. [17] calibrated a confined masonry model using multiple linear regression. The model's maximum resistance ($\tau_{max}$) is expressed as a function of the amount of longitudinal and transverse steel reinforcement in the confinement columns ($P_t.\sigma_y$, $P_{we}.\sigma_{we}$), the axial load ($\sigma_0$), and the compressive strength of the masonry prism ($F_m$). The maximum drift ($\Delta_{max}$) is expressed as a function of the wall (h/l), as evidenced in Equations (1) and (2).

Cardenas et al. [18] also calibrated a confined masonry model using multiple linear regression. The model's ultimate resistance ($\tau_u$) is based on the wall aspect ratio (h/l), the amount of longitudinal steel resistance in the confinement columns ($P_t.\sigma_y$), the axial load ($\sigma_0$), and the compressive strength of the masonry prism ($F_m$), as evidenced in Equation (3). The ultimate drift ($\Delta_u$) was not calibrated.

Diaz et al. [19] also calibrated a confined masonry model using multiple linear regression. However, this study was more comprehensive, since it calibrated the cracking, yielding, maximum, and ultimate resistance. The model's resistance ($\tau_{max}$) is based on the amount of longitudinal and transverse steel resistance in the confinement columns ($P_t.\sigma_y$, $P_{we}.\sigma_{we}$), the axial load ($\sigma_0$), and the compressive strength of the masonry prism ($F_m$), as evidenced in Equation (4). The corresponding drifts of the model ($\Delta$) are fixed values for each resistance state.

Overall, the capacity of confined masonry walls is mainly a function on the wall aspect ratio, the amount of longitudinal and transversal steel reinforcement in the confinement columns, the axial load, and the compressive strength of the masonry prism. Moreover, multiple linear regression is an appropriate statistical method for determining the capacity of confined masonry walls.

## III. Methodology

The research aims to create a model capable of determining the capacity of unreinforced and reinforced tubular masonry walls strengthened with electrowelded wire mesh. To achieve this, the independent variables must first be identified to form the dimensionless parameters. Subsequently, the most appropriate regression method is selected to perform the calibration of the confined tubular masonry wall model. The background information presented above is essential for identifying the independent variables and appropriate dimensionless parameters, as well as for selecting the most suitable regression method for model calibration.

### *A. Dependent and Independent Variables*

The dependent variables in this study are the resistance and deformation capacity, as the objective is to determine the capacity of confined tubular masonry walls. The independent variables were previously identified by the authors cited in the background section. Accordingly, in Equations (5) and (6), the dependent variables are expressed as functions of the independent variables—i.e., the strength and drift as a function of the amount of longitudinal ($P_t = A_s / t.l$) and transverse ($P_{we} = A_{we} / t.s$) steel of the columns; the yield resistance of the longitudinal ($\sigma_y$) and transverse ($\sigma_{wy}$) steel of the columns, the axial load ($\sigma_0$); the compressive strength of the masonry prism ($F_m$); and the wall height (h) and effective length (l = 0.9L). Here, *As* is the area of the longitudinal steel of the columns, *Awe* is the area of the transversal steel of columns, *t* is the wall thickness, *s* is the spacing of the transversal steel of columns, and *L* is the wall length.

### *B. Dimensionless Parameters*

The dimensionless parameters were also identified by the authors cited in the background section. In Equations (7) and (8), the dimensionless parameters are formed from the independent variables described above. It is worth noting that new dimensionless parameters can be formed using the Buckingham π theorem.

$$\tau = f(P_t, \sigma_y, P_{we}, \sigma_{wy}, \sigma_0, F_m, h, l) \quad (5)$$

$$\Delta = f(P_t, \sigma_y, P_{we}, \sigma_{wy}, \sigma_0, F_m, h, l) \quad (6)$$

$$\frac{\tau}{F_m} = f\left(\frac{P_t * \sigma_y}{F_m}, \frac{P_{we} * \sigma_{wy}}{F_m}, \frac{\sigma_0}{F_m}, \frac{h}{l}\right) \quad (7)$$

$$\Delta = f\left(\frac{P_t * \sigma_y}{F_m}, \frac{P_{we} * \sigma_{wy}}{F_m}, \frac{\sigma_0}{F_m}, \frac{h}{l}\right) \quad (8)$$

$$y = \beta_0 + \beta_1 * x_1 + \beta_2 * x_2 + \beta_3 * x_3 + \ldots + \beta_m * x_m \quad (9)$$

### *C. Regression Methods*

The models were calibrated using various regression methods, such as simple linear regression, simple nonlinear regression, multiple linear regression, multiple nonlinear regression, and polynomial regression. Among these, the simple linear regression method is the least complex since it relates a dependent variable to an independent variable (two variables) in a linear way. Conversely, the multiple nonlinear regression method is the most complex since it relates a dependent variable to several independent variables (more than two variables) in a nonlinear way [20].

Given that more than two independent variables were defined in the previous section, only the multiple linear regression, multiple nonlinear regression, and polynomial regression methods are applicable. In addition, the reviewed literature indicates that the multiple linear regression method provides an adequate representation of masonry walls. Consequently, this method was selected for the present calibration. The equations used to determine the regression parameters ($\beta_0$, $\beta_1$, $\beta_2$, and $\beta_3$), the standard error (SE), the coefficient of multiple determination ($R^2$), and the multiple correlation coefficient (R) are presented below. Equation (9) shows the expression of the multiple linear regression method. Here, *y* is the independent variable; $x_i$ ($x_1$, $x_2$, $x_3$, ...+$x_m$) are the independent variables; $\beta_i$ ($\beta_1$, $\beta_2$, $\beta_3$, ..., $\beta_m$) are the regression parameters; and *m* is the number of independent variables.

$$
\begin{aligned}
y_1 &= \beta_0 + \beta_1 * x_{11} + \beta_2 * x_{12} + \ldots + \beta_m * x_{1m} \\
y_2 &= \beta_0 + \beta_1 * x_{21} + \beta_2 * x_{22} + \ldots + \beta_m * x_{2m} \\
&\vdots \\
y_n &= \beta_0 + \beta_1 * x_{n1} + \beta_2 * x_{n2} + \ldots + \beta_m * x_{nm}
\end{aligned}
$$

$$
\begin{Bmatrix} y_1 \\ y_2 \\ \vdots \\ y_n \end{Bmatrix} = \begin{bmatrix} x_{11} & x_{12} & \cdots & x_{1m} \\ x_{21} & x_{22} & \cdots & x_{2m} \\ \vdots & \vdots & \vdots & \vdots \\ x_{n1} & x_{n2} & \cdots & x_{nm} \end{bmatrix} * \begin{Bmatrix} \beta_0 \\ \beta_1 \\ \vdots \\ a_m \end{Bmatrix} \rightarrow \{A\}_{nx1} = [B]_{nxm} * \{X\}_{mx1} \tag{10}
$$

$$
\rightarrow [B]^T * \{A\}_{nx1} = [B]^T * [B]_{nx\mathrm{m}} * \{X\}_{mx1}
$$

**Regression parameters ($\beta_i$).** The regression parameters can be determined using the least squares method or, alternatively, through a matrix approach, as shown in Equation (10). Here, $y$ is the independent variable; $x_i$ ($x_1$, $x_2$, $x_3$, ..., $x_m$) are the independent variables; $\beta_i$ ($\beta_1$, $\beta_2$, $\beta_3$, ..., $\beta_m$) are the regression parameters; $m$ is the number of independent variables; $n$ is the number of equations; $\{A\}$ is the vector of dependent variable values; $\{B\}$ is the matrix of independent variable values; and $\{X\}$ is the vector of the coefficients.

**SE.** The SE measures the dispersion, i.e., the variation between the calculated and experimental results [20]. In Equation (11), y represents the experimental values, $y^\wedge$ are calculated values, $e$ is the error between the experimental and calculated value, $n$ is the number of groups in the sample, and $p$ is the number of estimated parameters.

**$R^2$ and R.** $R^2$ represents the proportion of the total variation of the dependent variable that depends on the other variables involved in the regression equation [20]. This coefficient changes between zero and unity, with values closer to unity indicating a good fit. Here, $Se$ is the SE, $Sy^2$ is the variance of the dependent variable, $y$ is the mean of the independent variable, $y^\wedge$ is the calculated values, and $n$ is the number of groups in the sample. $R^2$ and R can be determined using Equation 12.

Table III presents all the samples used in the model calibration, expressed in megapascals (MPa). Cross-validation was not applied due to the limited number of samples. Likewise, regularization was not implemented to exclude irrelevant independent variables, as the independent variables identified in the research by Sugano et al. [17] and Diaz et al. [19]—already validated in previous research—were considered.

$$
Se = \sqrt{\frac{\sum (y - \hat{y})^2}{n - p}} = \sqrt{\frac{\sum e^2}{n - p}} \tag{11}
$$

$$
R^2 = 1 - \frac{Se^2}{Sy^2} = 1 - \frac{\frac{\sum (y - \hat{y})^2}{n - p}}{\frac{\sum (y - \bar{y})^2}{n - 1}} \tag{12}
$$

## IV. Results and Discussion

The proposed model is bilinear, and only the point where the ascending and horizontal lines intersect is calibrated—i.e., only the yield point is calibrated. The ultimate point maintains the same resistance, while the drift is a fixed value obtained from the studies presented in the background section. This section is organized into three parts. The first presents the results and discussion of the dimensionless parameters considered in the calibration of the unreinforced and reinforced confined tubular masonry wall model. The second focuses on the yield resistance calibration, and the third discusses the yield drift calibration.

### A. *Dimensionless Parameters of Confined Tubular Masonry Walls*

The dimensionless parameters used to determine the capacity of unreinforced confined masonry walls are the same as those proposed by Sugano et al. [17] and Diaz et al. [19]. However, to consider the reinforcement, an additional dimensionless

TABLE III

SAMPLES FOR CALIBRATION OF THE NUMERICAL MODEL

| Wall | Author | $F_m$ | $P_t.s_y$ | $P_{we}.s_{wy}$ | $s_0$ | $e.P_h.s_{yh}$ |
|---|---|---|---|---|---|---|
| 1 | Salinas & Lazares (2008) | 2.167 | 0.821 | 0.917 | 0.405 | 0.000 |
| 2 | Salinas & Lazares (2008) | 3.256 | 0.821 | 0.917 | 0.405 | 0.000 |
| 3 | Araoz & Velezmoro (2012) | 2.354 | 0.826 | 1.048 | 0.000 | 0.000 |
| 4 | Zavala et al. (2014) | 3.027 | 0.820 | 0.879 | 0.681 | 0.000 |
| 5 | Diaz et al. (2017) | 2.200 | 0.492 | 0.839 | 0.750 | 0.000 |
| 6 | Diaz et al. (2020) | 3.600 | 0.826 | 0.839 | 0.700 | 0.000 |
| 7 | Araoz & Velezmoro (2012) | 2.354 | 0.568 | 0.721 | 0.000 | 0.029 |
| 8 | Mamani (2015) | 2.648 | 0.568 | 0.721 | 0.259 | 0.074 |
| 9 | Mamani (2015) | 2.648 | 0.568 | 0.721 | 0.377 | 0.074 |
| 10 | Diaz et al. (2017) | 2.200 | 0.349 | 0.595 | 0.530 | 0.086 |
| 11 | Diaz et al. (2020) | 3.600 | 0.649 | 0.659 | 0.550 | 0.036 |
| 12 | Diaz et al. (2020) | 3.600 | 0.534 | 0.543 | 0.450 | 0.059 |
| 13 | SENCICO (2021) | 3.600 | 0.586 | 0.595 | 0.350 | 0.038 |
| 14 | SENCICO (2021) | 3.600 | 0.586 | 0.595 | 0.350 | 0.038 |

parameter must be introduced to represent the electrowelded wire mesh. Accordingly, a new parameter is incorporated, similar to that used for the steel of the confinement columns, but including an additional variable representing the type of connection of the electrowelded wire mesh to the wall. This variable represents the efficiency factor $e$ of the mesh, which reflects whether the mesh is connected only to the masonry, to both the masonry and the confinement columns, or to the masonry and all the confinement elements. Equations (13) and (14) present the relationships between the dependent and independent variables for unreinforced and reinforced confined tubular masonry walls with electrowelded wire mesh.

According to Diaz [21], the resistance of walls in which the mesh is connected only to the masonry is reduced to 45%, while that of the walls where the mesh is connected to the masonry and confinement columns is reduced to 65%, compared to walls where the mesh is connected to both the masonry and all confinement elements. Thus, the efficiency factor $e$ is defined as follows: $e$ is equal to unity when the mesh is connected to the masonry and all confinement elements ($e$ = 1.00); $e$ is equal to 0.65 when the mesh is connected to the masonry and confinement columns ($e$ = 0.65);

$$\frac{\tau}{F_m} = f\left(\frac{P_t * \sigma_y}{F_m}, \frac{P_{we} * \sigma_{wy}}{F_m}, \frac{\sigma_0}{F_m}, \frac{e * P_h * \sigma_{yh}}{F_m}\right) \quad (13)$$

$$\Delta = f\left(\frac{P_t * \sigma_y}{F_m}, \frac{P_{we} * \sigma_{wy}}{F_m}, \frac{\sigma_0}{F_m}, \frac{e * P_h * \sigma_{yh}}{F_m}\right) \quad (14)$$

and $e$ is equal to 0.45 when the mesh is connected only to the masonry ($e$ = 0.45).

*B. Calibration of Yield Resistance*

The bilinear model was calibrated using 14 tests conducted at UNI and PUCP. Six tests correspond to unreinforced walls and eight to reinforced tubular masonry walls confined with electrowelded wire mesh featuring different connection types between the mesh and the wall. The behavior curves of the 14 walls were converted to bilinear using the methodology proposed by ASCE/SEI 41-13 [13]. Furthermore, the statistical method of multiple linear regression was employed to calibrate this model, since it is widely used to calibrate the confined masonry wall models, as evidenced in the literature reviewed.

Table IV presents the dependent dimensionless parameter and the four independent dimensionless parameters used for model

TABLE IV

Dependent and Independent Dimensionless Parameters for Calibration – Resistance

| Author | $t_y/F_m$ | $(P_t.s_y/F_m)^{0.7}$ | $P_{we}.s_y/F_m$ | $s_0/F_m$ | $(e.P_h.s_{yh}/F_m)^{0.7}$ |
|---|---|---|---|---|---|
| Salinas & Lazares (2008) | 0.227 | 0.507 | 0.423 | 0.187 | 0.000 |
| Salinas & Lazares (2008) | 0.144 | 0.381 | 0.282 | 0.124 | 0.000 |
| Araoz & Velezmoro (2012) | 0.202 | 0.480 | 0.445 | 0.000 | 0.000 |
| Zavala et al. (2014) | 0.190 | 0.351 | 0.381 | 0.341 | 0.000 |
| Diaz et al. (2017) | 0.111 | 0.357 | 0.233 | 0.194 | 0.000 |
| Diaz et al. (2020) | 0.127 | 0.401 | 0.290 | 0.225 | 0.000 |
| Araoz & Velezmoro (2012) | 0.265 | 0.370 | 0.306 | 0.000 | 0.232 |
| Mamani (2015) | 0.288 | 0.340 | 0.272 | 0.098 | 0.414 |
| Mamani (2015) | 0.386 | 0.340 | 0.272 | 0.142 | 0.414 |
| Diaz et al. (2017) | 0.337 | 0.276 | 0.271 | 0.241 | 0.526 |
| Diaz et al. (2020) | 0.163 | 0.301 | 0.183 | 0.153 | 0.201 |
| Diaz et al. (2020) | 0.248 | 0.263 | 0.151 | 0.125 | 0.284 |
| SENCICO (2021) | 0.162 | 0.281 | 0.165 | 0.097 | 0.210 |
| SENCICO (2021) | 0.163 | 0.281 | 0.165 | 0.097 | 0.210 |

$$\frac{\tau_y}{F_m} = -0.049 + 0.206 * \left(\frac{P_t * \sigma_y}{F_m}\right)^{0,7} + 0.370 * \left(\frac{P_{we} * \sigma_{wy}}{F_m}\right) + 0.029 * \left(\frac{\sigma_0}{F_m}\right) + 0.483 * \left(\frac{e * P_h * \sigma_{yh}}{F_m}\right)^{0,7} \quad (15)$$

calibration. The first and last independent dimensionless parameters were raised to a number equal to 0.7, which improved the fit between the calculated and experimental values. Table V summarizes the regression parameters, SE, $R^2$, and R obtained for the yield resistance model of unreinforced and reinforced confined tubular masonry walls with electrowelded wire mesh. Finally, Equation (15) presents the calibrated model for calculating the yield resistance, incorporating the regression parameters and the dimensionless parameters that represent the longitudinal and transverse steel of the confinement columns, the axial load, the compressive strength of the masonry prism, and the electrowelded wire mesh.

Table V shows that $R^2$ is close to unity, indicating a strong fit between the observed and predicted values, in accordance with the confined masonry models proposed by Sugano et al. [17], Cardenas et al. [18], and Diaz et al. [19].

The dimensionless parameters in Equation (15) are consistent with those used in previous studies, except for the last one that represents

TABLE V

Calibration Results – Resistance

| Regression parameters | | SE | | $R^2$ | | R | |
|---|---|---|---|---|---|---|---|
| $b_0$ | -0.049 | | | | | | |
| $b_1$ | 0.206 | | | | | | |
| $b_2$ | 0.370 | SE | 0.03336 | $R^2$ | 0.88351 | R | 0.93995 |
| $b_3$ | 0.029 | | | | | | |
| $b_4$ | 0.483 | | | | | | |

the contribution of the electrowelded wire mesh to the wall resistance. In the equation, the factor *e* refers to the mesh efficiency, $P_h$ to the ratio ($P_h = A_h / t.S$), and $\sigma_{yh}$ to the yield resistance of the electrowelded wire mesh. $A_h$ represents the steel area of the mesh, *t* the wall thickness, and *S* the mesh spacing.

*C. Calibration of Yield Drift*

This section presents the results of the yield drift calibration for the unreinforced and reinforced

TABLE VI

Dependent and Independent Dimensionless Parameters for Calibration – Drift

| Author | $D_y$ ($10^{-3}$) | $(P_t.s_y/F_m)^{0,7}$ | $P_{we}.s_y/F_m$ | $s_0/F_m$ | $(e.P_h.s_{yh}/F_m)^{0,7}$ |
|---|---|---|---|---|---|
| Salinas & Lazares (2008) | 0.659 | 0.507 | 0.423 | 0.187 | 0.000 |
| Salinas & Lazares (2008) | 0.848 | 0.381 | 0.282 | 0.124 | 0.000 |
| Araoz & Velezmoro (2012) | 0.589 | 0.480 | 0.445 | 0.000 | 0.000 |
| Zavala et al. (2014) | 0.373 | 0.351 | 0.381 | 0.341 | 0.000 |
| Diaz et al. (2017) | 0.729 | 0.357 | 0.233 | 0.194 | 0.000 |
| Diaz et al. (2020) | 0.431 | 0.401 | 0.290 | 0.225 | 0.000 |
| Araoz & Velezmoro (2012) | 1.287 | 0.370 | 0.306 | 0.000 | 0.232 |
| Mamani (2015) | 1.340 | 0.340 | 0.272 | 0.098 | 0.414 |
| Mamani (2015) | 3.405 | 0.340 | 0.272 | 0.142 | 0.414 |
| Diaz et al. (2017) | 0.800 | 0.276 | 0.271 | 0.241 | 0.526 |
| Diaz et al. (2020) | 0.811 | 0.301 | 0.183 | 0.153 | 0.201 |
| Diaz et al. (2020) | 1.990 | 0.263 | 0.151 | 0.125 | 0.284 |
| SENCICO (2021) | 0.692 | 0.281 | 0.165 | 0.097 | 0.210 |
| SENCICO (2021) | 1.294 | 0.281 | 0.165 | 0.097 | 0.210 |

$$\Delta_y = \left[-0.454 + 6.087 * \left(\frac{P_t * \sigma_y}{F_m}\right)^{0.7} - 3.984 * \left(\frac{P_{we} * \sigma_{wy}}{F_m}\right) - 0.510 * \left(\frac{\sigma_0}{F_m}\right) + 3.183 * \left(\frac{e * P_h * \sigma_{yh}}{F_m}\right)^{0.7}\right] * 10^{-3} \quad (16)$$

confined tubular masonry wall model. Table VI lists the dependent and independent parameters used for calibration through the multiple linear regression method.

Table VII shows that $R^2$ is not close to unity, indicating that the fit between experimental and calculated values is not strong. However, it is considered an acceptable value, since it is closer to unity than those reported by other authors. Sugano et al. [17] obtained values of $R = 0.4300$ and $R^2 = 0.1849$, both of which are very far from unity. It is important to note that the fit was not satisfactory because a large number of independent variables were considered, while only a limited number of samples or experimental data were available for model calibration. In addition, the confined walls constructed with tubular bricks exhibited erratic behavior under vertical loads, since they suddenly collapsed under significant vertical loads without developing their full deformation capacity.

Equation (16) presents the model used to determine the yield drift. The dimensionless parameters are the same as those used in the yield resistance model; only the regression parameters change.

Accordingly, Fig. 3 illustrates the bilinear model, which is constructed based on three points. The first point corresponds to the origin, which is not determined; the second is the yield point, determined with Equations (15) and (16); and the third is the last point, constructed using Equation (15) for resistance and drift recommendations by Zavala et al. [5] and Diaz [16], i.e., a drift of 0.0037 for unreinforced walls and 0.0050 for walls reinforced with electrowelded wire mesh.

The numerical model applies to confined tubular masonry walls with characteristics similar to those of the walls used in the calibration process. The applicable range is as follows: $2.16 < F_m < 3.60$; $0.34 < P_t.\sigma_y < 3.83$; $0.54 < P_{we}.\sigma_{wy} < 1.05$; $0.0 < \sigma_0 < 0.75$; and $0.00 < e.P_h.\sigma_{yh} < 0.09$. The range of values can be verified in Table III.

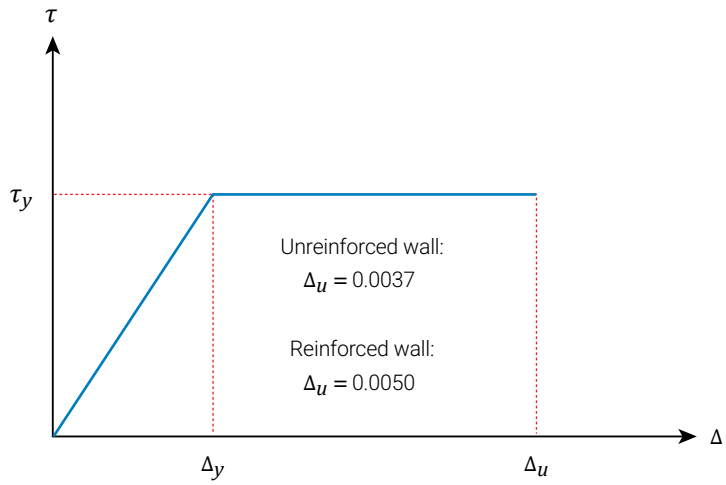


Fig. 3. Bilinear model of unreinforced and reinforced confined tubular masonry walls

## V. Conclusions

The multiple linear regression method proved suitable for calibrating confined tubular masonry wall models unreinforced and reinforced with electrowelded wire mesh. The resistance and drift of these walls depend on the longitudinal and transverse steel reinforcement in the confinement columns, the axial load, the compressive strength of the masonry prism, and the amount of the electrowelded wire mesh. The efficiency variable accounts for the type of connection used for the electrowelded wire mesh in the confined tubular masonry wall, which has a significant impact on the wall capacity. This study and its numerical model are limited by the fact that only isolated single-panel walls with aspect ratios close to unity were analyzed, and cross-validation was not applied due to the small sample size. Therefore, it is recommended future tests to be conducted on confined tubular masonry walls with multiple panels and aspect ratios different from unity to obtain a bilinear model with a wider and more reliable application range.

TABLE VII

Calibration Results – Drift

| Regression Parameters ($10^{-3}$) | | SE ($10^{-3}$) | | $R^2$ | | R | |
|---|---|---|---|---|---|---|---|
| $b_0$ | -0.454 | | | | | | |
| $b_1$ | 6.087 | | | | | | |
| $b_2$ | -3.984 | SE | 0.00073 | $R^2$ | 0.41806 | R | 0.64658 |
| $b_3$ | -0.510 | | | | | | |
| $b_4$ | 3.183 | | | | | | |

## References

[1] Servicio Nacional de Capacitación para la Industria de la Construcción (SENCICO), "Norma Técnica E.070 Albañilería," Ministerio de Vivienda, Construcción y Saneamiento, Lima, Peru, 2006. [Online]. Available: http://blog.pucp.edu.pe/blog/wp-content/uploads/sites/82/2008/01/Norma-E-070-MV-2006.pdf

[2] Instituto Nacional de Estadística e Informática (INEI), "Censos Nacionales 2017: XII de Población, VII de Vivienda y III de Comunidades Indígenas," INEI, Lima, Peru, 2018. [Online]. Available: https://censo2017.inei.gob.pe/resultados-definitivos-de-los-censos-nacionales-2017/

[3] F. Arias Schreiber, "7 de cada 10 viviendas en el Perú son autoconstruidas: los limeños tardan 16 años en levantar el primer

piso", *Infobae*, Jun. 2, 2024. [Online]. Available: https://www.infobae.com/peru/2024/06/03/7-de-cada-10-viviendas-en-el-peru-son-autoconstruidas-los-limenos-tardan-16-anos-en-levantar-el-primer-piso/

[4] W. Angulo, "Capeco: El 70% de viviendas en Lima son informales y vulnerables a un terremoto," *RPP*, Sep. 26, 2017. [Online]. Available: https://rpp.pe/economia/economia/capeco-el-70-de-viviendas-en-lima-son-construidas-sin-normas-tecnicas-noticia-1078934?ref=rpp

[5] C. Zavala, M. Diaz, E. Flores, and L. Cardenas, "Damage limit states for confined masonry walls based on experimental test," *Journal of Disaster Research*, vol. 29, no. 2, pp. 135–141, 2019, doi http://dx.doi.org/10.21754/tecnia.v29i2.715

[6] T. A. Araoz Escobedo and J. P. Velezmoro Girón, "Reforzamiento de viviendas existentes construidas con muros confinados hechos con ladrillos pandereta – segunda etapa," *Undergraduate thesis*, Pontificia Universidad Católica del Perú, Lima, Peru, 2012. [Online]. Available: http://hdl.handle.net/20.500.12404/1203

[7] P. Mamani Quina, "Comportamiento mecánico de muros de albañilería tubular confinada reforzados con malla electrosoldada ante cargas sísmicas y gravitacionales," *Master's thesis*, Pontificia Universidad Católica del Perú, Lima, Peru, 2015. [Online]. Available: http://hdl.handle.net/20.500.12404/6324

[8] Servicio Nacional de Capacitación para la Industria de la Construcción (SENCICO), "Ensayos estructurales de especímenes de albañilería reforzados con malla electrosoldada por una sola cara," Ministerio de Vivienda, Construcción y Saneamiento, Lima, Peru, 2021. [Online]. Available: https://www.gob.pe/institucion/sencico/informes-publicaciones/2290691-ensayos-estructurales-de-especimenes-de-albanileria-reforzados-con-malla-electrosoldada-por-una-sola-cara

[9] M. Diaz, C. Zavala, J. Gallardo, and L. Lavado, "Experimental study of non-engineered confined masonry walls retrofitted with wire mesh and cement-sand mortar," in *Proceedings of the 16th World Conference on Earthquake Engineering (16WCEE)*, Santiago, Chile, 2017. [Online]. Available: https://www.wcee.nicee.org/wcee/article/16WCEE/WCEE2017-2950.pdf

[10] M. Diaz, C. Zavala, and E. Flores, "Structural assessment of confined masonry retrofitting under multi-seismic scenarios in Metropolitan Lima Area," in *Proceedings of the 17th World Conference on Earthquake Engineering (17WCEE)*, Sendai, Japan, 2020. [Online]. Available: https://www.cismid.uni.edu.pe/wp-content/uploads/2021/10/3b-0076.pdf

[11] H. Tavera, "Evaluación del peligro asociado a los sismos y efectos secundarios en Perú," Instituto Geofísico del Perú, Lima, Peru, 2014. [Online]. Available: https://portal.indeci.gob.pe/wp-content/uploads/2019/01/fil20140926131431.pdf

[12] Á. F. San Batolomé, D. Quiun, and W. Silva, *Diseño y construcción de estructuras sismorresistentes de albañilería*, 2nd ed. Lima, Peru: Fondo Editorial de la Pontificia Universidad Católica del Perú, 2018. [Online]. Available: https://hdl.handle.net/20.500.14657/170319

[13] American Society of Civil Engineers, *Seismic Evaluation and Retrofit of Existing Buildings*, Reston, VA, USA: ASCE, 2014. [Online]. Available: https://doi.org/10.1061/9780784412855

[14] R. Salinas and F. Lazares, "Seismic performance of confined masonry buildings with tubular bricks in developing areas," in *Proceedings of the 14th World Conference on Earthquake Engineering (14WCEE)*, Beijing, China, 2008. [Online]. Available: https://www.iitk.ac.in/nicee/wcee/article/14_05-04-0003.PDF

[15] C. Zavala, L. Lavado, J. Taira, J., L. Cardenas, and M. Diaz, "Comparison of behaviors of non-engineered masonry tubular block walls and solid engineered walls,"

*Journal of Disaster Research*, vol. 9, no. 6, pp. 1025–1021, 2014. [Online]. Available: https://pdfs.semanticscholar.org/7cfc/ad6b25b0b7659e17366b9810da545f1faf5b.pdf

[16] C. M. Diaz, "Modelo elastoplástico para la estimación de la capacidad por corte de muros de ladrillo pandereta," *Undergraduate thesis*, Pontificia Universidad Católica del Perú, Lima, Peru, 2021. [Online]. Available: http://hdl.handle.net/20.500.12404/19466

[17] S. Sugano, T. Saito, C. Zavala, and L. Cardenas, L, "Strength and deformation of confined brick masonry walls subjected to lateral forces – Review of existing test data in Japan and Peru," *Journal of Disaster Research*, vol. 9, no. 6, pp. 984–992, 2014. [Online]. Available: https://doi.org/10.20965/jdr.2014.p0916

[18] L. Cardenas, R. Reyna, L. Estacio, and C. Zavala, "Implementation of database of masonry walls test – Review of existing test data in Peru," *Journal of Disaster Research*, vol. 9, no. 6, pp. 993–1000, 2014. [Online]. Available: https://doi.org/10.20965/jdr.2014.p0993

[19] M. Diaz, C. Zavala, E. Flores, and L. Cardenas, "Desarrollo de modelos analíticos para muros de mampostería confinada basados en resultados experimentales en la ciudad de Lima," *Tecnia*, vol. 29, no. 2, pp. 23–29, 2019. [Online]. Available: https://doi.org/10.21754/tecnia.v29i2.711

[20] M. Villon, *Hidrología estadística*. Lima, Peru: Ediciones Villón, 2016.

[21] Servicio Nacional de Capacitación para la Industria de la Construcción (SENCICO), "Propuesta técnica de reforzamiento sísmico de muros de albañilería confinada informal, a los que se tiene acceso por una sola cara," Ministerio de Vivienda, Construcción y Saneamiento, Lima, Peru, 2022. [Online]. Available: https://www.gob.pe/institucion/sencico/informes-publicaciones/2718022-propuesta-tecnica-de-reforzamiento-sismico-de-muros-de-albanileria-confinada-informal-a-los-que-se-tiene-acceso-por-una-sola-cara

# Evaluation of the Mechanical and Physical Properties of Concrete Using Seawater as a Replacement of Potable Water with the Addition of Blast Furnace Slag and Metakaolin

Alonso Enrique Marquez Pacheco[1], Bruno Alfredo Palacios Rocha[2], Jose Joao Rengifo Reategui[3]

[1] 20140783@aloe.ulima.edu.pe, [2] 20191483@aloe.ulima.edu.pe, [3] jrengifo@ulima.edu.pe

[123] Universidad de Lima, Perú

Recibido: 03 Mayo 2025 / Publicado: 24 Abril 2026
https://doi.org/10.26439/ciic2025.8665

ABSTRACT. **Concrete is the most widely used construction material worldwide, and its production consumes more than two million tons of fresh water annually—a resource that accounts for only 3% of the planet's available water, compared to 97% of seawater. Furthermore, 75% of freshwater consumption occurs in areas experiencing extreme water scarcity. In Peru, the distribution of water resources is unequal due to the geographic location of water sources relative to population centers, with the coastal region being the most affected since it has the lowest water availability and the highest concentration of inhabitants. This research evaluated, through laboratory testing, the mechanical properties of fresh and hardened concrete mixed with seawater, as a 100% replacement of potable water, and incorporating 30% to 50% blast furnace slag (BFS) and 5% to 15% metakaolin (MK) across eight sample types that varied these three components. The mixture containing seawater, 40% BFS, and 10% MK showed lower workability and reduced compressive strength at 28 days; however, it most closely resembled the control sample, suggesting its potential for future applications.**

KEYWORDS: Concrete, seawater, blast furnace slag, metakaolin, mechanical properties.

THEMATIC AXES: Axis 6: Sustainable construction

## I. Introduction

In the construction sector, concrete is the most widely used material worldwide, and its production consumes more than two million tons of fresh water every year, representing 9% of industrial water use. Moreover, three-quarters of the fresh water employed in concrete manufacturing is extracted from areas experiencing extreme water scarcity. This situation highlights the urgent need to seek alternatives to the use of fresh or potable water in concrete production and curing, particularly in regions facing severe water stress, where potable water should be reserved for human consumption [1]. Although approximately three-quarters of the planet is covered with water, only 3% is suitable for human consumption, while the remaining 97% consists of seawater. In this scenario, the continuous growth of the global population has increased water demand, which—compounded by environmental pollution and poor resource management—fails to meet the needs of many cities around the world. Water stress is expected to become particularly critical by 2025 [2]. The most critical case occurs along the Peruvian coast, where approximately 63% of the country's population resides but only 1.7% of the national water resources are available. This uneven distribution is the result of the geographic

location of water sources and the concentration of the population on the coast, creating high demand in regions with insufficient resources to meet it [3]. Despite scientific evidence supports the concept that seawater is not suitable for reinforced concrete, several ancient structures were successfully built using concrete mixed with seawater— for example, the ancient Roman port of Baiae, in Italy, which dates back 2000 years [4]. This suggests the potential applications of seawater for producing durable concrete. However, its use is largely restricted due to its high chloride content, which promotes corrosion in steel reinforcement. This problem can be mitigated by using seawater in plain (unreinforced) concrete applications or by employing non-corrosive materials such as fiber-reinforced polymer (FRP) bars to reinforce structures. FRP bars offer advantages such as light weight and corrosion resistance, but their high cost hinders their widespread use in the market [5].The use of supplementary cementitious materials (SCMs) to partially replace Portland cement also reduces $CO_2$ emissions associated with concrete manufacturing. Thus, advancing the use of SCMs represents a significant contribution to environmental protection. [6]

Based on these issues, the following research question arises: Can concrete mixed with seawater, adding BFS and MK, achieve properties comparable to concrete mixed with potable water?

## II. Methodology

This research follows an experimental design with a quantitative approach, based on the collection and analysis of numerical data obtained from tests conducted in the Materials Laboratory at the University of Lima. The objective was to evaluate the mechanical and physical properties of fresh and hardened concrete using seawater and incorporating BFS and MK. The experimental design allows for the intentional manipulation of independent variables in a controlled environment to analyze their impact on the dependent variables. [7] In this case, the effect of seawater on concrete was analyzed by varying the proportions of BFS and MK as partial replacements for cement. The variables evaluated are presented in Table I.

TABLE I

Dependent and Independent Variables

| Dependent Variables | Test |
|---|---|
| Mechanical properties of concrete | Slump |
| | Compressive strength |
| | Tensile strength |
| **Independent Variables** | **Ranges Studied (%)** |
| Cement | 35-100 |
| BFS | 30-50 |
| MK | 5-15 |
| Type of mixing water | Potable water or seawater |

To carry out this study, information related to the research topic was first gathered from academic sources and indexed journals to establish the theoretical framework and the scope of the research. Then, the materials required for the experimental phase—such as aggregates, binders, and seawater—were obtained and characterized through laboratory tests to determine particle size distribution, moisture content, specific gravity, among other relevant factors. Subsequently, the concrete mixtures for the samples considered in the study were prepared, and their physical and mechanical properties were evaluated. Finally, the results were analyzed and interpreted to answer the research question.

The experimental design included eight sample types, divided into two main groups: those prepared with potable water and those with seawater. Each sample had a different composition since the proportions of the cementitious materials—Portland cement, BFS, and MK—and the type of mixing water varied. BFS was incorporated at proportions ranging from 30% to 50%, and MK from 5% to 15%, following previous studies such as those by Pereira Silva [8] and Li [9]. In both cases, these percentages are regarded as optimal, since higher contents of BFS and MK tend to reduce cement properties and compressive strength, while lower percentages render their effects almost negligible [8], [10], [11], [12], [13], [14], [15], [16], [17]. A detailed presentation of these samples is shown in Table II.

TABLE II

COMPOSITION OF THE SAMPLE TYPES

| Sample | Mixing Water | Cement (%) | BFS (%) | MK (%) |
|---|---|---|---|---|
| P1 | Potable | 100 | – | – |
| P2 | Potable | 65 | 30 | 5 |
| P3 | Potable | 50 | 40 | 10 |
| P4 | Potable | 35 | 50 | 15 |
| M1 | Seawater | 100 | – | – |
| M2 | Seawater | 65 | 30 | 5 |
| M3 | Seawater | 50 | 40 | 10 |
| M4 | Seawater | 35 | 50 | 15 |

To designate each sample type, acronyms were used to indicate their composition. The first four samples correspond to those prepared with potable water, labeled "P," and numbered from 1 to 4 according to the proportions of the cementitious materials. Similarly, the last four samples were prepared with seawater, labeled "M," and numbered from 1 to 4 following the same criterion.

*A. Materials*

**Aggregates**. The fine aggregate used was coarse sand, with a specific gravity of 2.09, a water absorption of 1.47%, and a fineness modulus of 2.85. On the other hand, the coarse aggregate consisted of crushed stone, with a specific gravity of 1.70 and a maximum nominal size of 1 in.

Table III presents the retained weights for each sieve, the residue, and the total weight obtained for both the fine and coarse aggregates, ensuring that the test error remained less than or equal to 0.3%, as specified in the NTP 400.012 standard [18], thereby validating the results. Additionally, Fig. 1 shows the comparison of aggregate sizes, where the curve was generated by plotting sieve opening size on the X-axis against the passing percentage on the Y-axis.

**Seawater.** To characterize the extracted seawater, tests were conducted in the Environmental Laboratory at the University of Lima, including measurements of conductivity, pH, turbidity, and dissolved oxygen. The results obtained are presented in Table IV.

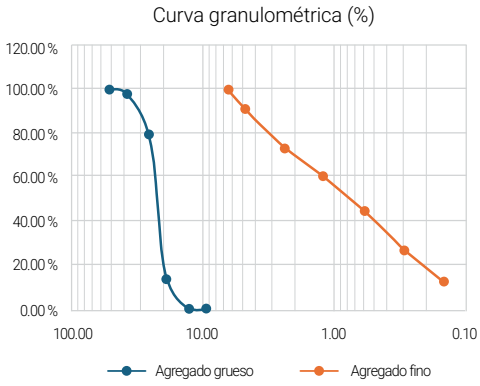


Fig. 1. Granulometry of the aggregates.

TABLE III

GRANULOMETRY OF THE AGGREGATES

| Fine Aggregate (500 gr) | | Coarse Aggregate (10 kg) | |
|---|---|---|---|
| Sieve | Retained Weight (g) | Sieve (in) | Retained Weight (g) |
| No. 4 | 45.5 | 2 | 0 |
| No. 8 | 85.2 | 1½ | 0 |
| No. 16 | 70.6 | 1 | 2.181 |
| No. 30 | 68.0 | ¾ | 6.357 |
| No. 50 | 84.8 | ½ | 1.44 |
| No. 100 | 71.0 | 3/8 | 0 |
| Residue | 74.7 | Residue | 0.024 |
| Total | 499.8 | Total | 10.0017 |

TABLE IV

CHARACTERIZATION OF SEAWATER

| Properties | Measured Value |
|---|---|
| Conductivity | 54.71 mS/cm |
| pH | 7.61 |
| Turbidity | 0.31 NTU |
| Dissolved oxygen | 9.66 mg/L |

**BFS.** Laboratory tests were performed to determine the physical properties of BFS, which showed a density of 2.56 g/cm³, a water absorption of 3.82%, and a porosity of 20.5%, as summarized in Table V.

To determine the chemical composition of BFS, an X-ray fluorescence (XRF) spectrometry test was carried out. This analysis allowed the quantification of the elements in the sample, yielding a calcium oxide (CaO) concentration of 43.41% and a silicon dioxide ($SiO_2$) concentration of 24.02%, among other compounds, as detailed in Table VI.

MK. MK was obtained by calcinating kaolin in a muffle furnace at 700 °C. To verify the effective formation of MK, Fourier-transform infrared (FTIR) spectroscopy was performed on both kaolin and MK samples. Before calcination, kaolin exhibits characteristic FTIR bands in the regions of 3695–3620 $cm^{-1}$, associated with O–H bonds of structural water; 1030–1000 $cm^{-1}$ from Si–O vibrations; and 540–500 $cm^{-1}$ from Al–O vibrations. After calcination, kaolin loses water and transforms into an amorphous structure (MK). The disappearance of O–H bands and the presence of new bands or changes in Si–O and Al–O vibrations confirm the dihydroxylation of kaolin and its conversion into MK [19]. The test results and the confirmation of the transformation process from kaolin to MK are shown in Fig. 2 and Fig. 3.

*B. Mix Design*

The samples were prepared following the ACI 211.1 (2014) method for concrete with a strength of 210 kg/cm² (21 MPa). Considering a slump range between 25 and 100 mm, a water-to-cement ratio of 0.45, a maximum nominal coarse aggregate size of 1 in., and a fineness modulus of 2.85 for the fine aggregate, the resulting cementitious material content was 423.88 kg per 1 m³, with corresponding variations in the proportions of the cementitious materials. Additionally, a plasticizer admixture, Sikament-290N, with a density of 1.20 g/cm³ was used in a dosage of 1% of the cementitious material by weight. The mixes were prepared in 40 L batches according to the specified mix design, with the proportions of each material adjusted for that batch size.

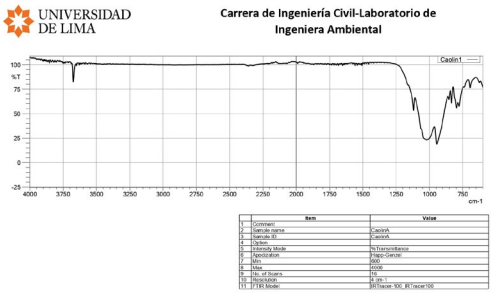


Fig. 2. FTIR spectrum of the Kaolin sample.

TABLE V
PHYSICAL PROPERTIES OF BFS

| Properties | Value |
|---|---|
| Density (g/cm³) | 2.56 |
| Absorption (%) | 3.82 |
| Porosity (%) | 20.50 |

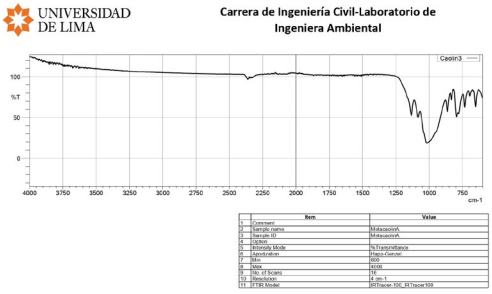


Fig. 3. FTIR spectrum of the MK sample.

TABLE VI
CHEMICAL COMPOSITION OF BFS

| Component | (%) |
|---|---|
| CaO | 43.41 |
| $SiO_2$ | 24.02 |
| $Al_2O_3$ | 18.61 |
| MgO | 10.84 |
| $Fe_2O_3$ | 2.67 |
| $SO_3$ | 0.32 |
| $TiO_2$ | 0.13 |

TABLE VII

MIX DESIGN

| Sample | Cementitious Materials (kg) | | | Water (L) | Aggregates (kg) | | Water–Cement Ratio |
|---|---|---|---|---|---|---|---|
| | Cement | BFS | MK | | Fine | Coarse | |
| P1 | 423.88 | - | - | 190.75 | 501.66 | 718.25 | 0.45 |
| P2 | 275.52 | 127.16 | 21.19 | 190.75 | 501.66 | 718.25 | 0.45 |
| P3 | 211.94 | 169.55 | 42.39 | 190.75 | 501.66 | 718.25 | 0.45 |
| P4 | 148.36 | 211.94 | 63.58 | 190.75 | 501.66 | 718.25 | 0.45 |
| M1 | 423.88 | - | 0.00 | 190.75 | 501.66 | 718.25 | 0.45 |
| M2 | 275.52 | 127.16 | 21.19 | 190.75 | 501.66 | 718.25 | 0.45 |
| M3 | 211.94 | 169.55 | 42.39 | 190.75 | 501.66 | 718.25 | 0.45 |
| M4 | 148.36 | 211.94 | 63.58 | 190.75 | 501.66 | 718.25 | 0.45 |

*Note.* The table presents the weights of cementitious materials (in kg), water (in L), aggregates (in kg), and the water–cement ratio for each sample type.

TABLE VIII

PROPERTIES TO BE EVALUATED

| Property | Standard | Description |
|---|---|---|
| Fresh State | | |
| Slump | NTP 339.035:2015 | This test involves filling a mold with fresh concrete, removing it, and measuring the distance between the mold and the settled concrete. |
| Hardened State | | |
| Compressive strength | NTP 339.034:2015 | This test consists of applying a gradually increasing load to a cylindrical concrete sample until it fractures, thus determining its capacity to withstand compressive forces. |
| Tensile strength | NTP 339.084:2017 | This test measures the concrete's ability to resist tensile forces by applying a load until it breaks. |

*Note.* Adapted from Instituto Nacional de Calidad [20], [21], [22].

The tests used to evaluate the properties of concrete were carried out in the laboratories at the University of Lima, assessing both the fresh and hardened states. The slump, compressive strength, and tensile strength tests were conducted in the Civil Engineering Materials Laboratory.

## III. Results and Discussion

### *A. Fresh-State Properties*

**Slump.** The slump values obtained from the test for each mix type are shown in Table IX.

As shown in Fig. 4, an increase in the percentage of BFS and MK in the mixes leads to higher workability. Furthermore, it is observed that seawater mixes—regardless of the percentage of cementitious materials used—show 44% lower workability compared to potable-water mixes. Initially, this reduced workability could make them more difficult to handle on site, particularly for pumping operations. However, as the BFS and MK content increases, workability becomes more suitable—by up to 20% in potable-water mixes and 85% in seawater mixes. The optimal slump depends on the specific application of the concrete. In this study, a range between 3 and 5 inches was considered appropriate.

TABLE IX

SLUMP TEST RESULTS

| Sample | Slump (in) |
|---|---|
| P1 | 6.25 |
| P2 | 6.75 |
| P3 | 7.25 |
| P4 | 7.50 |
| M1 | 3.50 |
| M2 | 4.50 |
| M3 | 6.00 |
| M4 | 6.50 |

*B. Hardened-State Properties*

**Compressive strength.** The compressive strength values at 7, 14, and 28 days, along with a summary for each mix type, are presented in Table X.

In Fig. 5, the compressive strength of the eight mix types is compared at 7, 14, and 28 days. It can be observed that analogous potable-water and seawater mixes with equivalent percentages of BFS and MK show similar results. In all four cases, the seawater mixes display higher strength at early ages; however, over time, their strength increases only slightly and ultimately becomes lower than that of potable-water mixes. The target design strength is 21 MPa.

On the other hand, despite the differences in several factors among the studies cited in Table XI—such as the water–cement ratio, curing days, percentage of cementitious materials used, and the fact that either BFS or MK was employed individually—it is still possible to make certain comparisons. Initially, it can be observed that the compressive strength results obtained in this research are 72% lower for seawater mixes and 74% lower for potable-water mixes compared with those reported in the referenced studies. This difference may be explained by various factors, such as human error during mix preparation, curing conditions, or the fact that, in previous studies, the cementitious materials were used separately, whereas in this research they were used in combination.

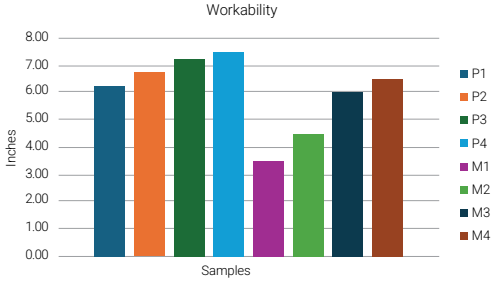


Fig. 4. Slump values in inches for each mix type.

TABLE X

SUMMARY OF COMPRESSIVE STRENGTH (MPA) FOR EACH MIX TYPE

| Sample | Compressive Strength (MPa) | | |
|---|---|---|---|
| | 7 Days | 14 Days | 28 Days |
| P1 | 31.01 | 38.75 | 45.18 |
| P2 | 21.14 | 24.46 | 30.92 |
| P3 | 14.37 | 17.93 | 20.52 |
| P4 | 7.64 | 9.56 | 11.60 |
| M1 | 37.67 | 39.94 | 43.25 |
| M2 | 24.17 | 27.51 | 30.85 |
| M3 | 16.31 | 18.85 | 19.80 |
| M4 | 8.69 | 10.22 | 11.79 |

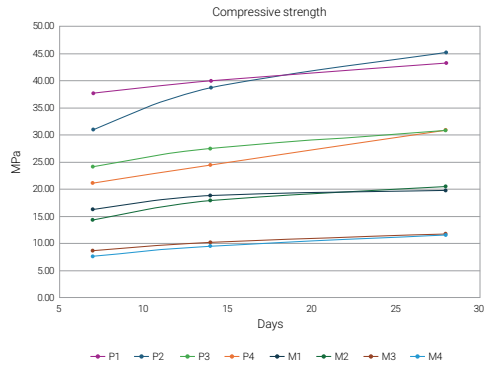


Fig. 5. Compressive strength (MPa) of each mix type at 7, 14, and 28 days.

TABLE XI

Comparison of Results Reported by Other Authors

| Author | Water–Cement Ratio | Cementitious Material (%) | Strength (MPa) | Days |
|---|---|---|---|---|
| Authors Using BFS as a Cementitious Material | | | | |
| Lizarazo Marriaga and Claisse (2011) [11] | 0.30 | 30 | 49.8 | 120 |
| | | 50 | 46.7 | |
| | | 30 | 65.3 | |
| | 0.50 | 50 | 55.6 | |
| Li et al. (2000) [13] | 0.35 | 50 | 34.97 | 28 |
| | | 60 | 32.26 | |
| | | 70 | 26.37 | |
| Lee et al. (2006) [17] | 0.42 | 30 | 44.9 | 28 |
| | | 50 | 44.6 | |
| | 0.37 | 30 | 56.3 | |
| | | 50 | 57.1 | |
| | 0.32 | 30 | 64.3 | |
| | | 50 | 66.7 | |
| | 0.27 | 30 | 72.6 | |
| | | 50 | 76.2 | |
| Authors Using MK as a Cementitious Material | | | | |
| Asghari et al. (2023) [10] | 0.55 | 5 | 48.28 | 28 |
| | | 10 | 51.91 | |
| | | 15 | 54.53 | |
| | 0.40 | 5 | 42.6 | |
| | | 11 | 43.9 | |
| | | 15 | 45.9 | |
| Mejía de Gutiérrez et al. (2009) [12] | 0.40 | 10 | 59.2 | 28 |
| | | | 54.0 | |
| | | | 51.4 | |
| | | | 32.0 | |
| Li et al. (2015) [15] | 0.45 | 5 | 61.32 | 28 |
| | | | 69.95 | |
| Li et al. (2015) [9] | 0.45 | 5 | 57.23 | 28 |
| | | | 69.49 | |

**Tensile strength.** Table XII presents the tensile strength values for each mix type.

In Fig. 6, it can be observed that both groups of mixes exhibit a decreasing trend in tensile strength as the percentage of BFS and MK increases—up to 53% for potable-water mixes and 61% for seawater mixes. An exception is the control seawater mix, which shows the highest tensile strength. In all other cases, seawater mixes display lower tensile strength than their potable-water counterparts. The optimal tensile strength is approximately 10% of the compressive strength; in this study, this corresponds to about 2.1 MPa.

TABLE XII

SUMMARY OF TENSILE STRENGTH (MPA) FOR EACH MIX TYPE

| Sample | Tensile Strength (MPa) |
|---|---|
| P1 | 2.66 |
| P2 | 2.62 |
| P3 | 1.73 |
| P4 | 1.24 |
| M1 | 3.14 |
| M2 | 2.23 |
| M3 | 1.25 |
| M4 | 1.22 |

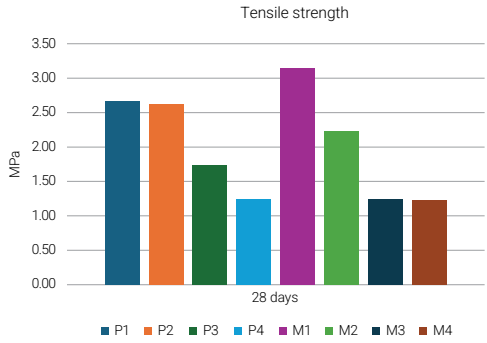


Fig. 6. Tensile strength (MPa) of each mix type.

## IV. CONCLUSIONS

The use of seawater reduced workability by 44% compared to the mix prepared with potable water, due to the accelerated hydration process caused by the salts present in seawater. However, the addition of BFS and MK increased workability by up to 20% in potable-water mixes and 85% in seawater mixes. Seawater improved compressive strength at early ages (7 and 14 days) compared to potable-water mixes; however, this trend decreased at later ages. The addition of higher percentages of BFS and MK led to reductions in compressive strength of up to 72% for seawater mixes and 74% for potable-water mixes. The effect of seawater on tensile strength resulted in an 18% increase compared to potable-water mixes. Nevertheless, at higher percentages of BFS and MK addition, tensile strength decreased by up to 53% for potable-water mixes and 61% for seawater mixes. Although the mixes containing BFS and MK (P2 and M2) showed lower compressive and tensile strength values compared to the control samples (P1 and M1), they still met the mechanical and physical properties for which they were designed. These results demonstrate that the use of supplementary cementitious materials and seawater is feasible under appropriate design criteria, without compromising the required structural performance.

Recommendations and Acknowledgements

- It is recommended to further evaluate the effects of seawater combined with BFS and MK in reinforced concrete, particularly regarding corrosion and concrete durability.
- The authors express their sincere appreciation to the Environmental and Materials Laboratories at the University of Lima for their valuable support throughout the development of this research. The staff's commitment, technical guidance, and generous access to the laboratory facilities were essential to the proper execution of the tests, allowing the research to be conducted with rigor and success. Thanks to this collaboration, it was possible to achieve the proposed objectives and obtain solid and reliable results.

## REFERENCES

[1] S. Rathnarajan and P. Sikora, "Seawater-mixed concretes containing natural and sea sand aggregates – a review," *Results in Engineering*, vol. 20, Art. no. 101457, Dec. 2023, doi: https://doi.org/10.1016/j.rineng.2023.101457

[2] Y. Elsaje, S. Ismail, H. Soussa, M. Gado, and A. Balah, "Water desalination in Egypt; literature review and assessment," *Ain Shams Engineering Journal*, vol. 14, no. 7, Art. no. 101998, Jul. 2023, doi: https://doi.org/10.1016/j.asej.2022.101998

[3] Autoridad Nacional del Agua, *Plan nacional de recursos hídricos del Perú: memoria 2013*, 2013. [Online]. Available: https://www.ana.gob.pe/sites/default/files/plannacionalrecursoshidricos2013.pdf

[4] S. Chae, M. Emwas, E. Gotti, P. Guttmann, M. Jackson, M. Kunz, P. Levitz, C. Meral, P. Monteiro, J. Moon, R. Taylor, and H. Wenk, "Material and Elastic Properties of Al-Tobermorite in Ancient Roman Seawater Concrete," *Journal of the American Ceramic Society,* vol. 96, no. 7, pp. 2598-2606, May 2013. doi: https://doi.org/10.1111/jace.12407

[5] A. Younis, U. Ebead, P. Suraneni, and A. Nanni, "Fresh and hardened properties of seawater-mixed concrete," *Construction and Building Materials,* vol. 190, pp. 276-286, Nov. 2018, doi: https://doi.org/10.1016/j.conbuildmat.2018.09.126

[6] K. P. Fattah, A. K. Al-Tamimi, W. Hamweyah, and F. Iqbal, "Evaluation of sustainable concrete produced with desalinated reject brine," *International Journal of Sustainable Built Environment,* vol. 6, no. 1, pp. 183-190, Jun. 2017, doi: https://doi.org/10.1016/j.ijsbe.2017.02.004

[7] R. Hernández Sampieri, C. Fernández Collado and P. Baptista Lucio, *Metodología de la investigación,* 6th ed. México: McGraw-Hill, 2014. [Online]. Available: https://apiperiodico.jalisco.gob.mx/api/sites/periodicooficial.jalisco.gob.mx/files/metodologia_de_la_investigacion_-_roberto_hernandez_sampieri.pdf

[8] L. H. Pereira Silva, V. Nehring, F. F. Guedes de Paiva, J. R. Tamashiro, A. P. Galvín, A. López Uceda, and A. Kinoshita, "Use of blast furnace slag in cementitious materials for pavements - Systematic literature review and eco-efficiency," *Sustainable Chemistry and Pharmacy,* vol. 33, Art. no. 101030, Jun. 2023, doi: https://doi.org/10.1016/j.scp.2023.101030

[9] Q. Li, H. Geng, Z. Shui, and Y. Huang, "Effect of metakaolin addition and seawater mixing on the properties and hydration of concrete," *Applied Clay Science,* vol. 115, pp. 51-60, Oct. 2015, doi: https://doi.org/10.1016/j.clay.2015.06.043

[10] Y. Asghari, S. E. Mohammadyan-Yasouj, and S. S. Rahimian Koloor, "Utilization of metakaolin on the properties of self-consolidating concrete: A review," *Construction and Building Materials,* vol. 389, Art. no. 131605, Jul. 2023, doi: https://doi.org/10.1016/j.conbuildmat.2023.131605

[11] J. Lizarazo Marriaga and P. Claisse, "Influencia de la adición de escoria de alto horno en la penetración de los cloruros en el concreto," *Revista Ingeniería e investigación,* vol. 31, no. 2, pp. 38-47, Aug. 2011. Available: https://www.redalyc.org/articulo.oa?id=64322334005

[12] R. Mejía de Gutiérrez, C. Rodríguez, E. Rodríguez, J. Torres, and S. Delvasto, "Concreto adicionado con metacaolín: Comportamiento a carbonatación y cloruros," *Revista de la Facultad de Ingeniería de la Universidad de Antioquia,* vol. 48, Apr. 2009. Available: http://www.scielo.org.co/scielo.php?pid=S0120-62302009000200006&script=sci_arttext

[13] D. Li, J. Shen, Y. Chen, L. Cheng, and X. Wu, "Study of properties on fly ash–slag complex cement," *Cement and Concrete Research,* vol. 30, no. 9, pp. 1381-1387, Sep. 2000. Available: https://doi.org/10.1016/S0008-8846(00)00360-4

[14] T. Nishida, N. Otsuki, H. Ohara, Z. M. Garba-Say, and T. Nagata, "Some considerations for applicability of seawater as mixing water in concrete," *Journal of Materials in Civil Engineering,* vol. 27, no. 7, Dec. 2013, doi: https://doi.org/10.1061/(ASCE)MT.1943-5533.0001006

[15] Q. Li, H. Geng, Y. Huang, and Z. Shui, "Chloride resistance of concrete with metakaolin addition and seawater mixing: A comparative study", *Construction and Building Materials,* vol. 101, no. 1, pp. 184-192, Dec. 2015, doi: https://doi.org/10.1016/j.conbuildmat.2015.10.076

[16] C. L. Page, N. R. Short, and W. R. Holden, "The influence of different cements on chloride-induced corrosion of reinforcing steel," *Cement and Concrete Research,* vol. 16, no. 1, pp. 79-86, Jan. 1986, doi: https://doi.org/10.1016/0008-8846(86)90071-2

[17] K. M. Lee, H. K. Lee, S. H. Lee, and G. Y. Kim, "Autogenous shrinkage of concrete containing granulated blast-furnace slag," *Cement and Concrete Research,* vol. 36, no. 7, pp. 1279-1285, Jul. 2006, doi: https://doi.org/10.1016/j.cemconres.2006.01.005

[18] Instituto Nacional de Calidad, Dirección de Normalización, *Norma Técnica Peruana NTP 400.012: AGREGADOS. Análisis granulométrico del agregado fino, grueso y global*, Perú, 2017.

[19] A. M. Rashad, "Metakaolin as cementitious material: History, scours, production and composition – A comprehensive overview," *Construction & Building Materials,* vol. 41, pp. 303-318, Apr. 2013, doi: https://doi.org/10.1016/j.conbuildmat.2012.12.001

[20] Instituto Nacional de Calidad, Dirección de Normalización, *Norma Técnica Peruana NTP 339.035: CONCRETO. Método de ensayo para la medición del asentamiento del concreto de cemento Portland*, Perú, 2015.

[21] Instituto Nacional de Calidad, Dirección de Normalización, *Norma Técnica Peruana NTP 339.034: CONCRETO. Método de ensayo normalizado para la determinación de la resistencia a la compresión del concreto en muestras cilíndricas*, Perú, 2015.

[22] Instituto Nacional de Calidad, Dirección de Normalización, *Norma Técnica Peruana NTP 339.084: CONCRETO. Método de ensayo normalizado para la determinación de la resistencia a tracción simple del concreto, por compresión diametral de una probeta cilíndrica*, Perú, 2017.

# Dynamic Weighing Through Vibration-Based Structural Monitoring in a Prestressed Concrete Road Bridge

Jennifer Marcela López[1], Diana C. Millán[2], Mauricio Marín[3], Johannio Marulanda[4], Peter Thomson[5]

[1] jennifer.marcela.lopez@correounivalle.edu.co, [2] diana.c.millan@correounivalle.edu.co, [3] mauricio.marin@correounivalle.edu.co, [4] johannio.marulanda@correounivalle.edu.co, [5] peter.thomson@correounivalle.edu.co

[12345] Research Group in Seismic, Wind, Geotechnical, and Structural Engineering (G 7), School of Civil and Geomatics Engineering, Universidad del Valle, Colombia.

Recibido: 20 Mayo 2025 / Publicado: 24 Abril 2026
https://doi.org/10.26439/ciic2025.8666

**ABSTRACT. The aim of this study was to implement a vibration-based approach for non-invasive dynamic weighing of a deteriorated prestressed concrete bridge. The research is set within the current context of road infrastructure, which is increasingly impacted by the frequent passage of overloaded vehicles. The proposed methodology relies on the structural vibration response recorded by a monitoring system composed of accelerometers and strain gauges mounted directly on the bridge girders. While commercial Bridge Weigh-In-Motion (B-WIM) systems have demonstrated high accuracy in estimating Gross Vehicle Weight (GVW), their implementation is often constrained by the ideal structural conditions required for proper operation. Moreover, these systems rely primarily on strain measurements, which require more complex and costly instrumentation, particularly in long-span bridges. In contrast, the proposed methodology is based on vibration measurements, which can be obtained using more portable equipment that cover larger areas with fewer sensors. Through numerical simulations and experimental validation, the method achieved high accuracy in estimating both GVW (with errors below 5%) and axle weights (with errors below 10%). The results demonstrate that this methodology is an efficient tool for roadway load monitoring, contributing to the reduction of structural risks and the improvement of road infrastructure management.**

KEYWORDS: Bridges, numerical model, structural health monitoring, technology, vehicle load, weigh in motion (WIM)

THEMATIC AXES: Seismic and structural engineering

## I. Introduction

Bridges are key components of road infrastructure networks, playing a critical role in regional connectivity and economic development. Ensuring their proper operation is essential, as they must withstand vehicular loads without compromising structural integrity or the safety of users. Accurately identifying these loads is crucial, as underestimating them can result in severe structural damage or even catastrophic failure. The collapse of a bridge results not only in the loss of human life but also in substantial

economic consequences, including traffic disruptions, commercial losses, logistical delays, and high reconstruction costs. In the communities affected, the impact extends to reduced mobility and tourism, further amplifying the long-term economic burden.

Globally, multiple bridge collapses caused by overloading and structural deficiencies have underscored the importance of effective load control. For example, the Morandi Bridge in Genoa, Italy (2018), and the Nanfang'ao Bridge in Taiwan (2019) collapsed under heavy vehicular loads, resulting in significant fatalities and infrastructure losses [1], [2]. In Colombia, approximately 20 bridges have collapsed over the past decade, including recent cases such as the El Alambrado bridge (2023), the road bridge over the Charte River in Yopal, and the Guayepo bridge in 2016 [3]. These failures are largely attributed to overloading and deterioration, which have seriously impacted mobility and road safety [4]. A study conducted by the National University of Colombia reported over 13 bridge failures in 2023 alone, nearly 24.4% of which involved road bridges, with overloading identified as a major contributing factor [5]. Similarly, a 2011 study had already identified overload as a contributing factor in 7% of bridge failures [6].

The growing need for effective strategies to manage and monitor vehicular loads is justified by critical factors. These include road safety, given the risks posed by overloading, infrastructure preservation, as excessive loads reduce structural lifespan and increase maintenance costs, and regulatory compliance, which requires reliable tools to enforce legal weight limits. For example, an overload of just one metric ton (1 t) applied to a single axle can increase pavement damage by up to 92% [7]. In this context, collecting data such as GVW, axle loads, and axle spacing has become essential not only for safety assessments but also for fatigue analysis and load-carrying capacity evaluations.

Conventional load identification methods, such as static weigh stations, offer high accuracy but are costly, land-intensive, and often avoided [8], [9]. Their implementation is often impractical in urban or high-traffic areas. As an alternative, Weigh-In-Motion (WIM) systems enable dynamic estimation of vehicle weights without requiring vehicles to stop. These systems, however, still present certain limitations, including the need for pavement modifications, potential traffic disruptions, and the risk of introducing noise or bias into the data [9], [10]. An advanced alternative to WIM is the B-WIM system, which uses the bridge as a weighing scale to estimate axle loads. To achieve this goal, these systems aim to optimize the fit between a finite element model and the structure's experimental response [11], [12], [13]. Based on the methodology proposed by Fred Moses in 1979 [14], B-WIM technology has evolved through modal analysis techniques and dynamic system modeling. Research efforts, including those by S. Law and Chan et al., introduced time-domain identification methods and addressed the dynamic effects of vehicle passage, thereby enhancing the accuracy of axle weight identification [15], [16], [17]. In Europe, the WAVE project significantly advanced the field by eliminating the need for pavement sensors [18]. More recently Yang Yu enhanced estimation accuracy by incorporating influence surfaces that account for a vehicle's transverse position on the bridge [19]. B-WIM systems have now been implemented in more than 20 countries for traffic analysis, overload detection, and infrastructure planning [20], [21].

Despite their benefits, traditional B-WIM systems rely heavily on ideal structural conditions, limiting their applicability on deteriorated bridges. Structural defects, surface roughness, and approach geometry generate signal noise and present significant challenges for modeling accuracy [12]. Additionally, conventional B-WIM approaches typically are based on strain responses, which require the installation of strain gauges—sensors that are highly sensitive and must be positioned precisely so that vehicle axles pass directly over them to enable precise weight identification. Such an approach often requires a large number of sensors, thereby increasing system complexity and cost. By comparison, a vibration-based method provides enhanced practicality, as accelerometers can monitor broader areas with fewer devices, facilitating implementation on longer-span bridges. This work addresses these limitations by proposing a noninvasive, vibration-based B-WIM methodology applied to a deteriorated prestressed concrete bridge located

in Cali, Colombia. By integrating structural monitoring data from accelerometers and strain gauges with numerical model calibration, the system estimates vehicle speed, axle loads, and GVW. This method is validated under real conditions and provides a practical solution for bridge load monitoring without traffic disruption or invasive interventions. The hypothesis is that, even in deteriorated structures, accurate dynamic weight estimations can be achieved through calibrated modeling and response monitoring, thereby contributing to safer and more sustainable infrastructure management.

## II. Methodology

In the process of estimating vehicular loads on bridges, vehicle identification is essential, requiring information such as speed, number of axles, and axle spacing. The accuracy of these data has a significant impact on the precision of the weight estimates [22]. For a vehicle weight estimation to be considered reliable, a complete identification of the vehicle is required, with a margin of error of less than 10% [23].

Vehicle identification was carried out using structural vibrations measured through the peak-to-peak method. A band-pass filter between 22 and 60 Hz was applied to the acceleration records to remove low- and high-frequency components. The frequency range limits were defined based on the dynamic properties of the structure, which were obtained through the Stochastic Subspace Identification (SSI) technique. The 22 Hz value corresponds to the highest frequency among the predominant modes identified experimentally as shown in Table I, while 60 Hz was set as the upper limit as frequencies above this threshold contribute minimally, as shown in the acceleration signal spectrum in Fig. 1. This filtering process effectively isolated the signal components generated by the passage of vehicle axles. Vehicle speed was calculated based on the time delay between the signal peaks corresponding to the vehicle's entry and exit from the bridge [23]. Using this speed and the time intervals between the peaks produced by each axle, the axle spacing may be accurately calculated.

TABLE I
Identified Operational Frequencies

| Mode | Frequency (Hz) |
|---|---|
| 1 | 5.90 |
| 2 | 6.21 |
| 3 | 7.80 |
| 4 | 11.55 |
| 5 | 14.83 |
| 6 | 16.44 |
| 7 | 21.90 |

*Note*: Data extracted from [22].

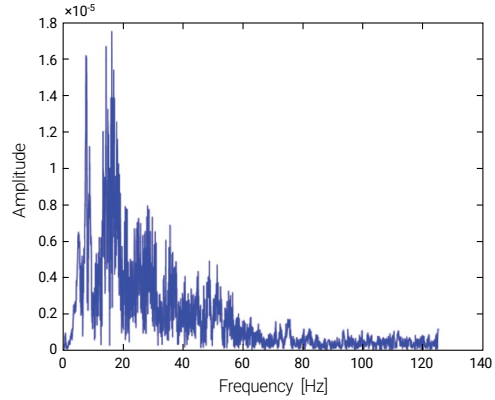


Fig. 1. Acceleration spectrum.

For load identification, based on Moses' algorithm, the static weight of each axle is determined by solving (1). In this equation, *A* represents the weight per axle, and the sum of these axle weights yields the GVW.

$$M = F * A \tag{1}$$

The terms of the equation are defined through the following expressions.

$$F = [F_{ij}] = \sum_{k=1}^{T} IS_i(k - C_i) IS_j(k - C_j) \tag{2}$$

$$M = [M_j] = \sum_{k=1}^{T} M_k IS_i(k - C_i) \tag{3}$$

$$C_i = \frac{D_i f}{v} \tag{4}$$

Where $IS_i\ (k - C_i)$ represents the ordinate of the influence surface, constructed from a numerical model of the structure, at the position of the $i$-th axle at time instant $k$; $D_i$ corresponds to the distance between the first axle and the $i$-th axle; $f$ is the sampling frequency of the acquisition system, and $v$ is the constant speed of the vehicle.

The influence surface was generated using the method proposed by O'Brien et al. [24], in which the model's response to a truck load of known weight is expressed by (5). To reduce calculation errors, (6) is used to compare the measured response with the theoretical response.

$$M_k = \sum_{i=1}^{N} A_i IS_i\ (k - C_i) \tag{5}$$

$$E = \sum_{k=1}^{K} (M_k^M - M_k^T)^2 \tag{6}$$

The general process for estimating vehicle weight is illustrated in Fig. 2, which considers three key factors: vehicle parameters, influence surface, and global bridge response. In this work, the global response is obtained by analyzing strain signals recorded by strain gauges installed on the beams at the bridge midspan, where the maximum response occurs during vehicle passage. These signals are compared with the influence surface obtained from the responses of the calibrated numerical bridge model, which accurately represents the structural behavior of the bridge. Using this information, together with vehicle identification, the dynamic weighing algorithm is applied to estimate the axle loads and GVW.

## III. Instrumented Bridge

This study focuses on an instrumented bridge in Cali, Colombia, which exhibits significant deterioration in its riding surface and steep longitudinal gradient. The structure's permanent instrumentation enabled continuous structural monitoring without disrupting traffic flow. The structure is located on the 16th Street, between Avenues 102 and 103, and serves north-south traffic. Based on the information provided by local residents, the bridge was estimated to have been built in 1999. The structure consists of a deck with prefabricated concrete slabs, with two traffic lanes, an exclusive bicycle lane, and a pedestrian sidewalk. The superstructure consists of a system of seven prestressed concrete I-beams and two intermediate braces, as shown in Fig. 3.

### *A. Monitoring System and Data Transmission*

The permanent monitoring instrumentation installed on the bridge consists of five triaxial accelerometers and 24 strain gauges (12 for strain measurement and 12 for temperature compensation). These sensors enable the continuous recording of vibrations and deformations, respectively. The Waleker SMA-551 accelerometers have a nominal sensitivity of 1000 mV/g, can measure acceleration ranges of ±2 g and ±4 g, and feature a dynamic range greater than 90 dB within a frequency range of 0–250 Hz, as shown in Fig. 4(a). PL-90-11-2LJQTA strain gauges were selected for the concrete strain measurements. These sensors have a strain limit of 2% (20,000 × $10^6$ με) and use a two-wire connection for power supply and data transmission. The strain gauges were bonded to the bridge surface and protected from environmental factors using three layers of protective coating, as shown in Fig. 4(b). The data acquisition and power system for the strain gauges consists of two LORD V-Link-200 nodes, each with eight channels—four configured for differential measurements and four for single-ended measurements. These nodes are equipped with an anti-aliasing filter and an 18-bit analog-to-digital conversion board as shown in Fig. 4(c).

The data collected by the accelerometers and strain gauges are transmitted via a gateway using UTP cables, which converge at an 8-port industrial switch, centralizing all information. From this switch, data are transmitted via a UTP cable to a computer located at the local police station, where they are stored and analyzed. The sensor distribution layout is shown in Fig. 5.

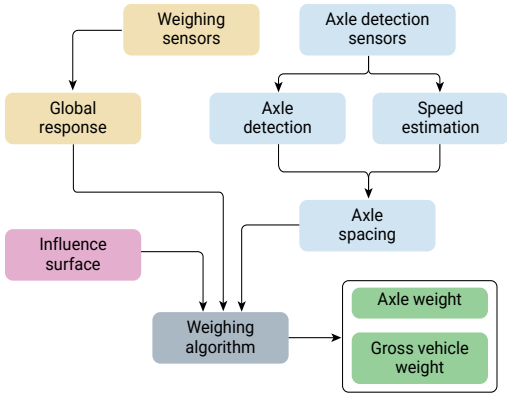


Fig. 2. B-WIM identification diagram.

Fig. 3. Reference bridge located at 16th Street with 102-103 Avenue, Ciudad Jardín, as documented in [25].

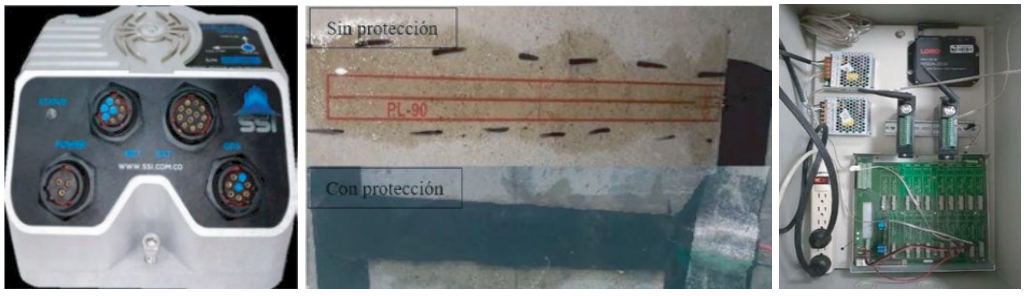


(a) (b) (c)

Fig. 4. Instrumentation equipment: (a) Accelerometer, (b) PL-90-11-2LJQTA strain gauge, (c) Acquisition system.

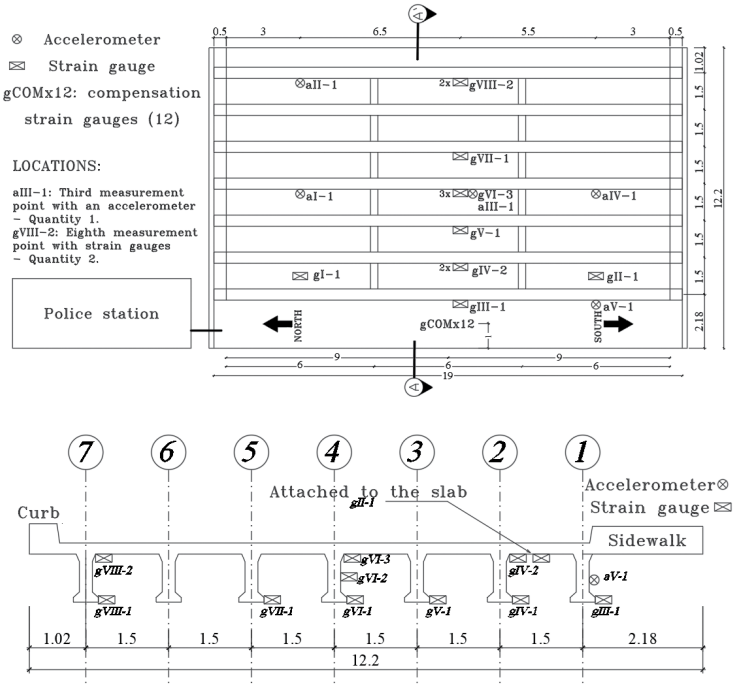


Fig. 5. Instrumentation: (a) Plan view and (b) Elevation View (section A-A), as documented in [22].

Table II presents a summary of the equipment installed.

TABLE II

INSTRUMENTED EQUIPMENT

| Equipment | Function | Location |
|---|---|---|
| Accelerometers | Triaxial measurement devices, designed to measure structural vibrations. | Installed on the web of the girders, near the bridge entrance, the exit, and at mid-span. |
| Equipment | Function | Location |
| Strain gauges | Sensors for measuring concrete strain. | Installed on the bottom flange at mid-span, with additional sensors placed on the slab for temperature compensation. |
| LORD V-LINK200 Node | Powers the strain gauges and supports the connection of up to eight channels. It includes an anti-aliasing filter and an 18-bit analog-to-digital (A/D) converter. | Installed in the acquisition cabinet located on one of the cross braces. |
| Gateway LORD WSDA-2000 | Centralizes the information transmitted by the node. | Installed in the acquisition cabinet located on one of the cross braces. |
| Computer | Used to store and process the signals. | Located at the police station. |

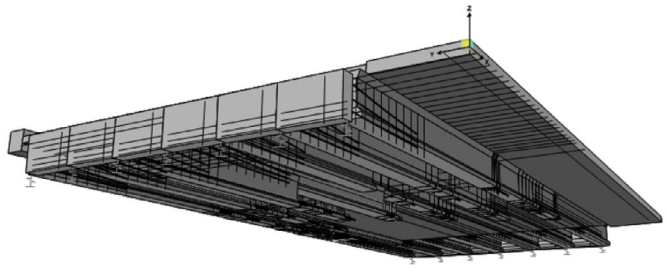

Fig. 6. Numerical model in SAP2000 software.

## IV. Results and Analysis

### *A. Numerical Simulations*

The methodology was evaluated through simulations conducted on a numerical model of the structure, developed using the finite element software SAP2000 and based on the geometric survey, as shown in Fig. 6. The model was constructed using thin-shell elements to represent the beams, diaphragms, and slabs. Springs were assigned at the nodes corresponding to the bottom flange to simulate the behavior of neoprene bearings [22]. Additionally, beam deterioration was incorporated by modeling the cracks identified through visual inspection. The length, thickness, and location of each crack were recorded, and the affected areas were partially removed in the model to represent them accurately. Prestressing cables were also included in the model to account for their structural effects. The cross bracings were represented by a distributed load equivalent to their self-weight, without considering their contribution to the overall stiffness.

Due to the lack of detailed information on material characterization, the material properties were treated as adjustable parameters during model calibration, based on the results of experimental modal identification [22] and field-measured displacements. Eq. (7) and (8) show the objective functions used for these calibrations, respectively.

$$F = \sum_{i=1}^{5} \left| \frac{fn_{ei} - fn_{ai}}{fn_{ei}} \right| + \sum_{i=1}^{5} 1 - MAC\left(\varphi_{ei}, \varphi_{ai}\right) \quad (7)$$

$$D \quad \sum_{i=1}^{6} \left| \frac{D_e - D_a}{D_e} \right| \quad (8)$$

Where $fn_{ei}$ and $fn_{ai}$ are the i-th experimental and analytical frequencies, respectively, and MAC is a statistical measure that evaluates the agreement between two mode shapes, specifically, the shapes of the experimental modes ($\varphi_{ei}$) and those of the analytical modes ($\varphi_{ai}$), expressing their similarity on a scale from 0 to 1, where 1 indicates perfect correlation, and values near 0 indicate little or no similarity. The equation used for its calculation is presented in (9).

$$MAC_{j,k} = \frac{(\varphi_{ei}^T \varphi_{ai})^2}{\varphi_{ei}^T \varphi_{ei} \varphi_{ai}^T \varphi_{ai}} \quad (9)$$

To calibrate the dynamic properties, variables such as material characteristics, elastic modulus, self-weight, and the vertical stiffness of the supports were considered. The results of the calibration are summarized in Table III.

TABLE III
Calibration Results

| Mode | Frequency difference (%) | MAC |
|---|---|---|
| 1 | 4.66 | 0.97 |
| 2 | 1.22 | 0.86 |
| 3 | 1.75 | 0.92 |
| 4 | 1.10 | 0.84 |
| 5 | 18.0 | 0.85 |
| Average | 5.35 | 0.89 |

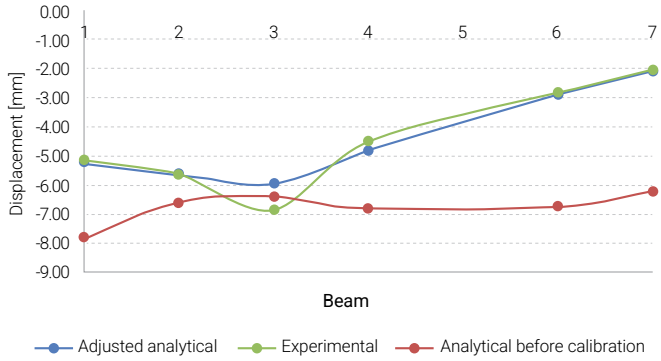


Fig. 7. Displacement adjustment at the midspan of the beams.

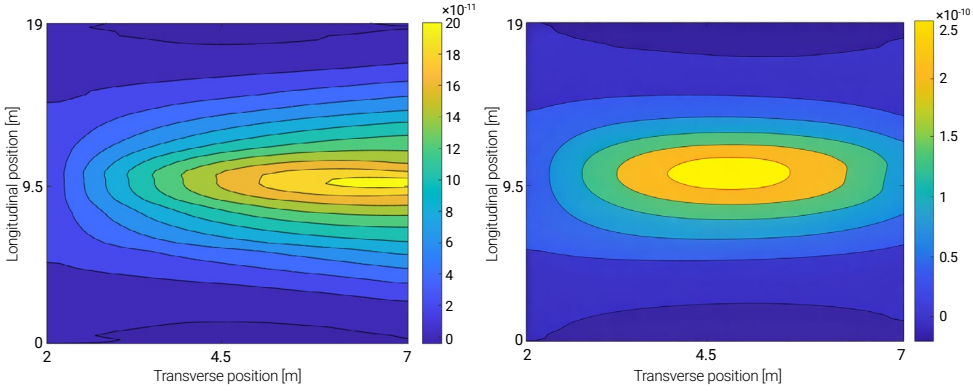


Fig. 8. Influence surface of B2 and B3.

The static adjustment was performed by varying the prestressing force in the beams, resulting in the configuration shown in Fig. 7.

To construct the bridge's influence surface, numerical simulations were conducted with a vehicle crossing at a speed of 1 m/s along different transverse positions. From these simulations, influence lines (ILs) were generated based on the strain response at the center of the bridge. These lines were then aligned to obtain the influence surfaces corresponding to each beam. Fig. 8 shows the influence surfaces corresponding to Beam 2 and Beam 3, respectively.

Using the calibrated model, various load scenarios were simulated for a two-axle vehicle with a GVW of 170 kN, distributed as 40 kN on axle 1 and 130 kN on axle 2. The simulations considered the vehicle crossing Beam 2, then Beam 4, and finally Beam 5, at speeds of 5 m/s and 15 m/s.

The vehicle parameters were identified using the previously described peak-to-peak method. Using the influence surface as a reference, the axle loads for each load scenario were estimated. Tables IV and V provide a summary of the main simulated scenarios. The results demonstrate that vehicle speed can be estimated with considerable accuracy using the proposed method. This level of precision is crucial, as errors in speed estimation directly affect the accuracy of load identification: the greater the error in estimated speed, the larger the deviation in the calculated load. Additionally, it was observed that axle-based load identification can yield higher percentage errors compared to the GVW, particularly at higher speeds. Nevertheless, the estimation of GVW was highly accurate.

TABLE IV

Speed Identification from Numerical Simulations

| Scenario | Speed (m/s) | Identified speed (m/s) | Identification difference (%) |
|---|---|---|---|
| 1 | 5 | 4.99 | 0.20 |
| 2 | | 4.94 | 1.20 |
| 3 | | 4.90 | 2.00 |
| Scenario | Speed (m/s) | Identified speed (m/s) | Identification difference (%) |
| 1 | 15 | 14.50 | 3.33 |
| 2 | | 14.62 | 2.53 |
| 3 | | 15.03 | 0.20 |

TABLE V

Load Identification from Numerical Simulations

| Scenario | Speed (m/s) | Identified weight (kN) | | | Identification difference (%) | | |
|---|---|---|---|---|---|---|---|
| | | Axle 1 | Axle 2 | GVW | Axle 1 | Axle 2 | GVW |
| 1 | 4.99 | 39.80 | 130.03 | 169.83 | 0.50 | 0.02 | 0.10 |
| 2 | 4.94 | 43.70 | 125.40 | 169.10 | 9.25 | 3.54 | 0.53 |
| 3 | 4.90 | 44.60 | 124.90 | 169.50 | 11.50 | 3.92 | 0.29 |
| 1 | 14.50 | 36.00 | 137.40 | 173.40 | 10.00 | 5.69 | 2.00 |
| 2 | 14.62 | 45.00 | 126.37 | 171.37 | 12.50 | 2.79 | 0.81 |
| 3 | 15.03 | 37.05 | 133.06 | 170.11 | 7.37 | 2.35 | 0.06 |

*B. Controlled Load Tests*

Controlled load tests were conducted to evaluate the loads. Prior to their execution, a load testing protocol was designed, taking into account the location of the structure within the city and traffic conditions. The number of configurations and tests to be performed was determined by considering static, dynamic, and service tests.

In this test, the structure was subjected to a 17.39-t truck with the load distributed across the two axles. A sampling frequency of 32 Hz was used for the strain recordings, and 250 Hz for the acceleration measurements. Three operational load tests were performed to assess the bridge's response to this type of demand and the frequency at which it is subjected to such loads.

During the dynamic load tests, the fully loaded dump truck traveled along each lane. The tests were conducted during periods selected to minimize traffic disruption as shown in Fig. 9.

*C. Identification of vehicle parameters*

Acceleration signals showed in Fig. 10 revealed distinct peaks corresponding to axle crossings. The time delay between these peaks, combined with the known travel distance (19 m), yielded an accurate estimation of vehicle speed. Similarly, the interval between the first and second axle peaks provided the axle spacing.

The vehicle was identified with a speed of 1.93 m/s and an axle spacing of 4.44 m, which are very close to the actual values of 1.9 m/s and 4.47 m. This demonstrates that the technique accurately identifies these parameters.

TABLE VI
LOAD TEST IDENTIFICATION

| | Speed (m/s) | Axle spacing (m/s) | Axle 1 weight (kN) | Axle 2 weight (kN) | GVW (kN) |
|---|---|---|---|---|---|
| Actual | 1.90 | 4.47 | 3.94 | 13.12 | 17.06 |
| Identified | 1.93 | 4.44 | 4.20 | 12.10 | 16.30 |
| Difference [%] | 1.60 | 0.70 | 6.60 | 7.80 | 4.50 |

Fig. 9. Vehicle used in the load tests, as documented in [22].

*D. Load determination*

The vehicle weight was estimated from the global strain response of the bridge, recorded at a frequency of 32 Hz using strain gauges and processed with the algorithm proposed by Yu et al. [19], as shown in Fig. 11. The axle weight estimation is performed using the influence surface corresponding to the vehicle's transverse position, identified based on the beam exhibiting the maximum response. First, the axle weights are calculated using (5), and then the GVW is determined using (1).

The results presented in Table VI show once again that the percentage differences are higher for individual axle weights than for the GVW. However, these values were very close to the actual values.

## V. CONCLUSIONS

One of the main challenges of B-WIM methodologies is their application in real traffic scenarios, where multiple vehicles travel simultaneously over the structure. This situation generates overlapping signals preventing the accurate identification of the target vehicle. For this reason, in this study, validation was only possible through a single controlled load test. Nevertheless, the results support the conclusion that the applied methodology is viable. Future work will focus on automating the process through tools such as image processing to improve the system's accuracy and efficiency under more complex and dynamic conditions.

A two-phase adjustment of the structure's numerical model was proposed. The first phase was based exclusively on modal information, while the second incorporated the results of a static load test. This approach enabled the achievement of reliable results. It is important to highlight that the accuracy of load estimation depends directly on the load-response relationship, using a properly tuned model.

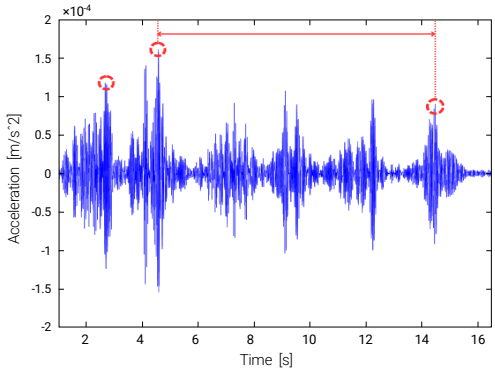


Fig. 10. Vehicle identification in acceleration signals.

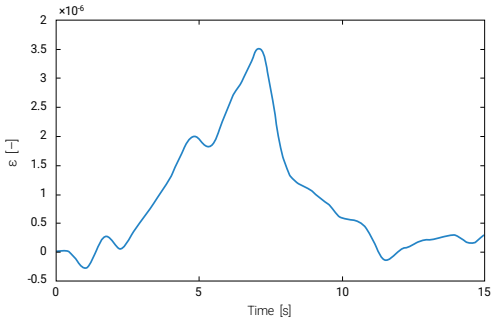


Fig. 11. Global response.

The numerical results confirm that in the process of determining weights, the accuracy of the initial data related to vehicle identification is crucial. In this regard, the vibration sensors used in this process have proven to be portable and accurate devices that, through the peak detection technique employed, enable the estimation of speed and axle spacing with an error margin below 5%.

The results obtained with the proposed methodology demonstrate that vehicular load estimation can be effectively achieved through a vibration- and strain-based system that relies on unit deformations. As a noninvasive and more practical method than commonly used approaches, it simplifies the measurement and implementation process, making it an accessible and efficient alternative for vehicular load estimation.

The application of this methodology to a bridge that does not meet the ideal conditions typically required by B-WIM methodologies, due to its rough deck surface and steep approach slope, presents a significant challenge. However, satisfactory results were obtained, providing a valuable contribution to the field of study.

## References

[1] P. Villani, "El puente de Morandi colapsado en el puerto italiano de Génova: dinámica y causas," presented at Session 30: Bridge Damage Assessment, 26th World Road Congress (PIARC), Abu Dhabi, United Arab Emirates, 2019. [Online]. Available: https://re.public.polimi.it/handle/11311/1102902

[2] S. Prieto, "Publican el informe oficial sobre el colapso del puente Nanfang'ao en Taiwán - Estructurando," *Estructurando*, Dec. 15, 2020. [Online]. Available: https://estructurando.net/2020/12/15/informe-oficia-sobre-el-colapso-del-puente-nanfangao-en-taiwan/

[3] El País, "Puente vehicular caído en Yopal, Casanare, colapsó por sobrepeso," *El País*, Aug. 23, 2016. [Online]. Available: https://www.elpais.com.co/colombia/puente-vehicular-caido-en-yopal-casanare-colapso-por-sobrepeso.html

[4] RCN Radio, "¿Cuántos puentes se han caído en Colombia?," *RCN Radio*, Apr. 18, 2023. [Online]. Available: https://www.rcnradio.com/colombia/puentes-caidos-en-colombia-los-cinco-casos-mas-recordados

[5] P. Héndez, "Fallas de los puentes en Colombia, ¿cuestión de tiempo, monitoreo o apropiación?," *Unal.edu.co*, Sep. 01, 2023. [Online]. Available: https://periodico.unal.edu.co/articulos/fallas-de-los-puentes-en-colombia-cuestion-de-tiempo-monitoreo-o-apropiacion (accessed Jan. 09, 2024).

[6] D. S. Cusba, "Estudio de las causas y soluciones estructurales del colapso total

o parcial de los puentes vehiculares de Colombia desde 1986 al 2011, y la evaluación de las consecuencias del derrumbamiento de uno de ellos," *Bachelor's thesis*, Pontificia Universidad Javeriana, Bogotá, Colombia, 2011. [Online]. Available: https://repository.javeriana.edu.co/bitstreams/136c63a9-6aac-4a4a-863b-af8f736f7d94/download

[7] G. Badilla Vargas, "Incidencia de las estaciones de pesaje móvil en los factores camión en pavimentos de Costa Rica," Informe Técnico UI-03-09, Unidad de Investigación en Infraestructura Vial, Laboratorio Nacional de Materiales y Modelos Estructurales, Universidad de Costa Rica, San José, Costa Rica, Oct. 2009. [Online]. Available: https://www.lanamme.ucr.ac.cr/repositorio/handle/50625112500/1179

[8] A. Lansdell, W. Song, and B. Dixon, "Development and testing of a bridge weigh-in-motion method considering nonconstant vehicle speed," *Engineering Structures*, vol. 152, pp. 709–726, Dec. 2017, doi: https://doi.org/10.1016/j.engstruct.2017.09.044.

[9] S. Lobo and G. Mora, "¡Puentes que nos hablan! Puentes Inteligentes, tecnología aplicada para la administración de la infraestructura vial," *Moviliblog – Inter-American Development Bank Blog*, May 08, 2020. [Online]. Available: https://blogs.iadb.org/transporte/es/puentes-que-nos-hablan-puentes-inteligentes-tecnologia-aplicada-para-la-administracion-de-la-infraestructura-vial/

[10] J. R. Hernández-Jiménez and M. J. Fabela-Gallegos, *Diseño y construcción de un prototipo para determinar el peso de vehículos ligeros en movimiento*, Mexican Institute of Transportation, Secretariat of Communications and Transportation, Technical Publication PT-247, 2004. [Online]. Available: https://www.imt.mx/archivos/publicaciones/publicaciontecnica/pt247.pdf

[12] J. Kim and J. P. Lynch, "Experimental analysis of vehicle–bridge interaction using a wireless monitoring system and a two-stage system identification technique," *Mechanical Systems and Signal Processing*, vol. 28, pp. 3–19, Apr. 2012, doi: https://doi.org/10.1016/j.ymssp.2011.12.008

[13] D. Paul and K. Roy, "Application of bridge weigh-in-motion system in bridge health monitoring: a state-of-the-art review," *Structural Health Monitoring*, Art. no. 147592172311544, Mar. 2023, doi: https://doi.org/10.1177/14759217231154431

[14] A. Žnidarič and J. Kalin, "Using bridge weigh-in-motion systems to monitor single-span bridge influence lines," *Journal of Civil Structural Health Monitoring*, vol. 10, no. 5, pp. 743–756, Jul. 2020, doi: https://doi.org/10.1007/s13349-020-00407-2

[15] F. Moses, "Weigh-in-Motion System Using Instrumented Bridges," *Transportation Engineering Journal of ASCE*, vol. 105, no. 3, pp. 233–249, May 1979, doi: https://doi.org/10.1061/tpejan.0000783.

[16] S. S. Law, T. H. T. Chan, and Q. H. Zeng, "Moving Force Identification: A Time Domain Method," *Journal of Sound and Vibration*, vol. 201, no. 1, pp. 1–22, Mar. 1997, doi: https://doi.org/10.1006/jsvi.1996.0774

[17] T. H. T. Chan, S. S. Law, T. H. Yung, and X. R. Yuan, "An interpretive method for moving force identification," *Journal of Sound and Vibration*, vol. 219, no. 3, pp. 503–524, Jan. 1999, doi: https://doi.org/10.1006/jsvi.1998.1904

[18] S. S. Law, Tommy H.T. Chan, and Q. L. Zeng, "Moving Force Identification—A Frequency and Time Domains Analysis," *Journal of Dynamic Systems Measurement and Control-transactions of The Asme*, vol. 121, no. 3, pp. 394–401, Sep. 1999, doi: https://doi.org/10.1115/1.2802487

[19] WAVE Project Consortium, *Weigh-in-Motion of Axles and Vehicles for Europe: Final Report*, RTD Project RO-96-SC-403. European Commission, Brussels, Belgium, 2002.

[20] Y. Yu, C. S. Cai, and L. Deng, "Nothing-on-road bridge weigh-in-motion considering the

transverse position of the vehicle," *Structure and Infrastructure Engineering*, vol. 14, no. 8, pp. 1108–1122, Nov. 2017, doi: https://doi.org/10.1080/15732479.2017.1401095.

[21] A Žnidarič, I Lavrič, and J. Kalin, "Latest practical developments in the bridge WIM technology," in *Bridge maintenance, safety and management*, Jul. 2010, pp. 993–1000, [Online]. Available: doi: https://www.researchgate.net/publication/281551030_Latest_practical_developments_in_the_bridge_WIM_technology

[22] J. Kalin, A. Žnidarič, and I. Lavrič, *Practical Implementation of Nothing-on-the-Road Bridge Weigh-in-Motion System*. Ljubljana, Slovenia: Slovenian National Building and Civil Engineering Institute (ZAG), 2006.

[23] M. Marín, D. Millán Yusti, S. Castellanos Toro, J. Marulanda Casas, and P. Thomson, "Caracterización de cargas vehiculares en un puente con monitoreo estructural," in *Desarrollo e Innovación en Ingeniería*. Colombia, Antioquía: Instituto Antioqueño de Investigación, 2021, pp. 627–640. [Online]. Available: https://dialnet.unirioja.es/servlet/articulo?codigo=8742742

[24] E. MacLeod and K. Arjomandi, "Enhanced Bridge Weigh-in-Motion System Using Hybrid Strain–Acceleration Sensor Data," *Journal of Bridge Engineering*, vol. 27, no. 9, Jul. 2022, doi: https://doi.org/10.1061/(asce)be.1943-5592.0001924

[25] E. J. OBrien, M. J. Quilligan, and R. Karoumi, "Calculating an influence line from direct measurements," *Proceedings of the Institution of Civil Engineers - Bridge Engineering*, vol. 159, no. 1, pp. 31–34, Mar. 2006, doi: https://doi.org/10.1680/bren.2006.159.1.31

[26] D. Millán, "Metodología para la gestión de la integridad estructural de una red urbana de puentes con actualización en tiempo real," *Doctoral Thesis*, Universidad del Valle, Cali, Colombia, 2023.

# Sustainable Materials for Acoustic Barriers in Urban Infrastructure: A Systematic Review

Elena Tirado Duarez[1], Henrry Delgado Ortega[2]

[1] 20232929@aloe.ulima.edu.pe, [2] HSDELGAD@ulima.edu.pe

[12] Facultad de Ingeniería, Universidad de Lima, Perú.

Recibido: 21 Mayo 2025 / Publicado: 24 Abril 2026
https://doi.org/10.26439/ciic2025.8667

ABSTRACT: **Noise pollution is a major environmental and public health issue in urban areas, leading to the extensive use of acoustic barriers in transportation and infrastructure projects. Traditionally, these barriers have relied on synthetic materials with high acoustic efficiency but considerable environmental impact. This study presents a systematic review of 65 scientific publications published between 2015 and 2024, examining the acoustic performance, environmental impact, durability, and technical feasibility of materials used in acoustic barriers. The review compares conventional synthetic materials with natural, recycled, and hybrid alternatives, using indicators such as noise attenuation metrics, sound absorption coefficients, and life cycle assessment results. The findings show that natural and recycled materials can achieve competitive acoustic performance in specific frequency ranges and application contexts, particularly in urban and moderate-noise environments, while offering clear sustainability advantages. However, limitations persist in low-frequency attenuation, long-term durability, and large-scale implementation under real operating conditions. Hybrid materials emerge as a promising compromise between acoustic efficiency and environmental performance, although cost and technological barriers currently restrict widespread adoption. The study underscores the need for long-term field validation, standardized evaluation methods, and cost-effective production processes to support the integration of sustainable acoustic barriers in urban infrastructure.**

KEYWORDS: sustainable acoustic barriers, sound absorption, recycled materials, environmental impact, comparative analysis, civil engineering

## I. Introduction

Noise pollution has become an increasingly complex environmental problem in urban and industrial settings and is considered by the World Health Organization (WHO) to be the second most significant environmental risk to human health, affecting more than 30 % of the global population [1]. This phenomenon, primarily driven by vehicular traffic and industrial activity, has direct consequences for public health, including an increased incidence of cardiovascular diseases, sleep disturbances, and cognitive deficits [2]. Despite the recognized importance of addressing noise pollution, effective mitigation remains a challenge, particularly in areas with elevated noise levels that require sustainable and technically effective solutions.

Acoustic barriers—structures designed to minimize noise propagation—are among the most widely used strategies for controlling environmental noise. Traditionally manufactured from materials such as concrete, metal, and polycarbonate, these barriers exhibit significant limitations associated with their environmental

impact during production and their reduced effectiveness in low- and mid-frequency ranges, particularly in dense urban environments [3], [4]). In response to these limitations, the scientific community has increasingly focused on the development of alternative materials capable of providing comparable or superior acoustic performance while reducing without the environmental impacts associated with conventional materials.

Over the past decade, alternative materials such as coconut fiber, straw, and various recycled composites have emerged as promising options, demonstrating not only favorable acoustic properties but also a reduced environmental footprint. For example, [5] and [6] reported that hybrid composites and natural fibers can achieve high noise reduction coefficients (NRC values of up to 0.8) along with effective sound attenuation performance. Similarly, other recycled materials, such as straw-cement composites, have shown reduced environmental impact together with satisfactory noise attenuation performance [7], [8]). However, much of the existing literature has focused on isolated material evaluations conducted under controlled laboratory conditions, leaving important questions unanswered regarding the real-world performance of these materials in urban infrastructure contexts, their long-term durability, and their practical applicability.

Despite these advances, significant gaps remain in the literature in terms of direct comparisons of acoustic and environmental performance of different material types (natural, recycled, synthetic, and hybrid). To date, no systematic review has integrated the methodologies used to evaluate the acoustic efficiency, sustainability, and durability of noise barriers in real-world urban scenarios. The diversity and heterogeneity of previous studies make it difficult to establish reliable technical standards to guide material selection in sustainable infrastructure projects [9], [10].

This study is grounded in the premise that, although natural and recycled materials often exhibit lower performance at low frequencies when compared with advanced synthetic materials, they offer substantial advantages in terms of sustainability, cost, and long-term feasibility. The main objective of this study is to conduct a systematic review comparing the acoustic and environmental performance of materials used in noise barriers, addressing existing gaps through the analysis of key methodologies for assessing acoustic efficiency (NRC and noise reduction), environmental impact (LCA), structural durability, and technical evaluation criteria.

Finally, this research proposes an analytical regulatory and environmental framework that may guide informed material selection, contributing to the development of more sustainable urban infrastructure that is effective in noise mitigation.

## II. Methodology

This study employs a systematic review of the literature on sustainable acoustic barriers, focusing on peer-reviewed publications in English and Spanish retrieved from databases such as Scopus, Web of Science, and Google Scholar. The search included key terms such as “acoustic wall,” “sustainable sound insulation,” “absorbing material,” “natural fiber for sound insulation,” and “recyclable acoustic panel,” and was limited to studies published between 2015 and 2024, a period reflecting the growing interest in architectural solutions that integrate sustainability, acoustic performance, and structural feasibility.

The selection criteria included experimental studies, case studies, and reviews that analyzing natural, recycled, hybrid, and synthetic materials used in acoustic barriers, with evaluations of parameters such as sound absorption (NRC), sound level reduction (dB), sustainability assessed through life cycle analysis (LCA), and material or structural durability. Excluded from consideration were documents not specifically addressing acoustic barriers, those focused solely on regulation or design without quantitative analysis, studies based exclusively on simulations without experimental validation, publications in other languages other than English or Spanish, and works those without full-text access.

From an initial total of 896 identified records, 245 were removed due to duplication. Of the remaining 651 records, 142 articles were selected for title and abstract screening and subsequent full-text assessment, resulting in the inclusion

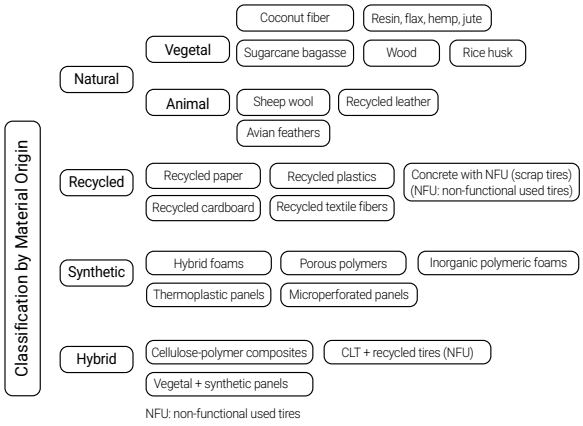


Fig. 1: Classification of materials used in acoustic barriers according to their origin: natural (plant- and animal-based), recycled, synthetic, and hybrid. Specific examples for each category are shown.

of 65 studies in the systematic review and the exclusion of 77 that did not meet the established criteria. The selected studies were organized according to material type (natural, recycled, synthetic, hybrid), evaluation method (laboratory tests, field trials and simulation-supported analyses), analyzed acoustic variables (NRC and sound level reduction in dB), and environmental and technical impacts in urban settings.

## III. Results

### *A. Materials used in acoustic barriers*

Various materials used in noise barriers were identified and analyzed in terms of their noise reduction performance, application context, and ecological impact.

In the reviewed literature, the information is organized according to the origin of the materials, distinguishing among natural fibers, recycled materials, synthetic products, and hybrid composites, which allows a systematic comparison of their acoustic and environmental behavior. In particular, the studies emphasize the acoustic performance of plant- and animal-based fibers, carbon- and polymer-based materials, and composite solutions combining organic and recycled components.

To ensure comparability among the different investigations, the analysis considers common acoustic parameters reported in the literature, mainly the sound absorption coefficient and the Noise Reduction Coefficient (NRC), evaluated over standardized frequency bands typically ranging from 125 Hz to 4000 Hz, which are representative of traffic and urban noise spectra. When available, sound levels are interpreted using equivalent continuous sound pressure levels expressed in dB(A), which account for the human auditory response. For the purpose of interpretation, low acoustic performance is associated with NRC values below 0.30, medium performance between 0.30 and 0.60, and high performance above 0.60, providing a reference scale for comparing materials reported in different studies.

Historically, the most widely used materials for sound absorption include glass wool, mineral wool, and synthetic polymers [11]. However, these materials present significant environmental limitations, as they are not biodegradable and generate pollution at the end of their life cycle [12]. In addition, energy-intensive manufacturing processes contribute to a high carbon footprint [7], and the use of certain toxic compounds in their production has been banned in some countries [13]. Accordingly, while synthetic materials continue to predominate due to their high acoustic efficiency, an increasing number of studies report the use of natural and recycled materials. Figure 1 presents the classification of acoustic barriers according to the material type considered in the reviewed studies.

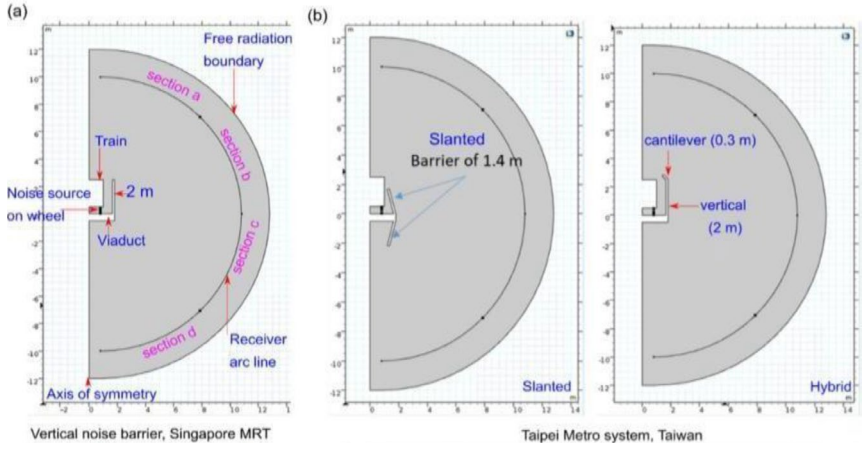


Fig. 2. Conventional aluminum noise barrier (elevated railway application) [3].

Acoustic barriers are engineering structures installed along transportation infrastructures such as highways and railways to mitigate the propagation of traffic noise toward surrounding urban areas. Their performance depends not only on the acoustic properties of the materials used, but also on geometric factors such as height, location, and surrounding morphology. Conventional barriers are commonly manufactured using metals, concrete, polymers, or composite panels, which offer effective noise attenuation but may present environmental and spatial limitations in dense urban contexts.

The practical implementation of acoustic barriers in complex urban geometries presents significant design challenges. Figure 2 illustrates a typical application of an aluminum barrier on an elevated railway line, this configuration provides a measurable reduction of 5–12 dB.

However, due to height limits (2.2–5.1 m), its effectiveness decreases near high-rise buildings, reducing its performance in densely populated urban areas or close to tall structures, with negative impacts [3]. These systems are effective for noise attenuation, but since they must adapt to local topography and spatial limitations, there are challenges to their application in certain environments, which calls for consideration of alternative solutions.

Fig. 3. Coconut fiber in wooden wall [14].

Within the reviewed studies, natural materials emerge as viable alternatives for acoustic barriers, as they combine effective noise attenuation with reduced environmental impact. Among these materials, coconut fiber stands out as a particularly promising option. As shown in Figure 3, coconut fiber-based materials have been applied to enhance acoustic performance in contexts where both sustainability and noise mitigation are key considerations [14]. These materials have demonstrated particular effectiveness in absorbing low- and mid-frequency sound, making them suitable for applications where reduction of railway traffic noise is critical. Moreover, as a renewable resource, coconut fiber reinforces its potential as an environmentally favorable alternative to conventional synthetic materials.

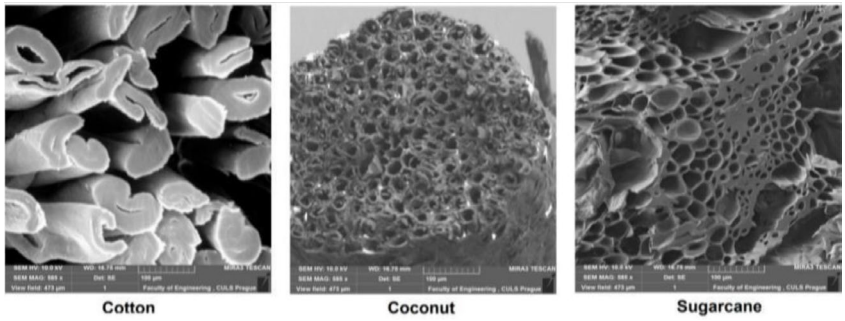


Fig. 4. Shows the microscopic details of cotton, coconut, and sugarcane fibers [12].

The use of coconut fiber has been associated not only with enhanced acoustic performance but also with improved economic and sustainability indicators. Several studies report that coconut fiber, particularly when combined with other natural materials, enhances the effectiveness of sound barriers, resulting in greater noise attenuation compared to conventional synthetic solutions. For instance, laboratory tests have demonstrated that acoustic barrier walls incorporation coconut fibers achieve higher levels of noise reduction than commonly used synthetic products such as polyurethane and polyethylene panels [12].

Coconut fibers can be effectively combined with other materials to form composite acoustic panels with improved performance, as shown in Figure 4 [12]. These composite panels, which incorporate natural fiber waste such as cotton, coconut, and sugarcane, are reinforced with epoxy resin to enhance acoustic performance. The sound absorption coefficient increases with the fiber content, with coconut fiber exhibiting the highest absorption values among the materials analyzed. At 1600 Hz, the absorption coefficient ranges from 0.081 to 0.183, depending on the type and content of fibers used.

In contrast to natural fibers, carbon fibers demonstrate excellent thermal stability, withstanding temperatures of up to 300 °C. Although their sound absorption capacity is moderate, carbon fibers provide strong noise-damping performance, making them more suitable for use as acoustic barriers than as sound-absorbing materials. Experimental tests indicate that composite materials incorporating carbon fibers achieve higher levels of noise reduction than conventional synthetic products. By comparison, earth and concrete barriers used on Spanish highways typically achieve attenuation levels ranging from 6.53 to 7.79 dB(A). However, continuous maintenance is required to prevent performance degradation over time [4]. Nevertheless, despite the continued dominance of synthetic materials due to their high acoustic efficiency, their environmental limitations have contributed to the growing interest in natural and recycled alternatives.

As shown in Figure 5, panels made from recycled materials such as straw-cement composites, also demonstrate high acoustic efficiency. These materials not only meet established acoustic performance requirements but also contribute to sustainability by reducing the demand for virgin natural resources. Rice husk composite (RHC) achieves a noise reduction index of 5–6 dB, while the treated wood composite (TWC) reaches values of 8–9 dB and performs effectively within the target frequency range (315–3150 Hz). In particular, rice husk-based materials have been used to manufacture acoustic panels with strong performance at the tested frequencies, exhibiting noise attenuation levels comparable to conventional materials such as concrete or metal [8].

In addition, studies such as Amarilla et al. (2021) report that construction and demolition waste (CDW) blocks achieve noise reductions of 11–14 dB, demonstrating that recycled materials

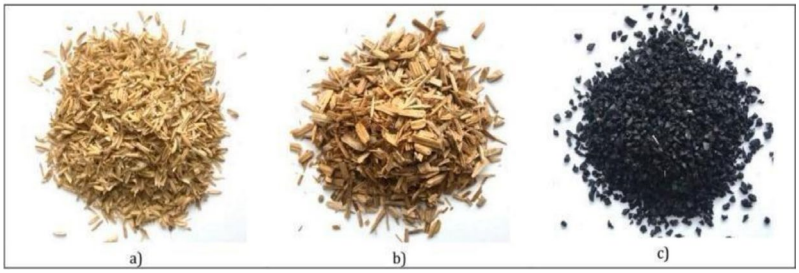


Fig. 5. Shows the materials used in the composites. (a) Rice husk. (b) Treated wood. (c) Recycled rubber [8].

can be competitive in urban environments. By comparison, as shown in Figure 6, displays finished composite panels incorporating cotton, coconut, and sugarcane fibers, illustrating the scalable product form that can be deployed in construction, this panels fiber exhibit high sound absorption, largely due to their porous structure and their ability to dissipate sound waves. As a result, these materials have been implemented in various urban applications, including the protection of residential areas adjacent to high-traffic roads. For example, [12] report that coconut fiber reinforced with epoxy resin achieves absorption coefficients of 0.183 at mid frequencies (1600 Hz). In addition, as illustrated in Figure 7, crucially, shows the standardized laboratory samples made from similar natural fiber composites, [10] show that composites incorporating natural fibers such as ramie and flax outperform synthetics materials at high frequencies, with absorption coefficients exceeding 0.6 above 800 Hz.

Hybrid materials combining natural and synthetic fibers have also demonstrated promising performance in the reviewed studies. These materials offer a balanced combination of properties that enhance both acoustic efficiency and sustainability. Combinations of materials such as cotton, sugarcane, and coconut have been shown to improve acoustic performance while providing a more environmentally favorable alternative to traditional synthetic panels.

By contrast, synthetic panels remain relevant due to their durability and sound absorption efficiency. These materials offer advantages such as resistance to extreme environmental conditions and high performance at low frequencies;

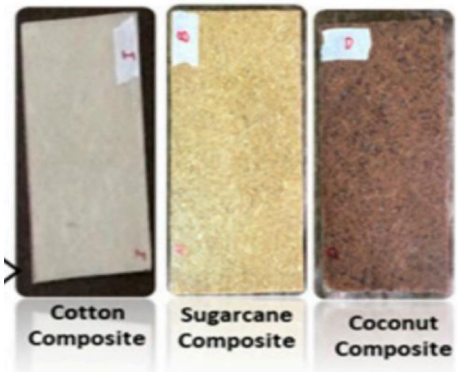


Fig. 6. Composite panels with cotton, sugarcane, and coconut [12].

however, their ecological footprints and production costs are often higher than those of natural and recycled alternatives. Nevertheless, their versatility and reliable performance across a wide range of conditions make them particularly suitable for projects in which long-term durability and consistent acoustic efficiency are essential.

### *B. Acoustic Performance and Sustainability in Noise Barriers*

Natural materials such as wool and coconut fibers have shown favorable results in terms of noise reduction, particularly within mid- and high-frequency ranges. These materials are primarily applied in urban infrastructure and in acoustic panels for transportation and construction projects, where acoustic efficiency is a critical requirement. Their overall acoustic performance

Fig. 7. Acoustic samples of composites with natural fibers [10].

is generally high (NRC coefficient of 0.7 to 0.8), however, their effectiveness tends to decrease at low frequencies, where sound attenuation remains a challenge. Coconut fiber, in particular, has a low carbon footprint and is a renewable resource, making it suitable for sustainable projects; however, limitations related to durability and acoustic effectiveness at low frequencies have been reported. These trends are illustrated in Figure 8.

By contrast, recycled materials such as straw-cement composites and recycled tire-based systems exhibit high sound absorption performance, with reported NRC values exceeding 0.9 in some cases. These materials have been applied primarily in highways and industrial sites in countries such as India, Colombia, and Spain, where high noise exposure and material availability favor their use. The use of recycled materials not only reduces the demand for virgin natural resources but also contributes to circular economy principles. However, while their sound absorption performance is competitive, these materials may require additional processing to ensure long-term durability and resistance to extreme weather conditions.

Synthetic materials such as 3D-printed foams and hybrid foams have demonstrated high acoustic efficiency across a wide frequency range, as demonstrated in applications for road infrastructure or elevated railway lines. These materials exhibit very high sound absorption performance, with NRC values of up to 0.99; however, their high environmental impact and elevated production costs represent significant drawbacks. They are therefore suitable for scenarios requiring precise acoustic performance and enhanced durability, such as industrial environments or high-traffic

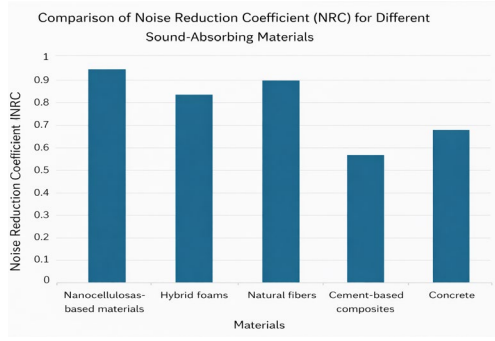


Fig. 8. Sound absorption coefficient of acoustic barriers.

areas; nevertheless, they are not the most ecological or cost-effective options.

Finally, hybrid materials combining natural and synthetic fibers are emerging as a viable option, with reported NRC values of up to 0.94 in certain applications. These materials integrate the high acoustic efficiency characteristic of synthetic materials with the improved sustainability associated with natural fibers. However, higher costs and the complexity of their manufacturing processes may limit their widespread adoption.

Figure 9 indicates that Inorganic Polymeric Foams (IPF) exhibit the highest acoustic performance among the materials analyzed, achieving approximately 100 dB, significantly outperforming other material categories. This exceptional sound attenuation makes them particularly suitable for applications in areas with high noise exposure, such as industrial zones, high-traffic roads, and airport runways, where effective noise control is critical.

Fiber composite materials also demonstrate high levels of noise attenuation, around 80 dB, making them suitable for use in urban infrastructure and industrial environments. These materials are particularly suitable for applications in which sound absorption plays a key role in improving acoustic quality, such as in commercial buildings or residential areas located near major highways.

Hybrid foams provide intermediate levels of acoustic performance, approximately 2 dB, positioning them between high-performance synthetic materials and natural or recycled alternatives. Although they do not reach the performance levels of high-end synthetic materials, they represent a viable alternative for projects that seek to balance sustainability and acoustic performance, such as green infrastructure or urban development initiatives.

Finally, microperforated panels (~14 dB) and earth berms (~10 dB) exhibit moderate levels of noise attenuation. These materials are suitable for agricultural projects or areas with lower traffic intensity, where overall noise levels are relatively low. Despite their limited noise attenuation capacity, they represent a cost-effective and easily deployable option in areas with less demanding acoustic control requirements.

## *C. Noise Reduction of Acoustic Barriers*

Table 1 compares different types of acoustic barriers used in various parts of the world, detailing the materials employed, reported noise mitigation performance (expressed in decibels), and the types of infrastructure in which they have been applied.

Figure 10 indicates that acoustic barriers based on construction and demolition waste (CDW) are among the most expensive options reported, with costs reaching up to USD 1,150 per unit, depending on the configuraton [2]. This type of barrier is primarily used in urban road infrastructure environments, where structural and regulatory requirements are particularly tringent. Despite being based on recycled material, its relatively high cost can be attributed to the additional processing, pressing, and technical adaptation steps required to meet structural and regulatory standards.

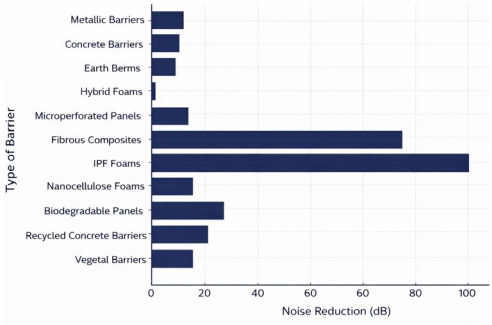


Fig. 9. Efficiency of different types of acoustic barriers.

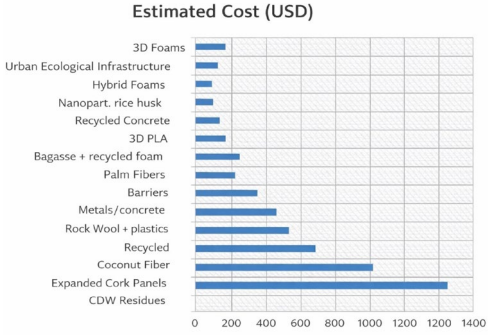


Fig. 10. Comparison of materials based on the investment required for acoustic barriers..

At first glance, it may appear counterintuitive that a waste-based material is among the most expensive options. However, the cost depends not only on the origin of the raw input but also on the conversion processes required to meet structural and acoustic performance requirements. First, CDW must be carefully classified and separated, as not all waste fractions are suitable for reuse. These materials must then undergo technical processes such as crushing, stabilization, or agglomeration with resins in order to form structurally sound and durable volumes or panels. In addition, their application requires laboratory testing to verify both their sound insulation capacity and structural performance, implying additional investment in certification and quality assessment procedures.

TABLE I

Comparison of Issues Among Studies

| Author | Material | Noise Reduction (dB) | Infrastructure and Place of Application | Cost Estimation |
|---|---|---|---|---|
| Yang y Li (2012) | Palm fibers | 7.00-8.02 | Acoustic panels for transportation and construction interiors. Malaysia | Natural fibers are more economical and offer ecological advantages |
| Rendón et al. (2022) | Metal and concrete barriers, and earth berms | 6.53-7.79 | Road infrastructure (highways). Spain | USD 50–150 per square meter |
| Rendón et al. (2022) | Rice husk nanoparticles | 0.94 | Urban façades (concrete, resin, mortar, etc.). Colombia | USD 20–60 per square meter |
| Rastogi et al. (2024) | 3D-printed foams | 6.30 | Architecture and transportation applications. United Kingdom | USD 108.64 per sample |
| Amarilla et al. (2021) | Construction and demolition waste (CDW) | 11-14 | Urban roadside barriers | Total cost: USD 50–100 |
| Villa et al. (2019) | Coconut fiber | 0.50-0.13 | Wooden walls for buildings. Colombia | USD 100–300 per cubic meter |
| Zhang et al. (2024) | Urban ecological infrastructure | 10.00 | Urban ecological infrastructure (UEI) | Low cost (eco-friendly, recyclable) |
| Liao et al. (2023) | Hybrid foams | 0.99 | Potential for building envelopes. Quzhou, China | Low cost (eco-friendly, recyclable) |
| Sailesh et al. (2021) | 3D-printed biodegradable PLA | >10.00 | Test panels evaluated using an impedance tube. India | USD 25–75 per panel (estimated based on PLA prices and 3D-printing costs) |
| Sharma et al. (2023) | Expanded cork panels | >30.00 | Sustainable buildings, interior walls. Portugal | USD 150–350 per $m^3$ (expanded cork estimate) |

Moreover, the weight and geometry of these materials require complex logistical arrangements during transport and installation, which further increase their relative cost. Furthermore, many CDW-based solutions remain at the experimental or pilot-project stage, meaning that their production is not yet fully standardized or implemented at an industrial scale. This lack of standardization contributes to higher costs, a pattern commonly observed in emerging construction technologies.

Other materials also exhibit relatively high costs, including expanded cork panels used in sustainable buildings in Portugal, aluminum applied in railway systems in Singapore, and coconut-based components. All of these solutions exceed USD 250 per unit of measurement, depending on configuration and application, reflecting a trend toward technically robust but more specialized solutions.

By contrast, cheaper and more environmentally friendly alternatives, such as palm fiber, rice husk nanoparticles, or biodegradable polymers like polylactic acid (PLA), have generally been tested only on a limited basis. This is partly because these materials tend to exhibit lower structural resistance to adverse conditions such as weather exposure or vandalism, which limits their suitability for use in public spaces. In addition, there is a degree of uncertainty and limited technical familiarity among designers and regulatory authorities regarding their long-term performance.


Fig. 11. Sample of super-stable foams reinforced with Cellulose Nanofibers (CNF) [9].

Finally, countries in which more expensive acoustic barrier materials are reported—such as Spain, Portugal, Singapore, or Brazil—tend to operate within regulatory frameworks characterized by stricter technical requirements and higher investment capacity. These conditions support prioritization criteria related to durability, structural performance, and technical standardization, which helps explain the preference for higher-cost acoustic barrier solutions.

*D. Criteria for the Implementation of Acoustic Barriers*

Recent advances in the design of acoustic barriers reflect the need to balance technical efficiency, sustainability, and economic feasibility, as summarized in Table 2. In the context of noise mitigation, studies such as [15] report that periodic structures incorporated into Helmholtz resonant cavities can achieve noise attenuation of up to 16 dB at specific frequency ranges (400–890 Hz). However, their effectiveness depends on factors such as barrier height and spatial configuration, and their action is limited to partial noise attenuation rather than complete noise elimination, as summarized in Table 2. With respect to materials [9], as illustrated in Figure 11, show that nanocellulose-based composites and hydrophobic particle systems can achieve high sound absorption when used in hybrid foam configurations, while maintaining a relatively low environmental impact. By contrast, conventional synthetic materials continue to generate waste streams that are difficult to recycle.

This observation is consistent with the advantages of recycled variants, such as end-of-life tire (ELT)-based systems, listed in Table 2, despite their shorter lifespan. In terms of costs, Table 2 indicates that innovative designs, such as the system developed by [16], require substantial initial investment; however, optimized maintenance strategies —such as the use of digital filters based on Gauss–Legendre quadrature—can significantly reduce operating costs. Finally, design flexibility enables the integration of micro-perforated panels or vegetation-based systems [15]); however, their implementation in dense urban environments remains a challenging, as indicated in Table 2. Taken together, these findings emphasize the need to adapt acoustic solutions to specific contextual conditions and to prioritize sustainable materials and multifunctional structural designs.

## IV. Discussion of Results

This study provides an integrative overview of materials used in acoustic barriers, with particular emphasis on acoustic performance, durability, and structural resistance. The results are consistent with previous findings supporting the effectiveness of natural and recycled materials in enhancing acoustic performance, in line with [8], who report favorable results for rice husk cement, while noting that its performance depends on structural configuration. However, despite their potential, these materials exhibit limitations in

TABLE II

Comparative Table of Advantages and Disadvantages of Acoustic Barriers

| Category | Advantages | Disadvantages |
|---|---|---|
| Noise reduction | -They mitigate noise impact in urban and industrial areas.<br>-They improve quality of life by reducing noise pollution.<br>-They enable compliance with environmental regulations on noise levels. | - Effectiveness depends on the material, height, and location.<br>-They do not completely eliminate noise; they only attenuate it.<br>-Some barriers may cause sound reflection instead of absorption. |
| Materials used | -Wide range of options: natural, recycled, synthetic, and hybrid materials.<br>-Biodegradable and recycled materials reduce environmental impact.<br>-Advanced polymers and hybrid foams provide high acoustic absorption. | -Synthetic materials have a high environmental impact.<br>-Some recycled materials exhibit lower durability.<br>-Natural materials may degrade over time if not properly treated. |
| Costs and economic feasibility | -Low-cost options exist, such as earth berms and recycled-material barriers.<br>-Different materials can be combined to optimize cost and efficiency.<br>-Long-term cost reduction through the use of sustainable materials. | -The initial investment can be high for advanced barriers and innovative designs.<br>-Some barriers require constant maintenance, increasing operational costs.<br>-Advanced materials can have high production costs. |
| Durability and maintenance | -Materials such as concrete and polymers offer high mechanical resistance.<br>-Some recycled barriers, such as those made from ELT (end-of-life tires), show good mechanical stability.<br>-Hybrid designs combine structural resistance with acoustic absorption. | -Metal barriers require frequent maintenance to prevent<br>-Barriers made from biodegradable materials may deteriorate due to moisture.<br>-Some structures may lose efficiency over time. |
| Environmental impact | -Natural and recycled material barriers reduce the carbon footprint.<br>-Innovative designs optimize material use without compromising sustainability.<br>-The use of recycled materials promotes the circular economy and reduces waste. | -Synthetic materials such as plastics and polymers generate waste that is difficult to recycle.<br>-The production of concrete and metals has high $CO_2$ emissions.<br>-Some recycled solutions require additional processes that may generate secondary pollution. |
| Design flexibility | -They can be designed with different heights, inclinations, and shapes to optimize performance.<br>-They can be integrated with vegetation to improve aesthetics and acoustic absorption.<br>-Portable and adaptable solutions can be developed for different environments. | -Some barriers require large areas to be effective.<br>-Implementation in densely urbanized areas can be challenging.<br>-Certain configurations may alter the urban landscape. |

low frequency noise attenuation, which is critical for industrial applications and high-traffic environments. This observation is consistent with the findings of [15], who report similar low-frequency constraints in periodic structural systems.

A key gap identified in the literature is that many studies, including those reviewed here, focus on controlled laboratory conditions without validation under real-world or long-term operational conditions. As noted by [9], hybrid materials—despite their low environmental impact—lack comprehensive studies based on real-world applications, representing a methodological limitation that hinders their broader practical adoption. This

lack of data on durability and real-world behavior under extreme environmental conditions introduces uncertainty and limits the robustness of current knowledge.

The analysis also reveals a gap between the technical potential of hybrid materials and their commercial feasibility. High production costs and technological barriers, as emphasized by [17], represent significant obstacles to large-scale adoption, thereby limiting the contribution of these materials to urban noise mitigation and the broader promotion of sustainable infrastructure.

Therefore, enhancing environmental performance and reducing costs are critical challenges that must be addressed for natural, recycled, and hybrid materials to become viable alternatives to traditional synthetic solutions, thereby contributing to a lower ecological footprint and improved urban quality of life [12], [10]. In particular, there is a need to develop technologies and production processes that enhance the structural performance of these materials under real-world conditions while reducing costs, in order to facilitate their integration into urban acoustic infrastructures that must meet stringent technical, environmental, and economic standards.

By contrast, variations in acoustic performance are observed in certain recycled materials, such as recycled cardboard, which—despite achieving limited noise reduction (approximately 7–8 dB)—do not reach the performance levels required for high-noise environments. This reduced effectiveness is likely related to insufficient structural rigidity and limited performance at low frequencies, which are critical in industrial applications. This observation highlights the need for further analysis of material structure and specific physical properties in order to optimize acoustic performance across in different application contexts.

Finally, this study contributes to existing knowledge by integrating acoustic, environmental, and durability analyses, and suggests that hybrid materials combining natural and synthetic fibers represent a viable pathway for optimizing acoustic efficiency without compromising durability. However, the adoption of emerging innovations such as nanotechnology and additive manufacturing (3D printing) still requires overcoming significant economic and technical challenges in order to achieve a substantial impact on urban infrastructure [17].

In summary, the discussion indicates that although progress in sustainable acoustic materials has been significant, important methodological and technological gaps remain, along with limitations related to environmental performance and cost. Future research should therefore focus on long-term testing, field validation, and economic and technical optimization to enable efficient and sustainable practical application.

## V. Conclusion

The analysis conducted in this study on acoustic barriers demonstrates that it is essential to select materials considering not only their acoustic efficiency, but also their environmental impact and economic feasibility, in accordance with the established objectives. Natural materials, such as coconut fiber and sheep wool, as well as recycled materials, such as rice husk cement and recycled plastics, were identified, achieving significant noise reductions ranging from 5 to 14 dB [2],[2], [8] and NRC coefficients between 0.13 and 0.94 [12], [10], confirming their potential as sustainable alternatives.

The initial hypothesis that these materials could match or surpass synthetic materials in acoustic efficiency and durability is partially confirmed. Although competitive, they face significant challenges related to durability and resistance to adverse environmental factors, which limit their practical and large-scale application [1], [4].

The systematic review method applied was validated for integrating acoustic, environmental, and economic aspects, allowing the identification of significant gaps in the literature, particularly the lack of long-term evaluations under real-world conditions, which reduces the robustness of the available knowledge and confidence in its practical application.

Furthermore, synthetic materials such as hybrid foams and advanced polymers, with NRC coefficients close to 0.99 [5], exhibit high acoustic performance; however, their high cost and environmental footprint position them as less

sustainable options. Hybrid materials combine properties from both approaches, achieving an NRC coefficient of approximately 0.94, but require optimization of production processes to reduce costs and facilitate their adoption [17].

The identified limitations, such as the lack of real-world testing, insufficient durability, and economic barriers, highlight the need for future research focused on field validation, technology optimization, and cost reduction, as well as on the development of materials with improved low-frequency performance and greater environmental resistance.

Finally, this research reaffirms the importance of continuing to develop sustainable acoustic solutions through a multidisciplinary approach that includes materials science, environmental engineering, and circular economy principles. The integration of natural and recycled materials into acoustic barriers not only improves acoustic efficiency but also significantly contributes to the sustainability of urban infrastructure and is essential for the future of cities.

## References


[1] A. Barros, J. K. Kampen, and C. Vuye, "Noise barriers as a mitigation measure for highway traffic noise: Empirical evidence from three study cases," *J. Environ. ManageJ. Environ. Manage.*, vol. 367, Art. no. 121963, 2024, https://doi.org/10.1016/j.jenvman.2024.121963

[2] R. S. D. Amarilla, R. Scoczynski, M. H. De Avelar, R. Pereira, L. H. Sant'Ana, and R. E. Catai, "Acoustic barrier simulation of construction and demolition waste: A sustainable approach to the control of environmental noise," *Appl. Acoust.*, vol. 182, Art. no. 108201, 2021, https://doi.org/10.1016/j.apacoust.2021.108201

[3] H. Pueh, K. Meng, and S. Kumar, "Noise assessment of elevated rapid transit railway lines and acoustic performance comparison of different noise barriers for mitigation of elevated railway tracks noise," *Appl. Acoust.*, vol. 183, Art. no. 108340, 2021, https://doi.org/10.1016/j.apacoust.2021.108340

[4] J. M. Martinez-Orozco and A. Barba, "Determination of Insertion Loss of noise barriers in Spanish roads," *Appl. Acoust.*, vol. 186, Art. no. 108435, 2021, https://doi.org/10.1016/j.apacoust.2021.108435

[5] J. Liao, Y. Hou, J. Li, M. Zhang, Y. Dong, and X. Chen, "Lightweight and recyclable hybrid multifunctional foam based cellulose fibers with excellent flame retardant, thermal, and acoustic insulation property," *Compos. Sci. Technol.*, vol. 244, Art. no. 110315, 2023, https://doi.org/10.1016/j.compscitech.2023.110315

[6] S. Sharma, P. Sudhakara, J. Singh, S. Singh, and G. Singh, "Emerging progressive developments in the fibrous composites for acoustic applications," *J. Manuf. Process.*, vol. 102, pp. 443–477, 2023, https://doi.org/10.1016/j.jmapro.2023.07.053

[7] C. Buratti, E. Belloni, E. Lascaro, G. A. Lopez, and P. Ricciardi, "Sustainable Panels with Recycled Materials for Building Applications: Environmental and Acoustic Characterization," *Energy Procedia*, vol. 101, pp. 972–979, 2016, https://doi.org/10.1016/j.egypro.2016.11.123

[8] B. Marques, J. Almeida, A. Tadeu, J. António, M. I. Santos, J. De Brito, and M. Oliveira, "Rice husk cement-based composites for acoustic barriers and thermal insulating layers," *J. Build. Eng.*, vol. 39, Art. no. 102297, 2021, https://doi.org/10.1016/j.jobe.2021.102297.

[9] R. Abidnejad, M. Beaumont, B. L. Tardy, B. D. Mattos, and O. J. Rojas, "Superstable Wet Foams and Lightweight Solid Composites from Nanocellulose and Hydrophobic Particles," *ACS Nano*, vol. 15, no. 12, pp. 19712–19721, 2021, https://doi.org/10.1021/acsnano.1c07084.

[10] W. Yang and Y. Li, "Sound absorption performance of natural fibers and their composites," Sci. China Technol. Sci., vol. 55, pp. 2278–2283, 2012, https://doi.org/10.1007/s11431-012-4943-1.

[11] N. M. Aly, H. S. Seddeq, K. Elnagar, and T. Hamouda, "Acoustic and thermal performance of sustainable fiber reinforced thermoplastic composite panels for insulation in buildings," J. Build. Eng., vol. 40, art. no. 102747, 2021, https://doi.org/10.1016/j.jobe.2021.102747.

[12] T. Hassan et al., "Acoustic, Mechanical and Thermal Properties of Green Composites Reinforced with Natural Fibers Waste," Polymers, vol. 12, no. 3, art. no. 654, 2020, https://doi.org/10.3390/polym12030654.

[13] F. Asdrubali, F. D'Alessandro, and S. Schiavoni, "A review of unconventional sustainable building insulation materials," Sustain. Mater. Technol., vol. 4, pp. 1–17, 2015, https://doi.org/10.1016/j.susmat.2015.05.002.

[14] K. Villa, C. Echavarria, and D. Blessent, "Wood walls insulated with coconut fiber," DYNA, vol. 86, no. 210, pp. 333–337, 2019, https://doi.org/10.15446/dyna.v86n210.73685.

[15] X. Qin, W. Yang, Z. Zhang, and Z. Chen, "Research on the design and noise reduction performance of periodic noise barriers based on nested structure," J. Clean. Prod., vol. 476, art. no. 143708, 2024, https://doi.org/10.1016/j.jclepro.2024.143708.

[16] D. Suescún-Díaz, J. A. Chala-Casanova, and G. Ule-Duque, "Reducción de ruido en el cálculo de la reactividad con filtro digital y cuadraturas de Gauss-Legendre," Inf. Tecnol., vol. 33, no. 6, pp. 45–54, 2022, https://doi.org/10.4067/s0718-07642022000600045.

[17] P. Rastogi, C. H. Venner, C. W. Visser, and Y. Wijnant, "Additive manufacturing of functionally graded foams for acoustic insulation and absorption," Appl. Acoust., vol. 228, art. no. 110269, 2025, https://doi.org/10.1016/j.apacoust.2024.110269.

# Modeling the Stress-Strain Curve of Confined Concrete Using Ensemble Machine Learning Models

Alex B. Casilla Gallegos

alex.casilla@utec.edu.pe

Independent Researcher Civil Engineer

Recibido: 18 Mayo 2025 / Publicado: 24 Abril 2026
https://doi.org/10.26439/ciic2025.8896

ABSTRACT. The objective of this research is to develop an efficient and broadly applicable data-driven model capable of determining the stress-strain curve of confined concrete. Therefore, experimental data of 115 specimens of reinforced concrete columns with square and circular cross-sections were collected from previous investigations in which uniaxial compression tests were performed. Using this data, Random Forest (RF), Adaptive Boosting (AdaBoost), and Extreme Gradient Boosting (XGBoost) models were evaluated to define the most accurate model. Subsequently, the final selected model (based on XGBoost) was optimized, achieving $R^2$ values of 0.97 for the peak stress of confined concrete ($f_{cc}$), 0.93 for the axial strain at peak confined stress ($\varepsilon_{cc}$), and 0.81 and 0.73 for the axial strains at which stress drops to 85 % ($\varepsilon_{85}$) and 50 % ($\varepsilon_{50}$), respectively, when evaluated with the testing data. In addition, the SHapley Additive exPlanations (SHAP) technique was used to explain and determine the importance of different parameters in the outcome of the predictive model. Based on the predictions of the XGBoost model, a proposed stress-strain curve was formulated. Finally, a comparison of $f_{cc}$, $\varepsilon_{cc}$, and the stress-strain curve was performed taking into account the experimental results, the previous models, and the proposed model. The comparison results indicate that the proposed model shows a closer agreement with the experimental data.

*Index Terms* Confined concrete, ensemble models, machine learning (ML), stress-strain curve.

*Thematic Axes* Construction processes and new technologies.

Nomenclature

| | |
|---|---|
| $a_c$ | Cross-sectional area of the confined concrete core. |
| $a_t$ | Total cross-sectional area. |
| AC | Area between curves. |
| $b$ | Dimension of column cross-section. |
| $b_c$ | Dimension of core cross-section. |
| $cc$ | Concrete cover thickness. |
| $cfg$ | Configuration of transverse reinforcement. |
| $d_l$ | Diameter of longitudinal reinforcement. |
| $d_t$ | Diameter of transverse reinforcement. |
| $D_{x\%}$ | Percentage of predictions within ±x% of the experimental value. |
| $E_c$ | Elastic modulus of the concrete. |
| $\varepsilon_{50}$ | Axial strain at which stress drops to 50% of $f_{cc}$. |
| $\varepsilon_{85}$ | Axial strain at which stress drops to 85% of $f_{cc}$. |
| $\varepsilon_{cc}$ | Axial strain at peak confined stress. |

| | |
|---|---|
| $f_c$ | Compressive strength of unconfined concrete. |
| $f_{cc}$ | Peak stress of confined concrete. |
| $f_l$ | Yield stress of the longitudinal steel. |
| $f_t$ | Yield strength of the transverse steel. |
| *FD* | Fréchet distance. |
| *MARD* | Mean absolute relative deviation. |
| $R^2$ | Coefficient of determination. |
| *RMSE* | Root mean square error. |
| $\rho_c$ | Volumetric ratio of the longitudinal steel in the cross-section. |
| $\rho_s$ | Volumetric ratio of the transverse steel in the concrete core. |
| $S_l$ | Distance between perimeter longitudinal reinforcements. |
| $S_t$ | Spacing of transverse reinforcements (equivalent to *s*). |

## I. Introduction

COLUMNS are prone to sustaining inelastic deformations during earthquakes. As a mitigation measure, transverse reinforcement is provided in these structural elements to confine the concrete core, thereby enhancing its inelastic deformation capacity without any reduction in strength.

Given the benefits of confinement, numerous investigations have focused on analyzing the stress-strain curve of confined concrete [1], [2], and [3], to gain a deeper understanding of the material's structural behavior. However, the main limitation is that these studies propose models that are only moderately useful for very specific specimens, i.e., their range of application is reduced.

The objective of this research is to develop an efficient and general data-driven model to determine the stress-strain curve of confined concrete using ensemble machine learning (ML) techniques. In contrast to mechanical models, the proposed model is applicable to a wider range of cases, reduces error propagation resulting from model assumptions, and provides more information about the stress-strain curve using fewer input data. The development of the model is based on ML, which requires a training process using ensemble models within the framework of supervised learning. The structure of this paper is divided into four sections: model implementation and results, explainability of the final model, proposal of the stress-strain curve, and comparison with previous models.

## II. Background

### *A. Confined Concrete*

The confinement of the specimens is achieved by incorporating transverse reinforcement. This type of confinement is referred to as passive as it becomes effective only when the transverse deformations become significant due to progressive internal cracking. The characteristics of the transverse steel vary according to the shape of the specimen. For circular cross-sections, spiral or circular reinforcement is used, whereas for quadrangular cross-sections, quadrangular reinforcement is used. The benefits of confinement include an increase in maximum stress and improved ductility of the elements [4]. The latter benefit is of great importance for seismic design as greater ductility enables structural elements to withstand higher seismic demands.

### *B. Ensemble ML Techniques*

Predicting the stress-strain curve of reinforced concrete constitutes a regression problem within the category of supervised ML algorithms. Among these supervised algorithms are weak learners and ensemble methods, the latter combining multiple weak learners to enhance the accuracy and efficiency of the predictions [5]. For this problem, three ensemble models were selected, Random Forest (RF), Adaptive Boosting (AdaBoost), and Extreme Gradient Boosting (XGBoost).

The RF model is based on the bagging method, which employs simple parallel algorithms. In this approach, decision trees are trained concurrently, and the model's final prediction is obtained as the arithmetic mean of the individual submodel outputs [6]. In addition, the AdaBoost and XGBoost models are based on the boosting method, using simple serial algorithms. These models generate new predictors that iteratively

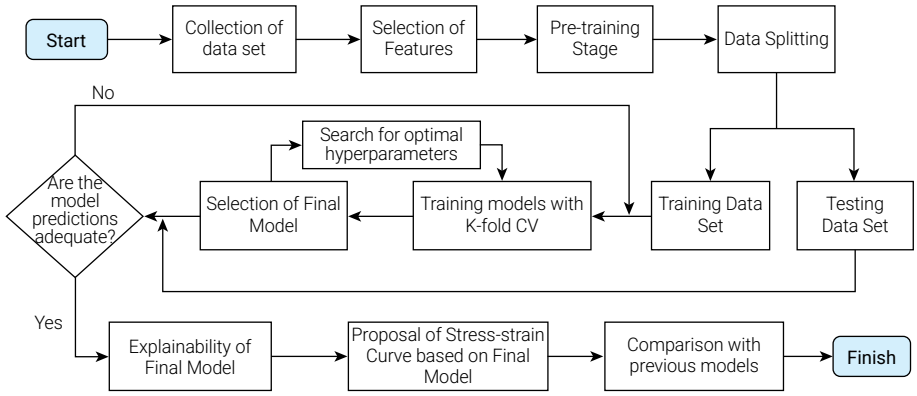


Fig. 1 Framework for the development and evaluation of a predictive model.

correct the errors of their predecessors. However, the models differ in that AdaBoost adjusts the weights at each iteration, giving greater emphasis to erroneous predictions [7], whereas XGBoost adjusts the new predictor to the residual errors made by the previous predictor [8].

*C. Performance Metrics*

To evaluate the predictions of the outputs, coefficient of determination ($R^2$), root mean square error (*RMSE*), mean absolute relative deviation (*MARD*), and $D_{x\%}$ metrics were implemented. This last metric represents the fraction of the dataset for which the relative difference does not exceed a predefined threshold; in this study, a threshold of 10 % was considered [9], [10]. The mathematical expressions for said metrics are shown below:

Where $\hat{y}_i$ is the value predicted by the model, $y_i$ is the real value, $\bar{y}$ is the average value of the samples, *N* is the number of samples, *countif* is a function that counts the number of data points that satisfy the condition in brackets, and *abs* is a function that takes the absolute value of its argument.

In addition, two metrics were used to compare the proposed and previous models against the experimental curve: the Area between Curves (AC), which estimates the total area between curves using quadrilaterals, and Fréchet Distance (FD), which quantifies the minimum continuous distance required to traverse both curves [10].

$$R^2 = 1 - \frac{\sum_{i=1}^{N}(\hat{y}_i - y_i)^2}{\sum_{i=1}^{N}(y_i - \bar{y})^2} \quad (1)$$

$$RMSE = \frac{1}{N}\sum_{i=1}^{N}(\hat{y}_i - y_i)^2 \quad (2)$$

$$MARD = Median\left(\left|\frac{\hat{y}_i - y_i}{y_i}\right|\right) \quad (3)$$

$$D_{x\%} \quad \frac{counti\,f\left[abs\left(\frac{\hat{y}_i - y_i}{y_i}\right) \le x\%\right]}{N} \quad (4)$$

## III. Methodology

In this research, a framework for developing and evaluating a predictive model is proposed, as illustrated in Fig. 1. The process began with the collection of the data set from previous investigations in which uniaxial compression tests were performed. This was followed by feature selection, a pre-training stage, and the splitting of the data set into training and testing. Subsequently, hyperparameter optimization and K-fold cross-validation (CV) were carried out to select the best performing model. Once the final model was obtained, its predictive explainability was evaluated, and a stress-strain curve was formulated based on its outputs. Finally, a comparison was made with previous models.

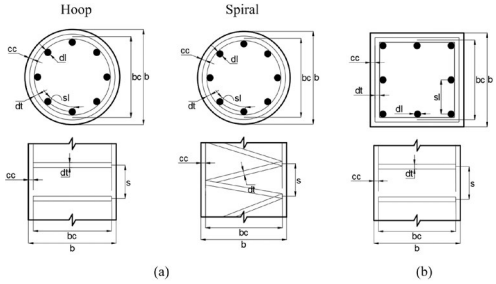


Fig. 2 Details of the specimens collected. (a) Circular Section. (b) Square Section.

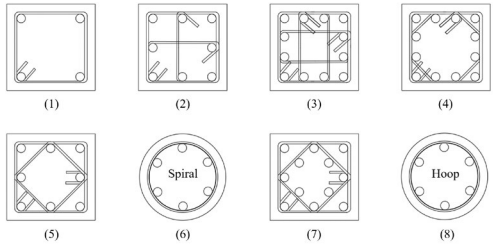


Fig. 3 Configuration of transverse steel (cfg).

TABLE I

Statistical Information of Input Features from the Data Set

| | Input 1 $f_c$ | Input 2 $a_c/a_t$ | Input 3 $d_l/s_l$ | Input 4 $\rho_s f_t/f_c$ | Input 5 $\rho_c f_l/f_c$ | Input 6 $s_t$ |
|---|---|---|---|---|---|---|
| Mean | 78.4 | 0.82 | 1234.38 | 16.22 | 10.6 | 69.7 |
| STD | 33.83 | 0.08 | 624.08 | 14.31 | 6.21 | 40.97 |
| Min. | 18.5 | 0.72 | 0 | 1.26 | 0 | 20 |
| Max. | 129.17 | 0.96 | 3062.4 | 79.88 | 27.65 | 300 |

## IV. Model Implementation and Results

### A. Dataset and Selection of Features

The dataset had a total of 115 specimens. The data were extracted from [2], [3], [11], [12], [13], and [14], where they performed uniaxial compression tests on confined concrete specimens. This data set included specimens of normal and high-strength concrete and of square and circular cross-sections, as shown in Fig. 2.

Based on the information collected and the typical design parameters, the final features of the proposed model were defined: six inputs and four outputs. Table I and Table II show statistical information of the features.

It should be noted that in addition to the aforementioned inputs, the categorical variable input *cfg*, representing the configuration of the transverse reinforcement, was considered. Within the selected dataset, eight types of *cfg* were included, as shown in Fig. 3.

### B. Model Training and Selection

As part of the pre-training stage, the output variables were transformed into logarithmic space to improve data distribution. Feature scaling was also applied to reduce the dispersion of input values. The dataset was randomly partitioned, allocating 70 % for training and 30 % for testing. During the training stage, the three ensemble models—RF, AdaBoost, and XGBoost—were tuned. To prevent overfitting, the K-fold CV technique with five folds was used.

Table III summarizes the performance metrics for each output. Considering all metrics, it is evident that the XGBoost model achieves better results for outputs $f_{cc}$ and $\varepsilon_{85}$, whereas RF performs best for $\varepsilon_{50}$. In the case of output $\varepsilon_{cc}$, similar results are obtained. In such a way, the RF and XGBoost models present similar global optimal behavior, the latter being slightly better. For the final choice, the XGBoost model was chosen because, in addition to the aforementioned advantages, its greater complexity enables it to handle unbalanced data and categorical variables.

TABLE II
STATISTICAL INFORMATION OF OUTPUT FEATURES FROM THE DATA SET

| | Output 1 ($f_{cc}$) | Output 2 ($\varepsilon_{cc}$) | Output 3 ($\varepsilon_{85}$) | Output 4 ($\varepsilon_{50}$) |
|---|---|---|---|---|
| Mean | 84.11 | 0.0051 | 0.0091 | 0.0165 |
| STD | 31.48 | 0.0038 | 0.0077 | 0.0119 |
| Min. | 22.28 | 0.0025 | 0.0031 | 0.0031 |
| Max. | 150 | 0.0281 | 0.0564 | 0.0603 |

TABLE III
RESULTS OF CROSS-VALIDATION (CV)

| Output | Metrics | RF | AdaBoost | XGBoost |
|---|---|---|---|---|
| $f_{cc}$ | $R^2$ | 0.93 | 0.92 | 0.92 |
| | $D_{10\%}$ | 71.25 | 68.75 | 76.25 |
| | *MARD* | 0.071 | 0.076 | 0.072 |
| | *RMSE* | 8.2186 | 8.8122 | 8.6559 |
| $\varepsilon_{cc}$ | $R^2$ | 0.51 | 0.5 | 0.47 |
| | $D_{10\%}$ | 35 | 23.75 | 23.75 |
| | *MARD* | 0.25 | 0.269 | 0.239 |
| | *RMSE* | 0.0022 | 0.0022 | 0.0021 |
| $\varepsilon_{85}$ | $R^2$ | 0.6 | 0.33 | 0.57 |
| | $D_{10\%}$ | 38.75 | 23.75 | 43.75 |
| | *MARD* | 0.209 | 0.293 | 0.21 |
| | *RMSE* | 0.0038 | 0.0044 | 0.0036 |
| $\varepsilon_{50}$ | $R^2$ | 0.73 | 0.64 | 0.61 |
| | $D_{10\%}$ | 23.75 | 17.5 | 18.75 |
| | *MARD* | 0.314 | 0.385 | 0.309 |
| | *RMSE* | 0.0056 | 0.0065 | 0.0056 |

### C. *Optimization and Validation of the Final Model*

To optimize the hyperparameters of the XGBoost model, the K-fold CV search technique was used. The grid search was conducted using K = 5 for CV. The optimized parameters were: learning_rate [0.1, 0.15, 0.2, 0.25, 0.3], max_depth [2, 3, 4, 5, 6, 7, 8], n_estimators [20, 30, 40, 50, 60, 70, 80, 90, 100, 110, 120]. The results show that the combination of hyperparameters that optimize the predictions is given when learning_rate = 0.2, max_depth = 5, n_estimators = 50. The optimized model was used to generate predictions for both the training and testing data. The graphical results are presented in Fig. 4, and the corresponding metrics are summarized in Table IV. Considering the testing data as unseen by the model, the performance metrics decreased in the following order: $f_{cc}$, $\varepsilon_{cc}$, $\varepsilon_{85}$, and $\varepsilon_{50}$. In terms of $R^2$, all four outputs exceeded 0.7, with values of 0.97 for $f_{cc}$, 0.93 for $\varepsilon_{cc}$, 0.81 for $\varepsilon_{85}$, and 0.73 for $\varepsilon_{50}$. Thus, the optimized model demonstrates a satisfactory level of predictive accuracy when applied to unseen data.

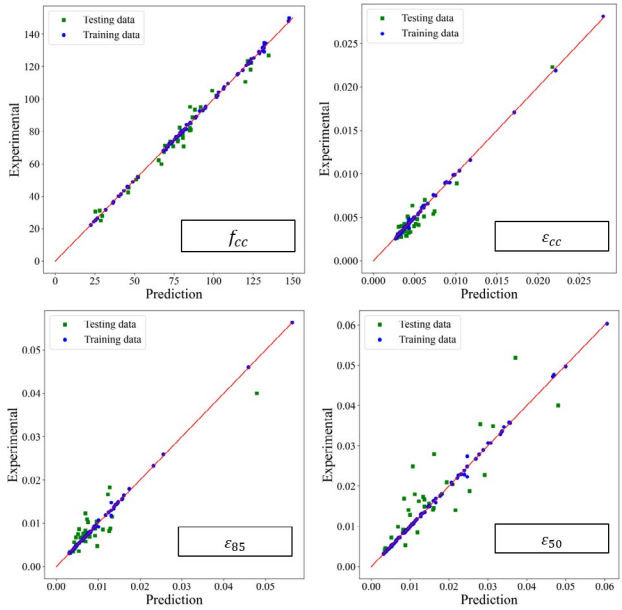


Fig. 4 XGBoost model prediction for training and testing data.

TABLE IV

METRICS OF THE XGBOOST MODEL FOR TRAINING AND TESTING DATA

| Data | Metrics | | | | |
|---|---|---|---|---|---|
| Training | $R^2$ | 1 | 1 | 1 | 1 |
| | $D_{10\%}$ | 100 | 98.75 | 97.50 | 98.75 |
| | *MARD* | 0.005 | 0.016 | 0.015 | 0.014 |
| | *RMSE* | 0.7534 | 0.0001 | 0.0003 | 0.0005 |
| Testing | $R^2$ | 0.97 | 0.93 | 0.81 | 0.73 |
| | $D_{10\%}$ | 82.86 | 37.14 | 31.43 | 28.57 |
| | MARD | 0.054 | 0.158 | 0.229 | 0.224 |
| | RMSE | 4.5349 | 0.0009 | 0.0028 | 0.0055 |

## V. EXPLAINABILITY OF THE FINAL MODEL

The SHapley Additive exPlanations (SHAP) algorithm was used as the primary approach to explain the model. This algorithm is based on game theory to interpret the behavior of ML models [15]. The final model was explained using two complementary approaches: first, through the SHAP Summary Plot, SHAP Dependence Plot, and SHAP Interaction Values; and second, through the SHAP Force Plot.

### *A. Global Explainability*

For the global explanation, the SHAP Summary Plot was used as it integrates both the importance of the input features and their corresponding effects on the model outputs. The results are presented in Fig. 5.

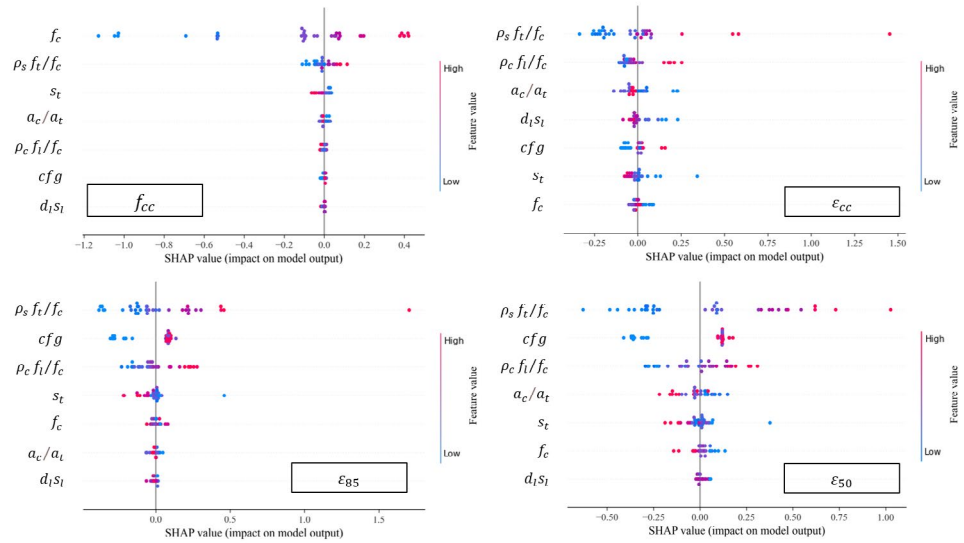


Fig. 5 SHAP Summary Plot for the final model.

For the output $f_{cc}$, it is observed that $f_c$ and $\rho_s f_t/f_c$ have the greatest impact, whereas for $\varepsilon_{cc}$ the inputs with the greatest impact are $\rho_s f_t/f_c$ and $\rho_c f_l/f_c$. In both cases, the mentioned inputs have a positive effect on the outputs.

In the case of the outputs $\varepsilon_{85}$ and $\varepsilon_{50}$, it is observed that the inputs $\rho_s f_t/f_c$ and *cfg* have greater impact and a positive effect. It should be emphasized that in the case of input *cfg* the trend does not refer to a numerical value but to the types of cross-sectional configurations shown in Fig. 3. In addition, it is observed that inputs such as $a_c$ / $a_t$ and $s_t$ have a negative effect since as their values increase the outputs decrease.

Additionally, SHAP Dependence Plot and Interaction Values were employed to relate the output parameters $f_{cc}$ and $\varepsilon_{cc}$ to the transverse strengthening index $\rho_s f_t/f_c$ and the interaction values. A clear interaction between $s_t$ and $\rho_s f_t/f_c$ was evidenced, as shown in Fig. 6.

Based on these results, it is inferred that as the values of $\rho_s f_t/f_c$ increase they cause greater impact on $f_{cc}$ and $\varepsilon_{cc}$. In that sense, it is confirmed that $\rho_s f_t/f_c$ has a greater impact on $\varepsilon_{cc}$, with an approximate maximum SHAP value of 1.5, while for $f_{cc}$ the approximate maximum SHAP value is 0.1.

Regarding the interaction, it is evident that as $\rho_s f_t/f_c$ decreases, the value of $s_t$ increases. In such a way, it is determined that the transverse reinforcement ratio is influenced by the transverse reinforcement spacing since as the transverse reinforcement spacing increases the amount of transverse reinforcement in the specimen decreases.

*B. Local Explainability*

For the local explanation, the SHAP Force Plots were applied for the testing data specimens CS23 and CS16, as shown in Fig. 7 and Fig. 8, respectively. In this manner, we intend to analyze individually the behavior of the inputs over the outputs.

For the output $f_{cc}$, it is observed that higher values of $f_c$ is high there is a positive impact, whereas lower values produce a negative impact. In both cases, for $\varepsilon_{cc}$ it is observed that $\rho_c f_l/f_c$ impacts positively, which evidences the importance of longitudinal reinforcement at the peak point. Finally, in the case of the remaining outputs, the importance of transverse reinforcement is confirmed, as indicated by the positive impact of $\rho_s f_t/f_c$ and the negative impact of $s_t$.

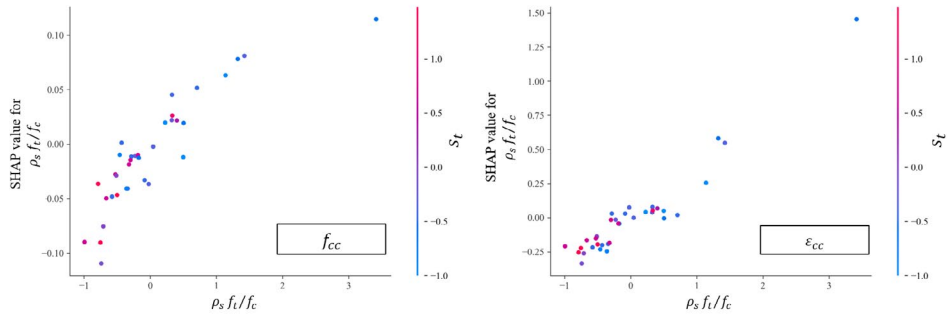


Fig. 6 SHAP feature dependence plot with interaction visualization for the final model.

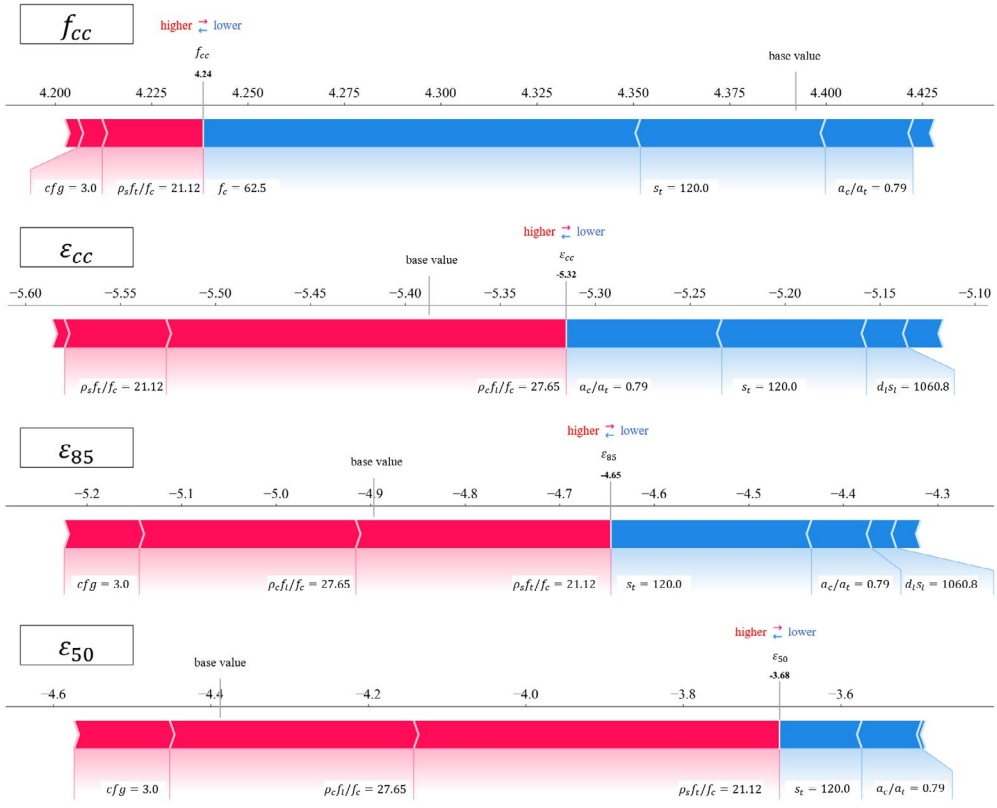


Fig. 7 SHAP Force Plot for specimen CS23.

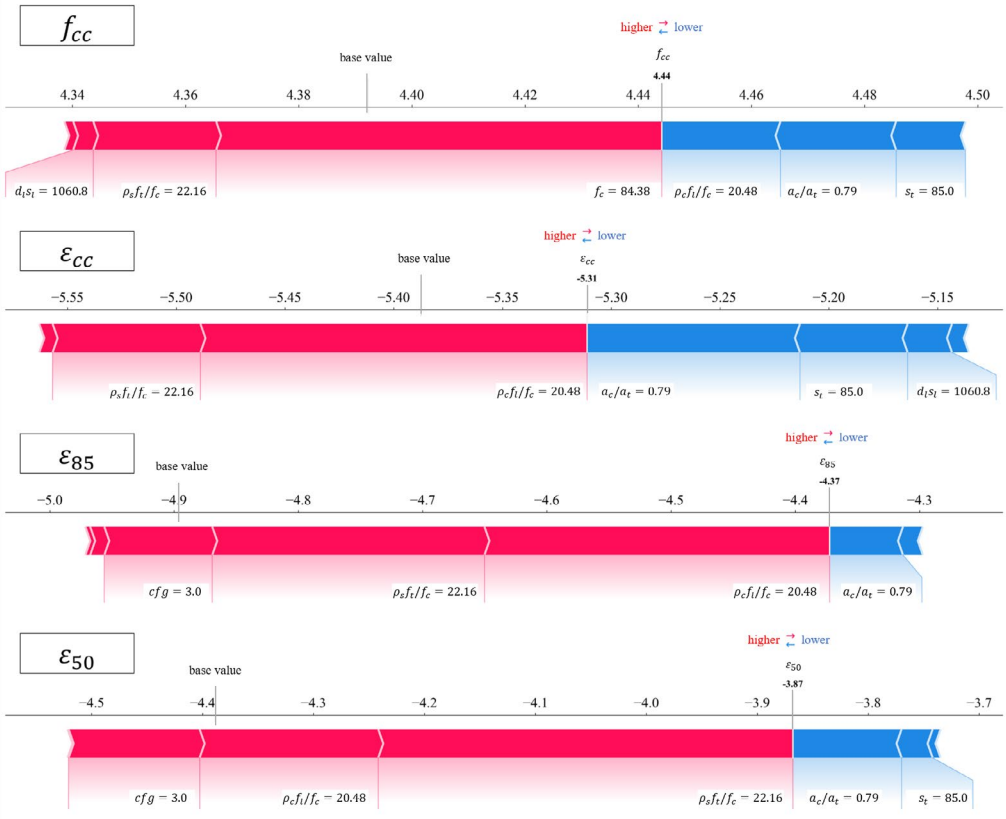


Fig. 8 SHAP Force Plot for specimen CS16.

## VI. Proposal of Stress-Strain Curve

Based on the outputs of the XGBoost model, a two-branch stress-strain curve was proposed.

### *A. Ascending Branch*

For the ascending branch, the coordinates of the curve peak ($\varepsilon_{cc}$ and $f_{cc}$) of the XGBoost model, and the slopes at the beginning (elastic modulus $E_c$) and end (zero) of this section were considered. It should be noted that the formulation of Mander (5) was used to calculate $E_c$.

$$E_c = 5000\sqrt{fc}\,MPa \tag{5}$$

Previous models indicate that a parabolic function adequately fits the experimental ascending curve. However, the Fafitis and Shah (6) approach was adopted for this proposal because it allows the use of all the available information and is not limited to only three data.

$$f_c = C_1{\varepsilon_c}^n + C_2\varepsilon_c + C_3 \tag{6}$$

Thus, the formulation (7) was obtained for the ascending branch of the curve.

$$f_c = E_c\varepsilon_c\left[1 - \frac{1}{n}\left(\frac{\varepsilon_c}{\varepsilon_{cc}}\right)^{n-1}\right] \tag{7}$$

Where:

$$n = \frac{E_c\varepsilon_{cc}}{E_c\varepsilon_{cc} - f_{cc}} \tag{8}$$

TABLE V

COMPARISON OF THE MODELS FOR THE OUTPUTS $f_{cc}$ AND $\varepsilon_{cc}$

| Output | Metrics | Mander | Hoshikuma | Razvi | XGBoost |
|---|---|---|---|---|---|
| $f_{cc}$ | $R^2$ | 0.19 | 0.68 | 0.77 | 0.99 |
| | $D_{10\%}$ | 23.75 | 42.5 | 48.75 | 96.25 |
| | MARD | 0.187 | 0.126 | 0.1 | 0.019 |
| | RMSE | 21.8265 | 13.8337 | 11.6435 | 2.7134 |
| $\varepsilon_{cc}$ | $R^2$ | 0.54 | 0.16 | 0.32 | 0.93 |
| | $D_{10\%}$ | 27.5 | 20 | 20 | 81.25 |
| | MARD | 0.224 | 0.233 | 0.204 | 0.064 |
| | RMSE | 0.0012 | 0.0016 | 0.0014 | 0.0005 |

*B. Falling Branch*

For the falling branch, the coordinates of the curve peak ($\varepsilon_{cc}$ and $f_{cc}$) predicted by the XGBoost model, along with two points corresponding to 85% and 50% of $f_{cc}$ were considered. Like the Hoshikuma model, the downward portion of the curve was idealized as a linear function (9).

$$y - y_1 = m(x - x_1) \tag{9}$$

However, this proposal differs in that an average slope ($m_c$) was calculated between the slope from the peak point to the point at 85% of $f_{cc}$ ($m_A$), and the peak point and the point at 50% of $f_{cc}$ ($m_B$). Thus, (10) was obtained for the downward portion of the curve.

$$f_c = m_c(\varepsilon_c - \varepsilon_{cc}) + f_{cc} \tag{10}$$

## VII. COMPARISON WITH PREVIOUS MODELS

In this section, two types of comparison were conducted between the experimental results, the previous models, and the proposed XGBoost model. The types of comparison were specific values $f_{cc}$ and $\varepsilon_{cc}$, and the stress-strain curve. It should be noted that among the previous models, Razvi's model was excluded from this latter comparison because its approach to the curve is identical to that of Mander.

*A. Comparison of $f_{cc}$ and $\varepsilon_{cc}$*

To ensure a fair comparison, only specimens within the application range of the previous models by Mander, Hoshikuma, and Razvi were considered. Additionally, specimens exhibiting atypical behavior, particularly those with unusually high strain values, were excluded. As a result, the comparison was carried out using 80 specimens, as shown in Fig. 9 and Fig. 10. It should be noted that the vertical axis represents the experimental results from previous investigations, while the horizontal axis shows the predictions from both the mechanical models and the proposed model. The corresponding performance metrics are presented in Table V.

In general, the results of $f_{cc}$ are evidently more accurate than the results of $\varepsilon_{cc}$, across all models. Within the mechanical models, it is observed that predictions of $f_{cc}$ by Razvi show better accuracy; while predictions of $\varepsilon_{cc}$ by Mander provide a better fit. In the case of the XGBoost model, the predictions exhibit superior performance compared to all other models, with $R^2$ and $D_{10\%}$ values greater than 0.9 and 80, respectively.

Regarding Fig. 10, it should be noted that the mechanical models exhibit increasing dispersion as the strain level rises. This is due to mathematical simplifications and idealizations that do not accurately represent the actual behavior of confined concrete at high-strain levels. In contrast, the proposed model shows reduced dispersion, which is attributed to the inclusion of a sufficient number of high-strain specimens in the training dataset.

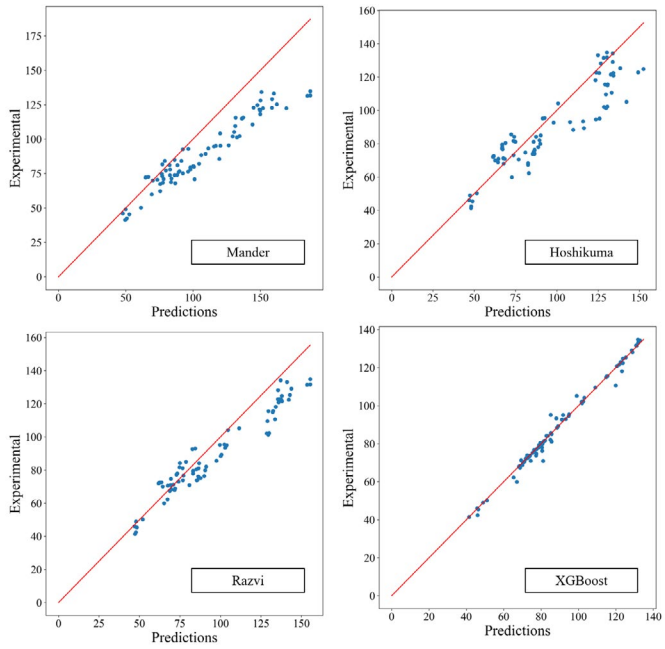


Fig. 9. Prediction of for previous and XGBoost models.

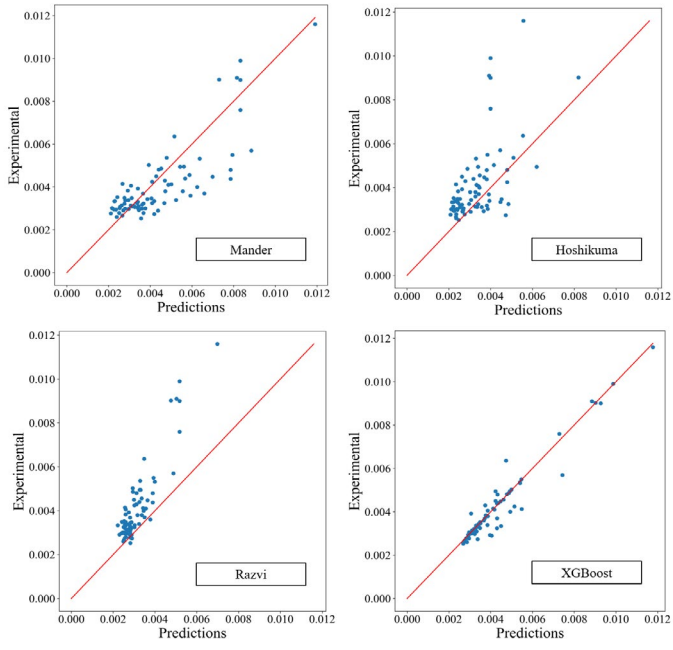


Fig. 10. Prediction of for previous and XGBoost models.

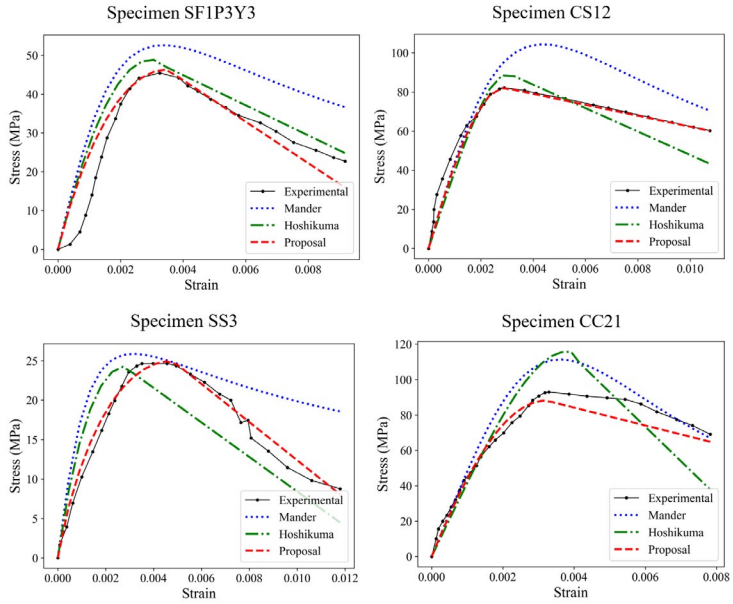


Fig. 11. Comparison of the stress-strain curve models.

*B. Comparison of Stress-Strain Curve*

For the curve comparison, four specimens, included in the testing dataset, were considered. Among the evaluated models, Mander's model employs a single expression, whereas Hoshikuma's model and the proposed model use two expressions to represent the complete stress-strain curve. The results of the curve modeling are shown in Fig. 11. For an accurate interpretation of the curves, the AC and FD metrics were used. The corresponding results are shown in Table VI.

Among the previous models, it is evident that Hoshikuma's model provides a closer approximation to the experimental curve for specimens SF1P3Y3, CS12, and SS3; whereas Mander's model performs better for specimen CC21, as Hoshikuma's approach overestimates the peak-point coordinates. For the proposed model, a strong graphical agreement with the experimental curve is observed when compared with the previous models, as evidenced by the low AC and FD values obtained for all four specimens.

The major differences between the models originate in the descending branch of the curve, where Mander's model exhibits a notably shallow slope compared to the experimental data, whereas Hoshikuma's model and the proposed model display behavior more closely aligned with the actual response. This behavior is attributed to the fact that Mander's model defines the descending branch without incorporating any reference points from that portion of the curve. Although both the Hoshikuma model and the proposed model define a linear function for the descending branch, the proposed model offers an advantage because its slope is derived from two points on the descending portion by averaging the corresponding local slopes.

## VIII. Conclusions

This research proposed the development of an ML model to predict $f_{cc}$, $\varepsilon_{cc}$, $\varepsilon_{85}$ and $\varepsilon_{50}$ of the stress-strain curve, and subsequently to model the entire curve using (7) and (10). To develop the model, a total of 115 confined concrete specimens were collected and used to train the RF, AdaBoost, and XGBoost models. Based on the CV results, XGBoost was selected as the final model. Subsequently, the final model was

TABLE VI

Stress-Strain Curve Comparison Metrics

| Specimen | Metrics | Mander | Hoshikuma | Proposal XGBoost |
|---|---|---|---|---|
| SF1P3Y3 | FD | 13.94 | 4.51 | 6.78 |
| | AC | 0.11 | 0.06 | 0.05 |
| CS12 | FD | 22.2 | 17 | 8.71 |
| | AC | 0.2 | 0.15 | 0.08 |
| SS3 | FD | 9.8 | 4.29 | 2.52 |
| | AC | 0.06 | 0.05 | 0.02 |
| CC21 | FD | 18.39 | 31.26 | 4.85 |
| | AC | 0.09 | 0.14 | 0.09 |

optimized by grid search. In addition, SHAP was used to provide both global and local explanations of the final model. Considering the outputs of the final XGBoost model, a stress-strain curve was proposed. Finally, the predictions from the proposed and the previous models were compared against experimental data.

To begin with, the pre-training stage plays a critical role in obtaining results. Therefore, it is recommended to transform the outputs into logarithmic space, which improves the distribution of the collected information, and apply feature scaling, which reduces the dispersion of the inputs. As shown in the CV results, the XGBoost model performs better than the RF and AdaBoost models.

During the optimization process, the following hyperparameters were selected: learning_rate = 0.2, max_depth = 5, n_estimators = 50. The predictions with the optimized model from the testing data demonstrate favorable results. In terms of $R^2$, all four outputs exceeded 0.7, with values of 0.97 for $f_{cc}$, 0.93 for $\varepsilon_{cc}$, 0.81 for $\varepsilon_{85}$, and 0.73 for $\varepsilon_{50}$.

In the model explanation, it is evident that the output $f_{cc}$ is highly influenced by $f_c$, and $\varepsilon_{cc}$ is highly influenced by $\rho_s f_t/f_c$ and $\rho_c fl/f_c$. In the case of $\varepsilon_{85}$ and $\varepsilon_{50}$, the parameters $\rho_s f_t/f_c$ and $cfg$ have greater impact. Unlike all parameters, $a_c/a_t$ and $s_t$ have an opposite effect since as their values increase, the outputs have a negative impact. Furthermore, it is observed that when $\rho_s f_t/f_c$ decreases, the value of $s_t$ increases.

Additionally, the XGBoost model achieves better performance than the previous models for $f_{cc}$ and $\varepsilon_{cc}$. Also, in the curve comparison, it is observed that the proposed model shows a high degree of similarity to the experimental curve compared to the other models as it provides a more accurate prediction of the peak point and of the curve's slope or decay rate.

Furthermore, the developed model has a broad range of applications. Its predictions are applicable to both normal and high strength concrete specimens, whether square or circular in shape, and can accommodate up to eight variations in transverse reinforcement configurations. It is important to note that the input values for the specimens must fall within the minimum and maximum limits of the dataset, as shown in Table I.

Regarding the dataset, it was collected from previous research. However, having experimental data generated specifically for this study would have been advantageous, as it would not only have increased the available data volume but also influenced the selection of the model inputs and outputs.

Finally, future research should focus on integrating hybrid approaches that combine data-driven models with physical constraints, which could improve both the interpretability and reliability of the model for structural design applications.

## References


[1] A. Fafitis and S. P. Shah, "Lateral Reinforcement for High-Strength Concrete Columns," in *ACI Special Publication SP-87, High-Strength Concrete*, American Concrete Institute, Farmington Hills, MI, USA, Sept. 1985, pp. 213–232.

[2] J. B. Mander, M. J. N. Priestley, and R. Park, "Theoretical Stress-Strain Model for Confined Concrete," *Journal of Structural Engineering*, vol. 114, no. 8, pp. 1804–1826, Sep. 1988, doi: https://doi.org/10.1061/(asce)0733-9445(1988)114:8(1804)

[3] J Hoshikuma, K. Kawashima, K. Nagaya, and A. Taylor, "Stress-Strain Model for Confined Reinforced Concrete in Bridge Piers," *Journal of Structural Engineering*, vol. 123, no. 5, pp. 624–633, May 1997, doi: https://doi.org/10.1061/(asce)0733-9445(1997)123:5(624)

[4] R. Park and T. Paulay, *Estructuras de Concreto Reforzado*, 2nd ed., Mexico City, Mexico: Limusa, 1983.

[5] A. Géron, *Hands-On Machine Learning with Scikit-Learn, Keras, and TensorFlow*, 2nd ed., Sebastopol, CA, USA: O'Reilly Media, 2019.

[6] L. Breiman, "Random Forests," *Machine Learning*, vol. 45, no. 1, pp. 5–32, Oct. 2001, doi: https://doi.org/10.1023/A:1010933404324

[7] Y. Freund and R. E. Schapire, "A Decision-Theoretic Generalization of On-Line Learning and an Application to Boosting," *Journal of Computer and System Sciences*, vol. 55, no. 1, pp. 119–139, Aug. 1997, doi: https://doi.org/10.1006/jcss.1997.1504

[8] T. Chen and C. Guestrin, "XGBoost: A Scalable Tree Boosting System," *Proceedings of the 22nd ACM SIGKDD International Conference on Knowledge Discovery and Data Mining - KDD '16*, vol. 1, no. 1, pp. 785–794, Aug. 2016, doi: https://doi.org/10.1145/2939672.2939785

[9] X. Guan, H. Burton, M. Shokrabadi, and Z. Yi, "Seismic Drift Demand Estimation for Steel Moment Frame Buildings: From Mechanics-Based to Data-Driven Models," *Journal of Structural Engineering*, vol. 147, no. 6, Jun. 2021, doi: https://doi.org/10.1061/(asce)st.1943-541x.0003004

[10] C. F. Jekel, G. Venter, M. P. Venter, N. Stander, and R. T. Haftka, "Similarity measures for identifying material parameters from hysteresis loops using inverse analysis," *International Journal of Material Forming*, vol. 12, no. 3, pp. 355–378, Jul. 2018, doi: https://doi.org/10.1007/s12289-018-1421-8

[11] B. Li, *Strength and ductility of reinforced concrete members and frames constructed using high-strength concrete*, Ph.D. dissertation, Dept. of Civil Engineering, Univ. of Canterbury, Christchurch, New Zealand, 1993.

[12] T. Nagashima, S. Sugano, H. Kimura, and A. Ichikawa, "Monotonic axial compression test on ultra-high-strength concrete tied columns," in *Proc. 10th World Conf. Earthquake Engineering (10th WCEE)*, Madrid, Spain, 1992, pp. 2983–2988.

[13] S. Razvi and M. Saatcioglu, "Confinement Model for High-Strength Concrete," *Journal of Structural Engineering*, vol. 125, no. 3, pp. 281–289, Mar. 1999, doi: https://doi.org/10.1061/(asce)0733-9445(1999)125:3(281)

[14] M. Suzuki, M. Akiyama, K.-N. Hong, I. D. Cameron, and W. L. Wang, "Stress-strain model of high-strength concrete confined by rectangular ties," in *Proc. 13th World Conf. Earthquake Engineering (13th WCEE)*, Vancouver, BC, Canada, Aug. 2004, Paper No. 3330, pp. 74–76.

[15] S. M. Lundberg, G. G. Erion, and S.-I. Lee, "Consistent individualized feature attribution for tree ensembles," *arXiv preprint arXiv:1802.03888*, 2019. [Online]. Available: http://arxiv.org/abs/1802.03888

# Methodology for Calculating the International Roughness Index (IRI) from Mobile LiDAR

Sergio López-Pinzón[1], Humberto Ramírez-Gómez[2], Wilmar Fernandez-Gomez[3]

[1] sdlopezp@udistrital.edu.co, [2] humberto.ramirez@umv.gov.co:, [3] wfernandez@udistrital.edu.co

[13] Sustainable Infrastructure Research Group, Universidad Distrital Francisco José de Caldas, Colombia | [2] Bogota's Special Administrative Unit for Bogota Road Rehabilitation and Maintenance

Recibido: 05 Mayo 2025 / Publicado: 24 Abril 2026
https://doi.org/10.26439/ciic2025.8669

ABSTRACT—**Pavement Management Systems integrate advanced decision-making tools for road management. This research addresses the automated approach for analyzing the light detection and ranging (LiDAR) data for road management. The proposed framework integrates machine learning techniques with advanced data-processing methodologies to estimate the International Roughness Index (IRI) using mobile LiDAR measurements. The data were obtained from the publicly available Lille2 and IQmulus point-cloud datasets, captured using the L3D2 mobile mapping systems. Automatic extraction of the rolling surface was performed on these datasets, enabling the subsequent automated generation of pavement profiles. In addition, the layout of edges, axes and profiles was automated. These alignments provided the corresponding Z-coordinates required for IRI computation, enabling faster and more accurate calculations. For both clouds, the differences observed in the global IRI values calculated from averaged reference profiles are small—ranging from 0.15 to 0.29 m/km for Lille2 and from 0.03 to 0.04 m/km for IQmulus. In contrast, the differences between these values and the IRI obtained from profiles generated using the simple method are substantially larger, ranging from 8.98 to 11.59 m/km for Lille2 and from 0.47 to 0.65 m/km for IQmulus. The results of this work will not only contribute to academic development in this field, but also to the practical implementation of more modern, efficient, and accurate systems for road network assessment and maintenance.**

*Index Terms*—International Roughness Index (IRI), mobile LiDAR, pavements, point clouds, road surface.

*Thematic Axes*—Construction processes and new technologies.

## I. Introduction

In countries such as the United States, New Zealand and Canada, the public road infrastructure sector benefited from management systems developed in the private sector and subsequently began to identify ways in which public administrations could adopt the best practices of private enterprise [1]. In this context, the concept of Transportation Asset Management Systems (TAMS) emerged. When applied to road infrastructure, these systems are commonly referred to as Highway Management Systems. According to the Transportation Asset Management Subcommittee of the American Association of State Highway and Transportation Officials (AASHTO), Transportation Asset Management is defined as a strategic and systematic process that encompasses the operation, maintenance, improvement, and expansion of assets throughout their life cycle. It is grounded in business and engineering

practices aimed at optimizing resource allocation. Its purpose is to ensure efficient decision-making based on quality information and clearly defined objectives, thereby maximizing asset value and performance over time.

The Transportation Asset Management Guide states that "transportation asset management is a strategic and systematic process for the operation, maintenance, updating and expansion of physical assets effectively throughout their life cycle [2]. It concentrates on business and engineering practices for the allocation and use of resources, with the objective of enabling better decision making based on high-quality data and clearly defined objectives." However, in general terms, a road administration manages typical assets such as physical infrastructure (e.g., pavements and bridges); human resources (including personnel and technical expertise); equipment and materials; and other valuable elements such as rights of way, data, computer systems, methods and technologies.

The decision-making framework for road management should be guided by asset performance targets over an extended period, i.e., with a long-term planning and analysis horizon [1]. Performance is defined as the degree to which an asset serves its users and fulfills intended purposes, measured in terms of the quality and duration of the cumulative service it provides. In other words, performance can be described as the combination of the quality of service provided by the asset and the duration of its useful life.

*A. Road infrastructure inventories*

The road infrastructure inventory is used to determine the operational and functional conditions of a roadway based on a detailed description of its physical, geometric, and design conditions. The most common method for compiling this inventory is visual inspection, which consists of surveying the sector or section under study to quantify and assess its conditions. The methodology for the visual inspection includes a complete description of three fundamental aspects: (1) road description; (2) road geometry; and (3) the pavement surface condition and complementary works.

A road description consists of recording its general characteristics, including location, direction of travel, boundaries, road type (highway, arterial, collector road, and local road), and pavement type (flexible, surface treatment, rigid, and gravel or dirt). Among the criteria that must be examined in road geometry are section length, roadway width, number of lanes, shoulder width and height, median strip, and shoulder areas. The visibility distance and braking distance available may also be analyzed. Evaluating the surface condition of the pavement involves identifying flaws, defects, or damage that compromise performance and may shorten its useful life.

The evaluation of the condition of urban roads and highways is a critical aspect of analyzing operational factors related to the infrastructure's quality and level of service. The condition of road infrastructure influences the macroscopic parameters of volume, speed, and density considered in the study of traffic phenomena. This is explained by the fact that, depending on the road's geometric characteristics, pavement condition, and associated structures, users (drivers and pedestrians) determine their preferences when making any trip. This, in turn, affects vehicular and pedestrian flow behavior, the speeds achieved by vehicles, and the outcomes of the analysis performed on the values obtained for the aforementioned parameters [3].

*B. International Roughness Index (IRI)*

To define the IRI, a mathematical model is used that simulates the suspension and masses of a typical vehicle traveling along a section of road at a given speed. This model is known by its English acronym, QCS (Quarter Car Simulation), as it represents a quarter of a four-wheeled vehicle or a single-wheel trailer. The IRI at a point on a roadway is defined as the ratio of the relative movement accumulated by the suspension of a typical vehicle, to the distance traveled by that vehicle. If the longitudinal road profile, $y(x)$, and the car speed, $V$, are known, the movement, $z_1$ and $z_2$, of the masses, $m_1$ and $m_2$, that make up the model can be calculated at each point.

In turn, the vehicle's response can be expressed in terms of the rectified slope (RS), at each point where the longitudinal profile is discretized.

$$RS_i = |Z'_1 - Z'_2|i$$

where, $z_1$ and $z_2$ represent the gradients of the vehicle masses at different positions, *i*, along the wheel path. Finally, the IRI is obtained as the arithmetic mean of the rectified gradient along the path traveled. Therefore,

$$\text{IRI} = [\sum_{i=1}^{n} RS_i] / \text{n}$$

where *n* is the number of points counted.

It is obvious that a vehicle's dynamic response while traveling on a roadway, and consequently its IRI value, strongly depends on the vehicle's operating speed. To resolve this ambiguity, and after weighing the various alternatives, the International Road Roughness Experiment (IRRE) participants established 80 km/h as the reference speed for defining the IRI. This speed was chosen because the IRI coefficients obtained at this speed were considered representative of the safety and comfort perceived by users. Furthermore, this speed was deemed suitable for measurement using response-type systems.

To calculate the IRI, it is necessary to know the slopes $z'_1$ and $z'_2$ of the masses of the typical vehicle at each point along a section. These slopes are obtained recursively, based on the values calculated in the previous point. Thus, if the vehicle's motion at point *i-1* is known, the response at the next point can be calculated using the equation:

$$\{Z\}_i = [ST]\{Z\}_{i-1} + y'_i\{RS\}$$

where $\{Z\} = [Z_2', Z_2'', Z_1', Z_1'']^T$, with primes representing spatial derivatives, $y'_j = \frac{y_i - y_{i-1}}{dx}$ and represents the distance between samples, is constant within each interval, *dx* , and [*ST*] and [*RS*] are 4 *x* 4 and 4*x*1 matrices, respectively, whose coefficients depend on the sample interval, *dx*. The above system of equations can be solved for any point on the road, except for the first point of the first section where the values of $z_i'$, $z_2'$, $z_i''$ and $z_2''$ at the previous point are unknown. The above procedure for calculating the IRI is valid for intervals between measurements, *dx*, between 0.25 and 0.6 m horizontally. For shorter intervals, it is recommended to smooth the longitudinal profile to more accurately represent how a vehicle's wheel traverses the roadway section. For this purpose, either the equivalent profile is determined every 0.25 m. (ignoring intermediate points), or a running average calculated at each point with a smoothing interval of 0.25 m. In the first case, the IRI is calculated using 0.25 m intervals, and in the second case, it is calculated using the original interval, but with the smoothed profile [4].

*C. Light Detection and Ranging (LiDAR)*

LiDAR is a remote sensing method that uses a laser to measure distances. A laser scanner emits pulses of light, and when a pulse strikes a target, a portion of its photons is reflected back to the scanner. Because the scanner's position, the pulse's direction, and the time between emission and return are known, the three-dimensional (3D) location (XYZ coordinates) from which the pulse is reflected can be calculated. The laser emits millions of such pulses and records their reflections, generating a highly accurate 3D point cloud (model) that can be used to estimate the 3D structure of the target area. Most often, the scanning laser is mounted on an aircraft—usually a fixed-wing aircraft, although increasingly on drones—and scans the terrain along its flight path. Scanning lasers are also mounted on a tripod or vehicle for terrestrial laser scanning (TLS).

A pulse is the emission produced by the scanning laser. It can be considered a time-stamped group of photons. When the pulse strikes a target, some of its photons are reflected back and detected by the LiDAR system, indicating that an echo has been received. Therefore, the source of an echo is a location struck by a pulse from which photons are reflected. An emitted pulse can, and often does, produce multiple echoes. LiDAR data contains information for each echo that is received. For example, in a text format (.txt), the data are often structured so that each row contains the information associated with a single echo, including its XYZ coordinates, intensity, and order when multiple echoes are present. Most often, LiDAR data comes in a compressed LAS/LAZ format. The LAS format is a standard file format for LiDAR data storage, where the LAZ format is a compressed format of LAS. The compressed LAZ file may be as small as 50 MB, but when decompressed and converted to a text

TABLE I
CHARACTERISTICS OF POINT CLOUDS

| | Lille2 | IQmulus |
|---|---|---|
| Project | NPM3D | TerraMobilita |
| Access | https://npm3d.fr/ | http://data.ign.fr/benchmarks/UrbanAnalysis/ |
| Total RS points | 11 816 213 | 3 196 982 |
| (points/m$^2$) average | 3000 | 3000 |
| Length (m) | 350 | 200 |

file—often containing tens of millions of rows (one per echo)—its size can reach several GB. There are many specialized programs designed to process and analyze LiDAR data, and most common remote sensing and geographic information system (GIS) programs can also process LiDAR data in LAS/LAZ format.

Mobile LiDAR, defined as the 3D data acquisition system mounted on ground vehicles, is an advanced technology that enables high-resolution geospatial information to be captured efficiently and accurately [5]. This system has transformed road infrastructure surveys and analyses by offering a modern and automated alternative to traditional methods such as profilometers or static levelling.

## II. Data and Methods

Pavement profiles were obtained from two freely accessible point clouds: Lille2 [6] and IQmulus [7]. These were captured with the L3D2 [8] and Stereopolis II [9] mobile mapping systems ADDIN CSL_CITATION {"citationitems":[{"id":"ITEM-1","itemData":{"ISSN":"17689791","abstract": "Precise realistic models of outdoor environments such as cities and roads are useful for various applications. However, achieving a high level of detail over a large environment requires addressing the challenges of the volume of data to be acquired, processed and stored, as well as the overall processing time. This paper introduces an integrated on-board laser range sensing system designed to address this need. It is intended to perform geometric modeling of urban and road environments during movement. It is based on a laser range sensor mounted on a vehicle whose position is known using GPS-INS localization. It generates raw 3D range data and performs specific modelling for cities and features extraction for roads.","author":[{"droppingparticle":"","family":"Goulette","given":"F","non dropping particle":"","parse names":false,"suffix":""},{"dropping particle":"","family":"Nashashibi","given":"F","nondroppingparticle":"","parse names":false,"suffix":""},{"dropping particle":"","family":"Abuhadrous","given":"I","non dropping particle":"","parse names":false,"suffix":""},{"dropping particle":"","family":"Ammoun","given":"S","non droppingparticle":"","parsenames":false,"suffix":""},{"dropping particle":"","family":"Laurgeau","given":"C","non dropping particle":"","parse names":false,"suffix":""}],"container title":"Revue Francaise de Photogrammetrie et de Teledetection","id":"ITEM 1","issue":"185","issued":{"date parts":[["2007"]]},"page":"78 83","title":"An integrated on-board laser range sensing system for on-the-way city and road modelling","type":"article journal"},"uris":["http://www.mendeley.com/documents/?uuid=f1726048 40e1 3665 93b1 5ba3ef1a458d"]}],"mendeley":{"formattedCitation":"[8]","plainTextFormattedCitation":"[8]","previouslyFormattedCitation":"[8]"},"properties":{"noteindex":0},"schema":"https://github.com/citation style language/schema/raw/master/csl citation. json"}, respectively. The most important information from these point clouds is summarized in Table I.

The experiments were carried out on a system equipped with an Intel Core i7-10750H CPU at 2.60 GHz, running Windows 11, with 32 GB of DDR4 RAM and a 6 GB NVIDIA GeForce GTX 1660 Ti GPU. The Python language was used for

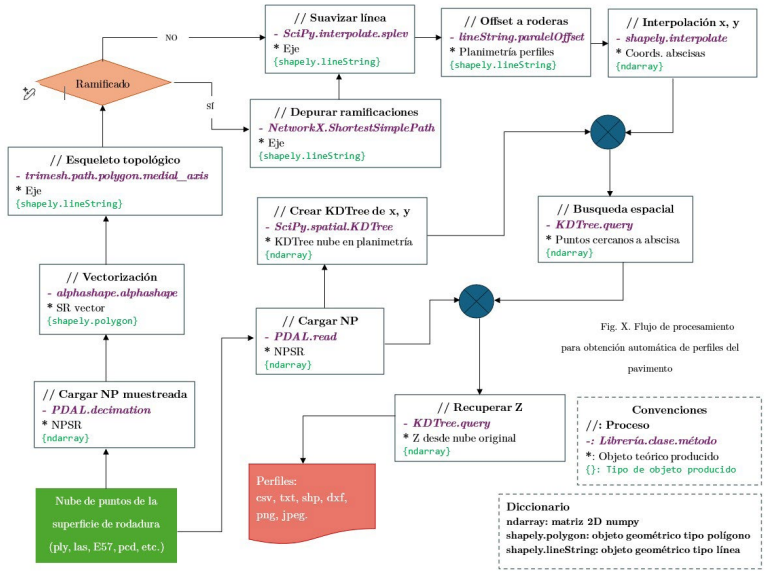


Fig. X. Flujo de procesamiento para obtención automática de perfiles del pavimento

Fig. 1. General flow for obtaining LiDAR point cloud profiles.

all development and experimentation, utilizing environment virtualization with Conda.

Obtaining a profile requires determining the topographic coordinates *x, y, z* of each point spaced 25 cm along the rut alignment. To achieve this automatically, the workflow presented in Fig. 1 must be followed. The general flow of this phase includes the following steps: vectorizing the rolling surface point cloud (RSPC), calculating the topological skeleton of the road, calculating the planimetric coordinates for each abscissa of the profile, retrieving the Z coordinate of each abscissa. The vectorization of the rolling surface converts the point cloud into a planimetric polygon for processing in advanced geometric models. This procedure, common in LiDAR data processing, involves converting coordinates into two-dimensional representations using techniques such as *α*-shapes [10]. It was implemented using the Python *α*-shape library with Shapely for handling geospatial data and PDAL for loading the point cloud in NumPy format. To optimize processing, data reduction was applied with the PDAL decimation method, minimizing the number of points without compromising the road geometry.

The topological skeleton, calculated with the Trimesh library, allows extraction of the road corridor's median axis using the *medial_axis* method, based on Voronoi diagrams [11]. In urban networks, it is necessary to eliminate branches, which was solved with NetworkX using *Shortest_Simple_Path* to extract the optimal trajectory from the skeleton. To improve the regularity of the horizontal alignment, smoothing was applied with SciPy's *splev* function, generating a *B*-spline interpolation on the calculated trajectory. Then, the planimetric coordinates of the profiles were obtained with Shapely's parallel_offset, ensuring their alignment with the tire marks.

Z coordinate retrieval was performed using a KD-tree, an efficient search structure implemented with SciPy. Three strategies were compared: nearest point mapping (NN), averaging the nearest 50 points (K50), and averaging points within a 10 cm radius (QB10). These techniques enabled accurate extraction of the 3D geometry of road profiles, facilitating the calculation of the IRI. The combination of these methodologies and tools facilitated progress towards the automation of road data processing, optimizing infrastructure assessment and maintenance.

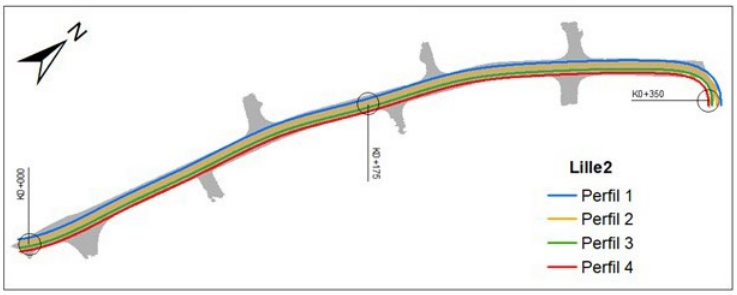


(a)


(b)

Fig. 2. Profiles on the different routes: (a) Lille2 roadway corridor in flat format and (b) IQmulus roadway corridor in flat format.

From the complete point cloud, the RSPC must be classified and obtained. Using this, the rut lines corresponding to the alignment of the vehicle tire trajectory are obtained, which in this study are referred to as profiles. For Lille2, the four rut profiles were calculated and for IQmulus, two rut profiles were computed. For both scenarios, a Δx of 0.25 m was used and in each case, three iterations were performed corresponding to the three methods for estimating the Z coordinate. The location of the tire tracks was defined based on the dimensions of each corridor and assuming an average vehicle width equal to 1.8 m. In the case of Lille2, the road is 8 m wide for two lanes, so the centerline offsets were set at 1.1 m and 2.9 m to the right and left, respectively. The IQmulus cloud has a single 3.5 m wide lane, with track locations set 0.9 m on either side of the median axis. Fig. 2 shows the location of each track profile on the road surface in vector format.

Fig. 3 shows an isometric view of the profiles. This shows the level of detail that can be collected with mobile LiDAR sensors, demonstrating that this technology provides a high-precision 3D representation, which is equivalent to, and even superior to, the information obtained through conventional topography [12]. Consequently, the profiles obtained from mobile LiDAR point clouds can be considered true profiles of the pavement and are therefore suitable for calculating the IRI, as this index corresponds to a property [13]. According to NCHRP Report 748 [14], for pavement regularity analysis, a LiDAR point cloud suitable for such analyses must have a density greater than 1000 points/m$^2$. It is also recommended that the sampling range for estimating the vertical component be between 2 and 10 cm.

Fig. 3 also shows the profiles directly from the point clouds allowing visualization of the discrepancies between the geometries obtained by the different methods. In both cases, the pink profile, corresponding to the one obtained using the nearest Z, exhibits more irregular behavior due to the peaks in both the upper and lower sections. In contrast, the profiles generated with the other two methods maintain a smoother and more consistent trajectory, to the extent that the green and blue profiles effectively merge into a single line.

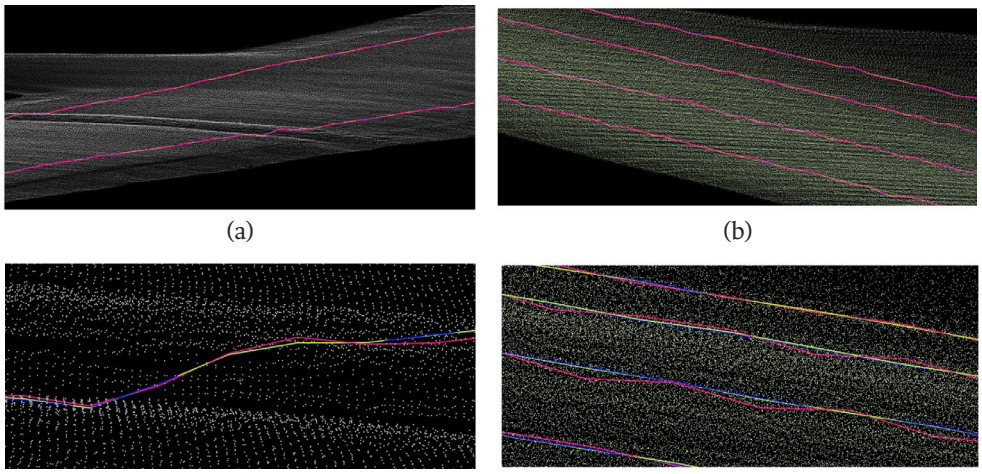

(a) (b) (c) (d)

Fig. 3. Isometric view of profiles: (a) IQmulus overview, (b) Lille2 overview, (c) IQmulus zoom, (d) Lille2 zoom.

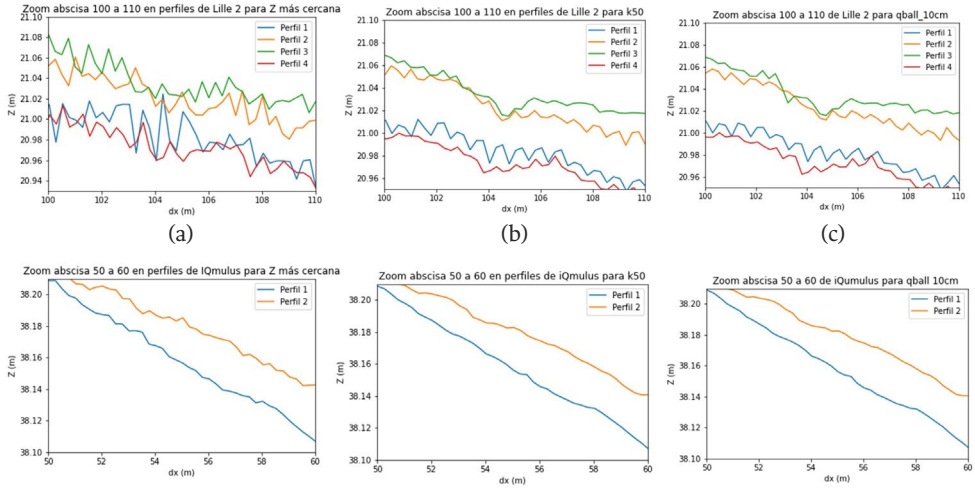


(a) (b) (c) (d) (e) (f)

Fig. 4. Detailed view of the profiles automatically generated for each Z-estimation method. (a) Left nearest Z. (b) Z average with 50 neighbors. (c) Z average 10 cm neighbors. Lille2 profiles Z-estimation method: (d) Left nearest Z. (e) Z average with 50 neighbors. (f) Z average 10 cm neighbors, IQmulus profiles.

A more detailed view of the profiles, suitable for a more precise analysis of the results, is presented in Fig. 4. This figure provides a zoomed-in view of the profiles obtained with each Z-axis estimation method over two abscissas separated by only 10 m. This figure confirms the previously described divergences in the profile geometries, as well as the more irregular behavior observed in the profiles derived from the nearest-neighbor Z-axis estimation.

TABLE II

Global IRI Results for Each Profile Analyzed for the Two Clouds Evaluated

| Z-estimation method | IRI (m/km) | | | |
|---|---|---|---|---|
| | Lille2-P1 | Lille2-P3 | IQmulus-P1 | IQmulus-P2 |
| Nearest (NN) | 17.56 | 17.52 | 6.52 | 7.33 |
| *K* = 50 | 8.43 | 6.22 | 6.01 | 6.68 |
| QueryBall = 10 cm | 8.58 | 6.51 | 5.97 | 6.65 |

TABLE III

Processing Times for Each Step of Phase 2

| Process | Response time | Impact on flow |
|---|---|---|
| RSPC Load | 3–9 s | Low |
| Vectorization / *α-shape* | 28 s–2 min | Considerable |
| Topological skeleton | Immediate (ms) | Negligible |
| Debugging / Branching | Immediate (ms) | Negligible |
| Smoothing the path | Immediate (ms) | Negligible |
| Offset | Immediate (ms) | Negligible |
| Abscissas | Immediate (ms) | Negligible |
| KD-tree creation | 1–4 s | Low |
| Recovery of *Z* | Immediate (ms) | Negligible |

## III. Results and Discussion

For the analysis and discussion, the IRIs of profiles 1 and 3 (corresponding to the external and internal wheel paths of different lanes) from the Lille2 dataset, as well as the two profiles from the IQmulus dataset were calculated using ProVAL software. The IRI results for each Z-estimation method for these profiles are presented in Table II below.

While Table II shows the total IRI for each profile, Fig. 5 exhibits the accumulated IRI on each abscissa for each profile, with the three different methods for obtaining Z. As evidenced by this table and figure, the relationship described in the profiles section remains consistent: the methods that estimate the Z value using multiple neighboring points yield similar results, whereas the nearest-neighbor method produces noticeably more divergent outcomes.

On the other hand, it should be noted that the implementation of the proposed methodology showed that the only step in this phase that requires substantial computational resources is the calculation of the concave envelope. For the other steps, the execution times are negligible, ranging from milliseconds to seconds. For IQmulus, the concave envelope calculation time was 28 s, and for Lille2, it was 2 min. Table III shows the times and their impact on the proposed workflow. It can also be observed that the profile calculation takes approximately 2 min for clouds containing up to 11,000,000 points, such as Lille2.

The clouds used in this experiment meet the suggested density as shown in Table III. The Z-retrieval method with a 10 cm radius also meets the proposed sampling range. The Z-retrieval method based on the 50 nearest neighbors approaches this range, exceeding it by 3 cm, as it reaches a total of 13 cm in all directions when considering the point-cloud density. In this context, the point clouds used and the profiles obtained with elevation-retrieval methods from multiple points are, in principle, suitable for pavement regularity analysis, since both methods produce highly similar profiles. This suggests that a slight increase in the proposed sampling range does not significantly affect the results.

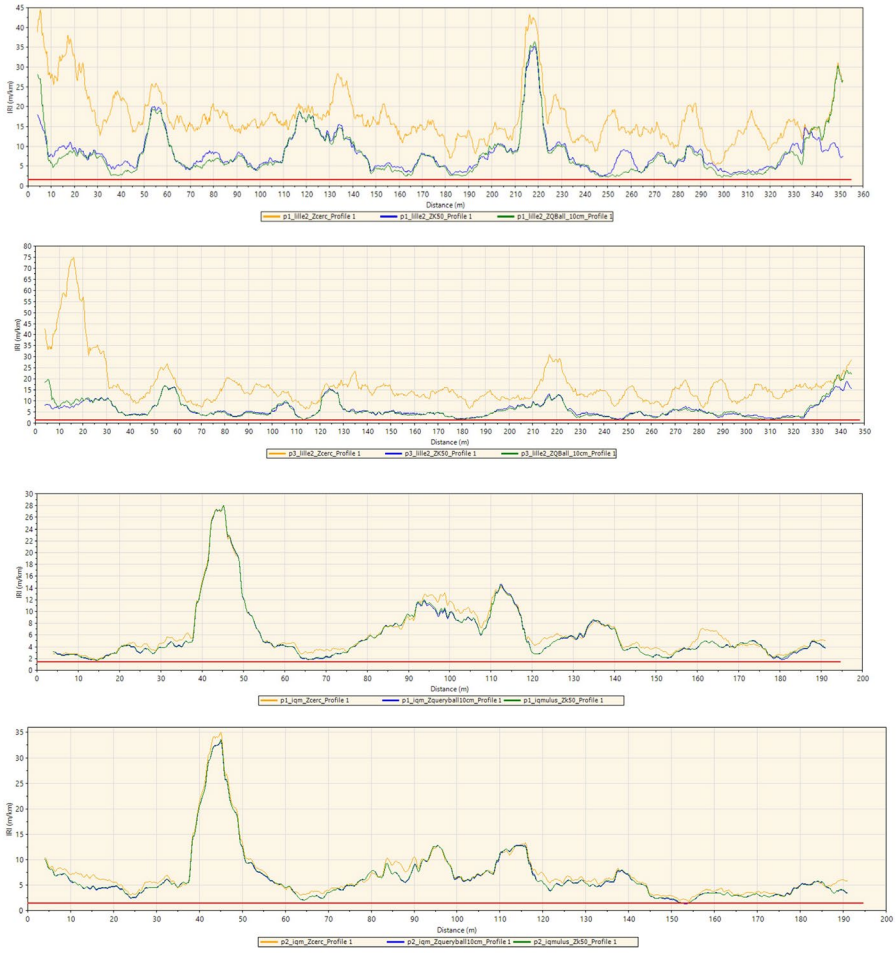


Fig. 5. Cumulative IRI with three methods of obtaining Z coordinates (NN, K50, QB10).

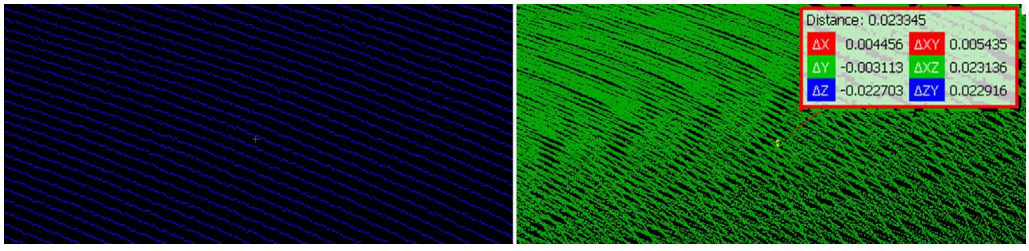


(a) (b)

Fig. 6. Three-dimensional representation and resolution achieved with LiDAR. (a) IQmulus. (b) Lille2.

On the other hand, an analysis of the vertical accuracy of the point clouds would be necessary, which is suggested to be submillimeter, according to the same report. This accuracy is typically assessed by comparing the elevations obtained from the point clouds with those measured through topographic leveling. However, the documentation for the clouds used does not reflect this procedure, so this criterion cannot be taken into account in this discussion.

A qualitative analysis of the geometric characteristics of the point clouds indicates that, in the case of IQmulus, the cloud exhibits greater geometric consistency in its representation, due to the visibly ordered and coherent scan lines, as shown in Fig. 6(a). In contrast, the Lille2 point cloud contains scan lines that intersect without maintaining coherence in the recorded elevations. As shown in Fig. 6(b), two points separated by only 5 mm in planimetric distance ($\Delta XY$) exhibit a vertical difference ($\Delta Z$) of 2 cm, meaning they are practically in the same horizontal position.

The scenario depicted in Fig. 6(b) occurs repeatedly throughout the Lille2 RSPC, indicating that this point cloud does not adequately represent the pavement surface. It could be hypothesized that this issue arises from a mismatch between the GNSS/IMU positioning module and the LiDAR system; However, the documentation available for the cloud [6], [8] is insufficient to draw a conclusive diagnosis, and therefore the cause of this situation remains unknown. A primary guideline to consider when extracting pavement profiles from mobile LiDAR data is the geometric coherence of the point cloud. This experimentation allows for the distinction of two potential scenarios. On one hand, a geometrically coherent point cloud, as is the case with IQmulus, in which the heights of the scan lines are adjusted to reality, without presenting different elevations for the same position. On the other hand, the opposite case is the Lille2 point cloud, where different elevations are recorded at the same location.

The implemented methodology formulates a strategy to handle geometrically inconsistent point clouds by calculating the Z value based on the average of multiple nearby reference points. These methods also yield more robust and reliable results when applied to geometrically coherent point clouds, compared to those obtained using a simple Z calculation based solely on the nearest reference point.

A comparison of the Lille2 profiles shows that the methods based on averaged reference points effectively smooth the resulting profile relative to that obtained using the simple nearest-point method. However, the resulting profiles still exhibit a behavior that is too erratic for a paved surface, indicating that true profiles were not obtained due to the geometric inconsistency of the RSPC. This suggests that the proposed methods are not sufficient to handle this type of cloud, and that new strategies would be required for this purpose or, ultimately, to discard this type of cloud from profile calculations.

For IQmulus profiles, it is again observed that the multi-reference averaged methods smooth the profile calculated with the simple method. In this case, however, all methods yield a similar pavement profile due to the geometric coherence of the cloud. In accordance with the above, and given that the RSPCs meet the recommended point density, it can be stated that the profiles computed for IQmulus correspond to the true pavement profiles and that, consequently, the IRIs derived from them are theoretically correct. However, their practical validation cannot be carried out, as this would only be possible by comparing the results with profiles obtained through well-established methods, such as topography or high-speed inertial profilometers. This validation is beyond the scope of this research. Nevertheless, the results demonstrate that this methodology can generate suitable products to be used as inputs in the calculation of this index through specialized software, such as ProVAL.

Although it cannot be confirmed that the IRIs calculated from the IQmulus data match those obtained using well-established methods, the results highlight relevant aspects regarding the influence of the Z coordinate calculation method on this index. For both clouds, the differences between the global IRIs (Table II), calculated using averaged reference profiles, are small: between 0.15 and 0.29 m/km for Lille2, and between 0.03 and 0.04 m/km for IQmulus. In contrast, the differences between these same values and the IRIs obtained with profiles calculated using the simple

method are significantly greater: between 8.98 and 11.59 m/km for Lille2, and between 0.47 and 0.65 m/km for IQmulus.

It is then evident that the simple Z-retrieval method increases the IRI from magnitudes in the cm range to values above 8 m/km in the case of Lille2, and from magnitudes in the mm range to values greater than 0.4 m/km in the case of IQmulus. This trend can also be seen in the accumulated IRI graphs, where the orange profiles always remain above the other two profiles, while the latter almost always maintain the same trajectory. This indicates that calculating the IRI from profiles obtained using simple methods is not reliable because these approaches assume very abrupt relative elevation changes. These arise because in many cases the heights obtained are not truly representative of the regions to which the abscissas belong, but instead correspond by chance to the nearest points. It is therefore acknowledged that the most appropriate approach is always to use a Z recovery method that considers multiple height references, thereby avoiding the reporting of inflated IRI values, which in many cases could lead to unnecessary pavement interventions.

On the other hand, the results show that the implemented workflow allows recreating pavement profiles in a short time. It should be noted that no references in the available literature propose a method to automate the extraction of pavement profiles. The study most closely related to this work is presented in [15], where the correlation between IRIs obtained from mobile LiDAR and those obtained from high-speed inertial profilometers is reviewed. It was demonstrated that a high correlation exists between these measurements, and that the potential to quantify the regularity of the entire surface is greater than when using linear profile measurements alone.

The research focused on comparing both technologies without dedicating much effort to automating the procedure. Z recovery was performed by reconstructing Digital Elevation Models (DEM) with two different interpolation methods, Inverse Distance Weighting (IDW) and Kriging. This resulted in processing times of 30 min and 10 h, respectively, for a cloud of 150,000,000 points representing 4 km of track. Considering that, in both the aforementioned research and this study, profile calculation only requires coordinate information (X, Y, Z), it is valid to establish a processing time per point relationship. Using this, the method in [15] would require between 0.012 and 0.24 ms of processing per point to obtain the surface from which the ordinates and abscissas of the profile are extracted, whereas the methodology proposed here requires approximately 0.011 ms per point to obtain the complete profile.

In that order, this methodology presents a marginal advantage over the analyzed method, but, in addition, it contributes new elements to the field of LiDAR processing automation for road management, allowing to automatically obtain the axis and the edges of the road, which are objects of study with considerable research interest, as reflected in the works of [16], [17], [18]. Likewise, in this work, the concepts, ordered steps and possible technologies (Python, in this case) for the implementation of the workflow are exhaustively detailed, so that it can be easily understood, improved and reproduced by other researchers in the area. Faced with this, the results show that the proposed processing flow is highly computationally efficient, since the profiles are obtained in a few seconds except for the step of vectorizing the RSPC that requires the calculation of $\alpha$-shape , increasing the processing time due to the high algorithmic complexity of this technique [19].

## IV. Conclusions

A methodology has been established for the automatic extraction of pavement profiles from mobile LiDAR data, and its effectiveness has been demonstrated in accomplishing two essential tasks: the extraction of road edges and centerlines, and the recovery of Z values for the abscissas defining each axis.

The high level of detail and accuracy provided by mobile LiDAR enables the resulting profiles to accurately represent the true pavement profile, thereby facilitating direct IRI calculations.

The results obtained demonstrate the viability of the proposed methodology. First, an effective elevation data recovery strategy from mobile LiDAR scenes enables accurate recreation of the

true pavement profile. Second, the proposed processing workflow for automatic profile generation is highly computationally efficient, as most products are obtained within seconds, except for the RSPC vectorization step, which requires the computation of α-shapes, thereby increasing processing time due to the high algorithmic complexity of this technique.

## V. References


[1] Federal Highway Administration, *Asset Management Overview*, FHWA-IF-08-008, U.S. Department of Transportation, Office of Asset Management, Washington, D.C., Dec. 2007. [Online]. Available: https://www.fhwa.dot.gov/asset/if08008/assetmgmt_overview.pdf?

[2] American Association of State Highway and Transportation Officials (AASHTO), *Transportation Asset Management Guide: A Focus on Implementation*, 2nd ed., ch. 1, "Introduction" (secs. 1.1–1.3). Washington, D.C.: AASHTO, Feb. 27, 2020. [Online]. Available: https://www.tamguide.com/wp-content/uploads/2020/02/TAM_GuideIII_ch01-20200227.pdf?

[3] J. R. Quintero González, "Inventarios viales y categorización de la red vial en estudios de Ingeniería de Tránsito y Transporte," *Revista Facultad de Ingeniería*, UPTC, vol. 20, no. 30, pp. 65–77, 2011. [Online]. Available: https://dialnet.unirioja.es/descarga/articulo/3758451.pdf

[4] M. W. Sayers, "On the Calculation of International Roughness Index from Longitudinal Road Profile," *Transportation Research Record: Journal of the Transportation Research Board*, no. 1501, pp. 1–12, 1995. [Online]. Available: http://onlinepubs.trb.org/Onlinepubs/trr/1995/1501/1501-001.pdf

[5] K. Williams, M. Olsen, G. Roe, and C. Glennie, "Synthesis of Transportation Applications of Mobile LIDAR," *Remote Sensing*, vol. 5, no. 9, pp. 4652–4692, Sep. 2013, doi: https://doi.org/10.3390/rs5094652

[6] X. Roynard, J.-E. Deschaud, and F. Goulette, "Paris-Lille-3D: A large and high-quality ground-truth urban point cloud dataset for automatic segmentation and classification," *The International Journal of Robotics Research*, vol. 37, no. 6, pp. 545–557, Apr. 2018, doi: https://doi.org/10.1177/0278364918767506

[7] B. Vallet, M. Brédif, A. Serna, B. Marcotegui, and N. Paparoditis, "TerraMobilita/iQmulus urban point cloud analysis benchmark," *Computers & Graphics*, vol. 49, pp. 126–133, Jun. 2015, doi: https://doi.org/10.1016/j.cag.2015.03.004

[8] F. Goulette, F. Nashashibi, I. Abuhadrous, S. Ammoun, and C. Laurgeau, "An integrated on-board laser range sensing system for on-the-way city and road modeling," *Revue Française de Photogrammétrie et de Télédétection*, no. 185, pp. 78-83, 2007.

[9] N. Paparoditis *et al.*, "Stereopolis II: A multi-purpose and multi-sensor 3D mobile mapping system for street visualisation and 3D metrology," *Revue française de photogrammétrie et de télédétection*, no. 200, pp. 69–79, Apr. 2014, doi: https://doi.org/10.52638/rfpt.2012.63

[10] H. Edelsbrunner, D. Kirkpatrick, and R. Seidel, "On the shape of a set of points in the plane," *IEEE Transactions on Information Theory*, vol. 29, no. 4, pp. 551–559, Jul. 1983, doi: https://doi.org/10.1109/tit.1983.1056714

[11] F. P. Preparata and M. I. Shamos, *Computational Geometry: An Introduction*, New York / Berlin / Heidelberg: Springer, 1985. doi: https://doi.org/10.1007/978-1-4612-1098-6

[12] T. Křemen, M. Štroner, and P. Třasák, "Determination of Pavement Elevations by the 3D Scanning System and Its Verification," *Geoinformatics FCE CTU*, vol. 12, pp. 55–60, Jun. 2014, doi: https://doi.org/10.14311/gi.12.9

[13] M. W. Sayers and S. M. Karamihas, *The Little Book of Profiling: Basic Information about Measuring and Interpreting Road Profiles*, Ann Arbor, MI: University of Michigan

Transportation Research Institute, Sep. 1998. [Online]. Available: https://hdl.handle.net/2027.42/21605

[14] M. J. Olsen *et al.*, *Guidelines for the Use of Mobile LiDAR in Transportation Applications*, NCHRP Report 748, Transportation Research Board, Washington, D.C., 2013. [Online]. Available: https://onlinepubs.trb.org/onlinepubs/nchrp/nchrp_rpt_748.pdf

[15] M. R. De Blasiis, A. Di Benedetto, M. Fiani, and M. Garozzo, "Assessing of the Road Pavement Roughness by Means of LiDAR Technology," *Coatings*, vol. 11, no. 1, Art. no. 17, Dec. 2020, doi: https://doi.org/10.3390/coatings11010017

[16] B. Suleymanoglu, M. Soycan, and C. Toth, "3D Road Boundary Extraction Based on Machine Learning Strategy Using LiDAR and Image-Derived MMS Point Clouds," *Sensors*, vol. 24, no. 2, Art. no. 503, Jan. 2024, doi: https://doi.org/10.3390/s24020503

[17] Y. Wang *et al.*, "Framework for Geometric Information Extraction and Digital Modeling from LiDAR Data of Road Scenarios," *Remote Sensing*, vol. 15, no. 3, Art. no. 576, Jan. 2023, doi: https://doi.org/10.3390/rs15030576

[18] J. Wang, X. Dong, and G. Liu, "Extraction of Urban Road Boundary Points from Mobile Laser Scanning Data Based on Cuboid Voxel," *ISPRS International Journal of Geo-Information*, vol. 12, no. 10, Art. no. 426, Oct. 2023, doi: https://doi.org/10.3390/ijgi12100426

[19] Z. Yahya, R. W. Rahmat, F. Khalid, A. Rizaan, and A. Rizal, "A Concave Hull Based Algorithm for Object Shape Reconstruction," *International Journal of Information Technology and Computer Science*, vol. 9, no. 3, pp. 1–9, Mar. 2017, doi: https://doi.org/10.5815/ijitcs.2017.03.01

# Virtual Reality for Remote Inspection of Railway Tunnels

Felipe Muñoz La Rivera[1], Andrés López Valenzuela[2], Mathias Proboste[3], Sofía Montecinos Orellana[4], Guillermo Höfflinger Bartsch[5], Javier Mora Serrano[6]

[1] felipe.munoz@pucv.cl, [2] andres.lopez.v@mail.pucv.cl, [3] mathias.proboste@upc.edu, [4] sofia.montecinos@pucv.cl, [5] guillermo.hofflinger@efevalparaiso.cl, [6] mora@cimne.upc.edu

[124] School of Civil Engineering, Pontificia Universidad Católica de Valparaíso, Chile
[3] Escuela de Caminos, Canales y Puertos, Universitat Politècnica de Catalunya, Spain
[5] Efe Valparaíso, Chile | [6] International Centre for Numerical Methods in Engineering, Spain

Recibido: 08 Mayo 2025 / Publicado: 24 Abril 2026
https://doi.org/10.26439/ciic2025.8670

ABSTRACT—**The inspection of railway tunnels is essential to ensure the safety and operability of transportation networks. Traditionally, these inspections are conducted through on-site visual assessments, which entails logistical challenges, occupational hazards, and operational interruptions. Although there have been technological advances in infrastructure inspection, on-site visual inspection remains predominant due to the strong reliance on direct observation and the value of the inspector's field experience. In this context, this study analyzes the efficiency of railway tunnel inspections in virtual reality (VR) environments as an alternative to traditional methods. The research applies Design Science Research Methodology (DSRM) to develop and validate a VR-based inspection protocol, using as a case study a detailed model generated from a point cloud of a railway tunnel. The developed protocol was evaluated and compared with the traditional methodology using 5 key performance indicators (KPIs). The results showed that VR matches the accuracy of traditional inspections, while increasing coverage, reducing operational time, and minimizing service interruptions. However, it also presents certain limitations such as restricted graphical resolution and a learning curve for new users. This study concludes that the effective implementation of VR-based structural inspections represents a key opportunity to significantly improve the management and maintenance of critical infrastructure, providing a safer, more precise, efficient, and operationally sustainable approach.**

*Index Terms*—Railway tunnels, remote inspection, virtual reality (VR).

*Thematic Axes*—Thematic Area 5: Construction Processes and New Technologies >
2. Virtual Design and Construction (VDC)

## I. Introduction

### *A. Inspection and Maintenance of Railway Tunnels*

Railway infrastructure plays a crucial role in transportation systems and faces increasing maintenance demands similar to those observed across the Architecture, Engineering, Construction, and Operation (AECO) sector. In this context, railway tunnels represent a critical component of the network, especially in underground railway systems and mountainous regions. However, these structures are subject to deterioration processes caused by continuous use, geotechnical conditions, humidity, water infiltration, vibrations,

and material aging, which may compromise their structural integrity if not detected in time [1].

Therefore, the periodic inspection and maintenance of railway tunnels is a critical process for ensuring their functional and structural integrity. Effective inspection enables the detection of damage such as cracks, leaks, or deformations, which may lead to severe failures if not addressed in a timely manner. The data gathered during these inspections provide the foundation for planning preventive or corrective maintenance activities and for making operational decisions that ensure the safety of the railway system [2].

In this regard, the traditional method of on-site visual inspection, which requires inspectors to be physically present inside the tunnels, remains the most widely adopted approach [3]. Despite its prevalence, this method poses significant challenges, including the need for temporary track closures, the exposure of personnel to hazardous environments, and a strong dependence on the inspector's experience and judgment. Although a variety of technologies are now available, reliance on on-site visual inspection is still substantial [4].

*B. The Role of VR in Inspections*

The adoption of emerging technologies, such as VR, has begun to substantially transform processes in the construction and infrastructure maintenance sectors. In the specific domain of structural inspection, VR facilitates the reconstruction of highly detailed three-dimensional (3D) environments that may be explored in real time. This development creates new opportunities for remote, safe, and efficient assessment of critical assets, such as railway tunnels [5].

VR enables users to interact with precise digital models that accurately replicate the geometric and material characteristics of real-world structures. These models may be generated by means of point clouds, photogrammetry, or laser scanning, thereby enabling a realistic and navigable representation of the inspected environment [6]. By employing immersive devices, inspectors may explore hard-to-access areas, simulate specific lighting or deterioration conditions, and record observations without physical risk or disruption to railway operations. Furthermore, this technology enables repeated inspections by multiple users, thereby enhancing traceability and promoting standardization [7].

Among the primary advantages of applying VR in infrastructure inspections is the reduction of risks to inspectors by eliminating exposure to hazardous environments. It also minimizes tunnel downtime (TD), as data acquisition may be performed without interference to railway operations [8]. In addition, VR enables broader coverage of the infrastructure, as entire areas may be virtually explored with millimeter-level accuracy [9]. A permanent digital record of the inspection may be kept, enabling historical comparisons, audits, and training activities. Moreover, VR facilitates immersive training experiences by providing realistic scenarios that enable new inspectors to prepare without requiring access to the actual site [10]. Finally, this approach may optimize resources by reducing the logistical and human costs typically associated with frequent on-site inspections [11].

In summary, VR is not merely an alternative to conventional inspection methods; it represents a strategic opportunity to transform the management, maintenance, and inspection of underground railway infrastructure while enhancing both safety and operational efficiency [12].

*C. Research Gap and Objectives*

Despite the growing advancement of technologies for infrastructure inspection, on-site visual inspection remains the predominant methodology [6], [13]. This is primarily attributed to the value of the inspector's direct observation, which allows the identification of subtle structural conditions that are often difficult to detect through automated means [7], [14]. However, this reliance on human perception constrains the adoption of advanced solutions, many of which introduce novel approaches for data acquisition and analysis but face challenges related to data management and the absence of validated, standardized protocols for efficient implementation [5], [15].

In this context, immersive technologies such as VR represent a promising opportunity to redefine inspection processes in a structured, quantifiable, and safe manner. This study aims to evaluate the operational efficiency of railway tunnel inspections performed in VR environments as an alternative to conventional visual methods.

TABLE I
EXPERT PANEL DESCRIPTION

| Profession | Area | Experience (years) |
|---|---|---|
| Mining engineer | Infrastructure inspection | >8 |
| Electrical and electronics engineer | Infrastructure inspection | >10 |
| Transportation engineer | Infrastructure inspection | >15 |
| Transportation engineer | Infrastructure inspection | >12 |
| Electronics engineer | Infrastructure inspection | >6 |

To achieve this objective, a specific inspection protocol was developed and validated using a 3D model generated from a railway tunnel point cloud, enabling a detailed and immersive evaluation of structural conditions.

*D. Article Structure*

The article is organized into three main sections. The first section introduces the methodological framework and the formulation of the inspection protocol within VR environments, describing the adopted approach, the selection of technological tools, and the definition of performance indicators. The second section details the implementation of the protocol in a real case study, encompassing the generation of the 3D model, the construction of the virtual environment, and the implementation of the inspection process. Finally, the third section presents the results and provides a comparative analysis between the conventional inspection methodology and the VR-based approach, assessing its effectiveness, benefits, and limitations.

## II. Research Methodology

For this research, the Design Science Research Methodology (DSRM) was used because of its suitability for the creation and evaluation of technological artifacts, thereby enabling the research process to be represented in a structured manner. The process was divided into five stages: (I) problem and motivation identification, (II) objective definition for a potential solution, (III) design and development, (IV) demonstration, and (V) evaluation.

In the first stage, the available literature was reviewed based on the Web of Science database. Additionally, possible methodologies for tunnel inspection in VR environments were explored using the same source. Based on this research, the second stage focused on defining the objectives of a potential solution, proposing that the use of a VR environment may enhance the efficiency of tunnel inspections.

The third stage designed and developed an inspection protocol for a VR environment. To this end, the standard tunnel inspection methodology established in the technical guidelines of the Chilean National Railway Company (EFE Trenes de Chile) was adopted. Key inspection tasks, such as the identification and mapping of defects including cracks, water ingress, and spalling, were translated into the VR environment to identify areas where VR may enhance efficiency. This process involved incorporating steps for photogrammetric data acquisition and 3D model generation prior to the virtual inspection phase.

The fourth stage formulated the protocol in a case study. The case study was first reconstructed as a 3D model using Autodesk Revit software. A photographic survey of the tunnel was subsequently performed and integrated into the 3D model. Once the model was complete, the VR environment was tested according to the protocol established in the previous stage, and the results were recorded. For the testing phase, a group of experts specializing in railway tunnel inspection was selected. Five experts were appointed, each with more than five years of experience in inspection processes for the company that owns the infrastructure under study. Table I summarizes the characteristics of the experts. Finally, in the fifth stage, the results of the virtual inspection were evaluated and compared with those obtained from a standardized inspection of the case study. Performance indicators were reviewed, and improvements were proposed for both inspection methods.

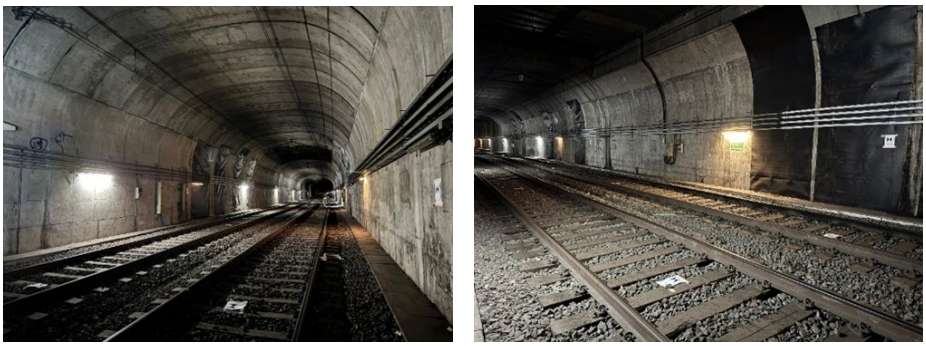

(a) (b)

Fig. 1. Study area in the tunnel. (a) Front view. (b) Side view.

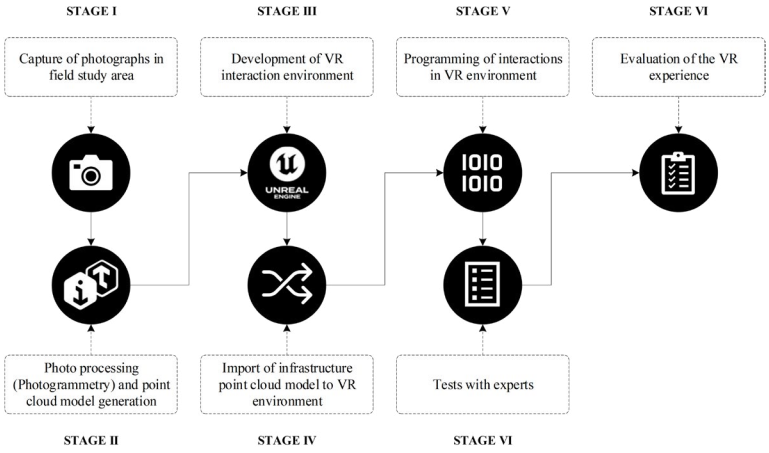


Fig. 2. General diagram of the proposed workflow.

## III. Design and development

### *A. Case Study Description*

The case study focuses on a critical section for regional connectivity within a railway tunnel in Viña del Mar (Chile), used for both passenger and freight transportation. The section selected for the study spans approximately 65 m. The tunnel infrastructure has a straight, horseshoe-shaped geometry, designed to optimize structural stability and load distribution. The distance between the side walls is 7.936 m, and the height from the track platform to the vault is 5.850 m. The tunnel was constructed using the cut-and-cover technique, with reinforced concrete as the primary material, providing durability under operational and environmental conditions. Fig. 1 depicts a photograph of the study area.

### *B. Workflow*

The development of the VR environment for tunnel inspection followed a structured workflow, as shown in Fig. 2, enabling the physical conditions of the infrastructure to be accurately replicated.

The process began with the capture of high-resolution, on-site images during the photogrammetric survey phase (Fig. 3(a)). The images were processed using Bentley's iTwin software, enabling the generation of a detailed 3D model of the tunnel in .las and .obj formats. These formats were adopted for their ability to optimize the

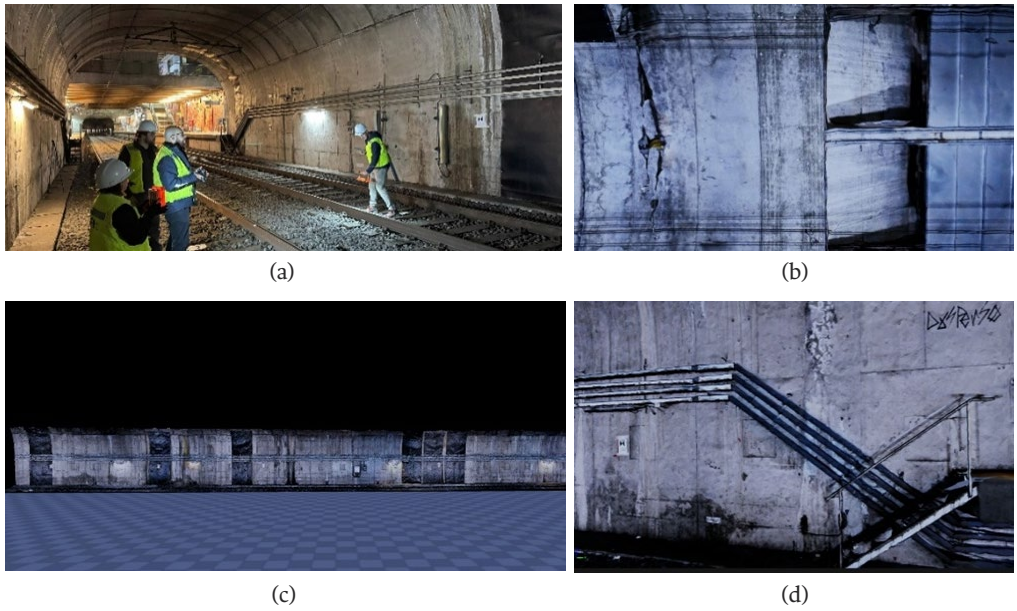

Fig. 3. Developed workflow tasks. (a) On-site photo capture. (b) Point cloud model. (c) Global view of the tunnel in VR. (d) View of tunnel side elements in VR.

geometric and visual representation of the infrastructure. The .obj format was preferred over the .las format for its more efficient use of computational resources, ensuring optimal performance in the VR environment (Fig. 3(b)). Subsequently, the VR environment was set up in Unreal Engine, as shown in Fig. 3(c) and 3(d), integrating the generated models with interactive tools that facilitated navigation and virtual inspection. The environment included options for horizontal and aerial movement, as well as lighting adjustments to enhance the visualization of structural details. In addition, specific digital tools were incorporated, including rulers for crack measurement and marking systems for damage identification.

Upon completion of the virtual environment development, as shown in Fig. 4, preliminary tests were conducted by the research team to ensure its functionality and accuracy. These tests focused on verifying interaction with the models, the clarity of these models within the VR environment, and the overall system usability. These aspects were evaluated prior to testing with expert users.

## IV. Implementation and Results

### *A. Expert Testing*

The VR environment developed for tunnel inspection was validated with the participation of a panel of five experts selected for their experience in railway infrastructure inspection. The evaluation process consisted of three main stages, as shown in Fig. 5.

In the first stage, the experts became familiar with the system, including the use of VR headsets and associated controls, as illustrated in Fig. 6(a). This phase was essential to ensure that participants fully understood the available tools and could interact efficiently within the virtual environment. During the second stage, a virtual inspection session was conducted, during which the experts evaluated the system's capability to identify structural damage—such as cracks and leaks—present in the 3D model, as shown in Fig. 6(b). This analysis included both the identification of critical elements and the interaction

Fig. 4. General view of the tunnel in the study area in a VR environment.

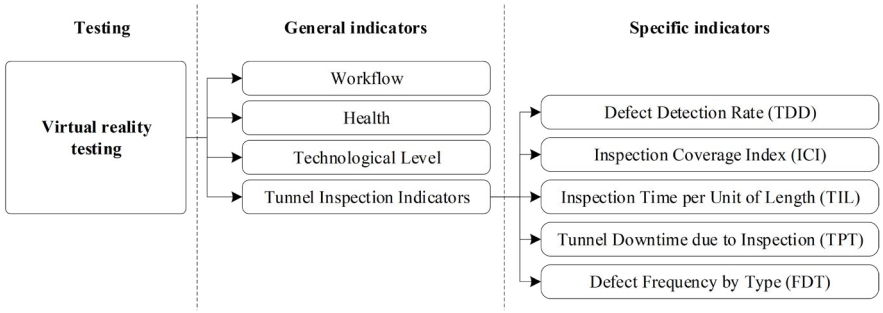


Fig. 5. General view of the tunnel in the study area in a VR environment.

(a) (b)

Fig. 6. Experts interacting with the VR tool. (a) Expert familiarizing himself with his environment. (b) Expert looking for damage in the environment.

with the virtual tools integrated into the inspection protocol. Finally, in the third stage, experts were asked to provide their feedback of the developed environment through structured questionnaires that evaluated aspects such as usability, level of immersion, and the accuracy of the tools compared with traditional inspection methods.

*B. Results*

The following presents the results of the experts' feedback regarding the system workflow, associated physical symptoms, level of technological expertise, and key performance indicators (KPIs) for specific tunnel inspection tasks.

1) Workflow: (1) The analysis of the workflow within the VR environment yielded highly positive results. Four of the five experts rated the workflow as very efficient, while the remaining expert rated it as efficient. This perception highlights that the implemented digital tools, such as the measuring devices and marking systems, significantly optimize the inspection process, enabling a more agile and accurate performance compared with traditional methods. Additionally, the immersive environment was praised for its ability to maintain focus on the assigned tasks. Three out of five participants reported an extremely high level of immersion, while the remaining two rated it as *high.* However, some users reported minor challenges when navigating the environment, particularly with lighting adjustments and the visualization of structural details, which suggested the need for improvements in these technical aspects.

2) *Health:* In terms of physical well-being, most participants reported mild or no symptoms during the use of the system. Two out of five experts reported no discomfort, while a similar percentage mentioned low levels of visual fatigue and slight dizziness. However, one out of five experts experienced a moderate cognitive load, attributed to the need to perform multiple tasks simultaneously, such as inspecting structural elements and navigating through the virtual environment. The levels of visual fatigue were mainly related to the system's graphical resolution and lighting, which were identified as priority areas for future improvements. Moreover, balance and orientation remained stable for most users, although pre-training sessions were recommended for those with less experience in immersive technologies.

3) *Technological Level:* The evaluation of the technological level revealed that prior knowledge of advanced technologies significantly influences the perception of the system's ease of use and utility. Three out of five participants reported that their prior experience with technological tools had a high or very high influence on their ability to interact with the virtual environment. On the other hand, two of the five participants with moderate or low familiarity with these tools reported a steeper learning curve, although they considered it manageable with appropriate guidance. Regarding specific experience with VR, two out of five indicated they had not previously used this technology in professional applications. Nevertheless, all participants were able to adapt to the system, demonstrating its accessibility even for users with limited prior experience. This adaptability reinforces the importance of integrating interactive tutorials and training sessions when deploying immersive technologies in new operational contexts.

4) *Tunnel Inspection Indicators:* The evaluation of the KPIs between traditional inspection methodologies—using data provided by the maintenance company for the same inspection process—and the VR-based methodology. These indicators were designed to measure operational efficiency, coverage, and accuracy, providing a comprehensive assessment of the strengths and areas for improvement in the VR-based approach.

The Defect Detection Rate (DDR) quantifies the number of defects identified per unit of

TABLE II

COMPARATIVE TABLE OF DDR BETWEEN THE TRADITIONAL AND VR METHODOLOGY

| Method | Number of Detected Defects | Inspected Area (m²) | DDR (Defects/m²) |
|---|---|---|---|
| Traditional | 21 | 28.69 | 0.73 |
| VR | 21 | 31.96 | 0.66 |

TABLE III

COMPARATIVE TABLE OF ICI BETWEEN THE TRADITIONAL AND VR METHODOLOGY

| Method | Inspected Area (m²) | Total Tunnel Area (m²) | ICI (%) |
|---|---|---|---|
| Traditional | 28.11 | 31.96 | 88 |
| VR | 31.96 | 31.96 | 100 |

TABLE IV

COMPARATIVE TABLE OF ITUL BETWEEN THE TRADITIONAL AND VR METHODOLOGY

| Method | Total Inspection Time (min) | Inspected Tunnel Length (m) | ITUL (min/m) |
|---|---|---|---|
| Traditional | 90 | 64.76 | 1.39 |
| VR | 60 | 64.76 | 0.93 |

TABLE V

COMPARATIVE TABLE OF TD BETWEEN THE TRADITIONAL AND VR METHODOLOGY

| Method | Total TD (h) | Total Inspection Time (h) | TD (h) |
|---|---|---|---|
| Traditional | 5 | 5 | 1.00 |
| VR | 3.5 | 4.5 | 0.78 |

inspected area. This metric is critical for assessing the effectiveness of each inspection methodology in detecting critical structural damage. In this case, the results showed similar values between the two methods, with 0.73 defects/$m^2$ for the traditional approach and 0.66 defects/$m^2$ for the VR-based approach, as shown in Table II. While the accuracy was comparable, the VR-based approach provided additional advantages in terms of traceability and digital defect recording.

The Inspection Coverage Index (ICI) represents the percentage of the tunnel's total area that was inspected. Results indicated that the VR-based methodology achieved full coverage (100%), while the traditional method reached 88%, as shown in Table III. This difference reflects the capability of the VR-based approach to evaluate hard-to-reach areas, thereby minimizing the risk of overlooking critical zones.

The Inspection Time per Unit Length (ITUL) was used to measure the time efficiency of each methodology. VR showed a significant advantage, reducing the required time from 1.39 to 0.93 min per inspected meter, as shown in Table IV. This improvement reflects the elimination of external interruptions such as weather conditions or operational constraints.

The TD metric assesses the operational impact of inspections on railway service. The VR-based approach reduced this time from 5 to 3.5 h, demonstrating its capability to perform comprehensive evaluations with minimal disruption to operations, as shown in Table V.

TABLE VI

Comparative table of DFT between the traditional and VR methodology

| Method | Structural concrete defects | Water defects | Total defects | DFT concrete (%) | DFT water (%) |
|---|---|---|---|---|---|
| Traditional | 5 | 16 | 21 | 24 | 76 |
| VR | 5 | 16 | 21 | 24 | 76 |

The Defect Frequency by Type (DFT) metric enabled the categorization of detected damages, supporting a more detailed analysis of maintenance needs. Both methods identified similar patterns, with 76% of defects associated with water infiltration and 24% associated with structural concrete issues, as shown in Table VI.

## V. Discussions

### *A. General Discussions*

The implementation of VR in the inspection of railway tunnels has proven to be a significant advancement in the optimization of critical maintenance processes. The results obtained through KPIs confirm the feasibility of the proposed methodology, demonstrating its capability to achieve accuracy comparable to that of traditional inspections while improving coverage and reducing operational times. The DDR values were comparable between both methodologies, indicating that VR can effectively replicate established detection standards.

Additionally, the ICI metric demonstrated a significant advantage for the VR approach, achieving 100% coverage compared to 88% for the traditional method. This aspect is particularly relevant in complex environments, where traditional inspections may face logistical limitations. Moreover, the reduction in ITUL and TD underscores the operational efficiency of the virtual-based approach, minimizing disruptions and improving resource planning. These findings suggest VR has potential for integration into standard tunnel inspection workflows, providing quantifiable benefits beyond those achievable with traditional methods.

However, some technical challenges remain. Participants with less experience in immersive technologies reported moderate difficulties in visualizing specific details, primarily due to issues with graphical resolution and lighting adjustments. These findings highlight the importance of technical improvements and the incorporation of training programs to optimize user experience.

### *B. Limitations*

Although the VR-based methodology demonstrated high potential, the development and implementation of the model faced several limitations that must be considered:

- Logistical challenges for tunnel access: Obtaining the necessary Weekly Work Permit (PST) posed significant challenges, particularly in complying with strict railway safety regulations related to high-voltage catenaries. The requirement for specific licenses, such as the P6 permit, and the need for coordination with multiple entities delayed the initial data collection process.
- Limitations of photographic equipment: Relying on a standard camera for visual surveying-imposed restrictions on capturing complex geometric details. Although a 90% image overlap ensured sufficient coverage, the use of advanced tools—such as LiDAR cameras or specialized drones—could have further improved the quality of data capture.
- Computational constraints: Rendering the detailed 3D model using software like Unreal Engine and iTwin required intensive computational resources. This led to extended model generation times and

occasional navigation difficulties within the virtual environment, especially on mid- to low-range devices. These findings highlight the need to optimize rendering and visualization algorithms to facilitate broader adoption across various operational contexts.

### *C. Future Research Directions*

This study opens multiple opportunities to expand and enhance the application of VR in structural inspections. Key directions for future research include:

- Integration of interactive tools: Developing new functionalities within the virtual environment—such as tools for measuring cracks directly on the 3D model or for marking damaged areas in real time—could enhance inspection accuracy and traceability. These tools would also facilitate the generation of automated reports.
- Improvements in data capture: The integration of advanced technologies, such as LiDAR cameras or drones equipped with multispectral sensors could improve the quality and precision of initial surveys, overcoming limitations associated with conventional photographic equipment.
- Computational optimization: Research aimed at reducing computational demands for rendering and navigating virtual environments could significantly increase accessibility. This includes the implementation of more efficient algorithms, 3D model compression, and adaptive visualization techniques.
- Validation in different scenarios: Expanding the application of VR to other infrastructure types, such as bridges or underground stations, would provide a broader comparative framework to evaluate its applicability under diverse structural and operational conditions.

## VI. Conclusions

This study demonstrates that the implementation of VR environments in railway tunnel inspections is not only feasible but also highly effective in terms of efficiency, safety, and accuracy. The results demonstrate that VR maintains a DDR comparable to traditional inspections, while offering additional benefits in key areas such as the ICI, which reached 100%, significantly surpassing the 88% achieved with conventional methodologies. This level of coverage ensures a comprehensive evaluation, reducing the likelihood of overlooking critical areas.

In addition, VR optimizes operational times, reducing the ITUL from 1.39 to 0.93 min/m, and decreasing the TD from 5 to 3.5 h. These results reinforce the capability of this technology to conduct inspections more efficiently, minimizing operational disruptions and associated costs.

Nevertheless, challenges remain that must be addressed to maximize the adoption of this technology. Among them are the need to improve technical aspects of the system, such as graphical resolution and lighting, and to provide adequate training to reduce the learning curve for inspectors with limited experience in advanced VR tools. Additionally, further research should prioritize the validation of the developed protocol and its replicability in other infrastructure contexts.

Overall, this study contributes to the existing body of knowledge by establishing a standardized protocol for railway tunnel inspection using VR, demonstrating its advantages over traditional methodologies. These findings underscore the potential of VR not only to transform maintenance processes in railway infrastructure but also to be applied across other areas of civil engineering, promoting safer, more efficient, and sustainable practices.

## References

[1] N.-H. Pan and N. N. Isnaeni, "Integration of Augmented Reality and Building Information Modeling for Enhanced Construction Inspection—A Case Study," *Buildings*, vol. 14, no. 3, p. 612, Mar. 2024, doi: https://doi.org/10.3390/buildings14030612

[2] A. Sánchez-Rodríguez, B. Riveiro, M. Soilán, and L. M. González-deSantos, "Automated detection and decomposition of railway tunnels from Mobile Laser Scanning

Datasets," *Automation in Construction*, vol. 96, pp. 171–179, Dec. 2018, doi: https://doi.org/10.1016/j.autcon.2018.09.014

[3] A. Sjölander, V. Belloni, A. Ansell, and E. Nordström, "Towards Automated Inspections of Tunnels: A Review of Optical Inspections and Autonomous Assessment of Concrete Tunnel Linings," *Sensors*, vol. 23, no. 6, Art. no. 3189, Mar. 2023, doi: https://doi.org/10.3390/s23063189

[4] A. Sadhu, J. E. Peplinski, A. Mohammadkhorasani, and F. Moreu, "A Review of Data Management and Visualization Techniques for Structural Health Monitoring Using BIM and Virtual or Augmented Reality," *Journal of Structural Engineering*, vol. 149, no. 1, Jan. 2023, doi: https://doi.org/10.1061/(asce)st.1943-541x.0003498

[5] R. Zhang, G. Hao, K. Zhang, and Z. Li, "Reactive UAV-based automatic tunnel surface defect inspection with a field test," *Automation in Construction*, vol. 163, Art. no. 105424, Jul. 2024, doi: https://doi.org/10.1016/j.autcon.2024.105424

[6] R. Argüelles-Fraga, C. Ordóñez, S. García-Cortés, and J. Roca-Pardiñas, "Measurement planning for circular cross-section tunnels using terrestrial laser scanning," *Automation in Construction*, vol. 31, pp. 1–9, May 2013, doi: https://doi.org/10.1016/j.autcon.2012.11.023

[7] M. Pejić, "Design and optimisation of laser scanning for tunnels geometry inspection," *Tunnelling and Underground Space Technology*, vol. 37, pp. 199–206, Aug. 2013, doi: https://doi.org/10.1016/j.tust.2013.04.004

[8] X. Núñez-Nieto, M. Solla, A. Novo, and H. Lorenzo, "Three-dimensional ground-penetrating radar methodologies for the characterization and volumetric reconstruction of underground tunneling," *Construction and Building Materials*, vol. 71, pp. 551–560, Nov. 2014, doi: https://doi.org/10.1016/j.conbuildmat.2014.08.083

[9] L. Bellini Machado and M. Massao Futai, "Tunnel performance prediction through degradation inspection and digital twin construction," *Tunnelling and Underground Space Technology*, vol. 144, Art. no. 105544, Feb. 2024, doi: https://doi.org/10.1016/j.tust.2023.105544

[10] Z. Huang, H. Fu, J. Zhang, W. Chen, and Y. Shi, "Structural Damage Evaluation Method for Metro Shield Tunnel," *Journal of Performance of Constructed Facilities*, vol. 33, no. 1, Nov. 2018, doi: https://doi.org/10.1061/(asce)cf.1943-5509.0001248

[11] D. Llanca, P. Breul, and C. Bacconnet, "Improving the diagnosis methodology for masonry tunnels," *Tunnelling and Underground Space Technology*, vol. 70, pp. 55–64, Nov. 2017, doi: https://doi.org/10.1016/j.tust.2017.07.002

[12] F. Foria, M. Calicchio, L. Moretti, and G. Loprencipe, "Multidimensional mobile mapping and integrated approach for the digitalisation of underground transport infrastructure," *Acta Polytechnica*, vol. 63, no. 2, pp. 111–122, May 2023, doi: https://doi.org/10.14311/ap.2023.63.0111

[13] T. Askarzadeh, R. Bridgelall, and D. D. Tolliver, "Systematic Literature Review of Drone Utility in Railway Condition Monitoring," *Journal of Transportation Engineering, Part A: Systems*, vol. 149, no. 6, Jun. 2023, doi: https://doi.org/10.1061/jtepbs.teeng-7726

[14] L. Hesselink, F. Vahdatikhaki, Y. Harmsen, and H. Voordijk, "Usability analysis of virtual-reality-enabled digital twin for the inspection of sewage pumping stations," *International Journal of Construction Management*, vol. 24, no. 13, pp. 1419–1430, Jun. 2023, doi: https://doi.org/10.1080/15623599.2023.2219941

[15] M. Omer, L. Margetts, M. Hadi Mosleh, S. Hewitt, and M. Parwaiz, "Use of gaming technology to bring bridge inspection to the office," *Structure and Infrastructure Engineering*, vol. 15, no. 10, pp. 1292–1307, May 2019, doi: https://doi.org/10.1080/15732479.2019.1615962

UNIVERSIDAD
DE LIMA